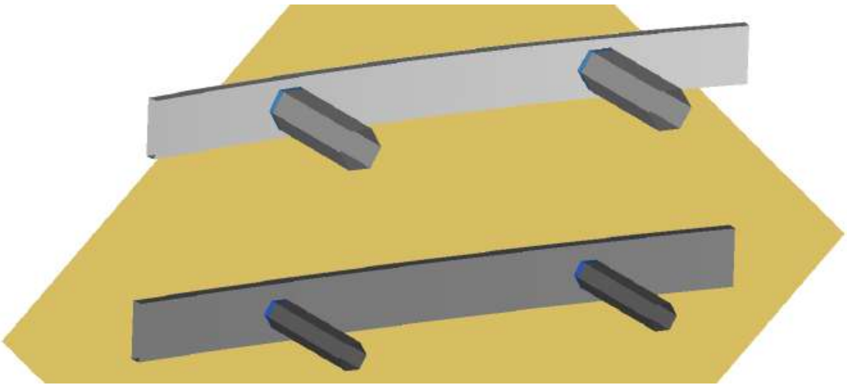

Front Secondary Crash Management System

Samuel Alves Cardoso

Thesis to obtain the Master of Science Degree in

Aerospace Engineering

Supervisors: Prof. André Calado Marta
Eng. Luís Miguel Ouro Colaço

Examination Committee

Chairperson: Prof. Filipe Szolnoky Ramos Pinto Cunha
Supervisor: Prof. Prof. André Calado Marta
Member of the Committee: Prof. Miguel António Lopes de Matos Neves

November 2018

Dedicated to my grandfather

Acknowledgments

I want to thank my supervisors, Professor André Marta and engineer Luís Colaço for their support during this project.

Thanks to CEiiA and specially the mobility team for the availability and help whenever it was necessary.

A special word to my colleague José Pereira for his companionionship and patience every day in this internship.

To my colleagues and friends in CEiiA, Pedro Santana, Henrique Oliveira, Jorge Ramos and Rui Vilaça for the good time spent together.

To my friends João Louro, Diogo Sanches, Luís Louro for the long nights in IST and Sertã and for all the good moments during the last five years.

To my father, mother and sister for all the support, love and presence in the worst and best moments of my way. Thank you for always believing in me.

To the rest of my family, and specially to my grandmother, my uncle Alberto Reis, my aunt Isabel Reis and my cousin Hugo Reis for the affection and support.

To my friends from Sertã and Erasmus for the good time and the laughs for the simpler things.

Finally, to Filarmónica União Sertaginense and the people from the Residência Duarte Pacheco for the extra-university times and for helping me grow.

Resumo

Nos últimos 20 anos, mais de 800 mil pessoas morreram nas estradas da União Europeia. Graças ao esforço conjunto de algumas organizações e governos, estes números têm vindo a decrescer devido à criação de regulamentação para a inclusão de sistemas de proteção passiva e ativa nos veículos. Consequentemente, este trabalho foi desenvolvido no âmbito da criação de uma estrutura ou várias estruturas que protejam os ocupantes em caso de colisão frontal de forma a serem aplicadas numa plataforma modular que irá albergar várias tipologias de veículos.

Assim, para cada caso, foram desenvolvidas as estruturas para a proteção dos ocupantes de forma a respeitar o protocolo de colisão frontal total do Euro NCAP. O processo de desenvolvimento das estruturas baseou-se na parametrização de parte da geometria e uma optimização genética multi objectivo utilizando resultados de análises de elementos finitos, de forma cumprir os pressupostos para o ensaio de teste frontal.

Foram analisados quatro tipos de veículos em que foi desenvolvida uma estrutura primária que absorve a energia correspondente à massa do veículo mais leve e estruturas secundárias que serão adicionadas à primária para que absorvam a energia correspondente à diferença de massa nos veículos mais pesados.

As geometrias obtidas cumprem os pressupostos, tendo sido obtida uma boa relação entre o acréscimo de massa nestas estruturas e a absorção de energia durante o impacto. Por outro lado, a inserção da estrutura secundária provou ter efeitos bastantes satisfatórios no comportamento geral durante o acidente.

Palavras-chave: colisão frontal, optimização multi objectivo, Euro NCAP, algoritmo genético, sistema secundário, absorpção de choques

Abstract

Over the past 20 years, more than 800,000 people have died on the roads of the European Union. Thanks to the joint effort of some organizations and governments, these numbers have been decreasing due to the creation of regulations to include passive and active protection systems in vehicles. This way, this work was developed to create a structure or several structures that protect the occupants in case of frontal collision in order to be applied in a modular platform that will carry several types of vehicles.

Thus, for each case, the structures were developed to protect the occupants regarding the Euro NCAP frontal full width test protocol. The structural development process was based on some geometric parametrization and a multi-objective genetic optimization was used to find the best solutions from the finite element analyses.

Four types of vehicles were considered. For the lighter case, a primary structure was developed to absorb the corresponding energy during the impact. The heavier vehicles have a secondary structure to absorb the energy corresponding to the added weight.

The final geometries have proven to fulfil the assumptions, obtaining a good relation between the mass increase in these structures and the energy absorption during the impact. On the other hand, the insertion of the secondary structure proved to have satisfactory effects on the overall behaviour during the crash events.

Keywords: frontal collision, multi objective optimization, Euro NCAP, genetic algorithm, secondary system, energy absorption

Contents

Acknowledgments v
Resumo vii
Abstract ix
List of Tables xiii
List of Figures xv
Nomenclature 1
Glossary 1

1 Introduction 1
1.1 Motivation 1
1.2 Project Background 4
1.3 Objectives 4
1.4 Thesis Outline 5

2 Background 7
2.1 Materials 7
2.2 Regulations 9
2.2.1 European Regulations 9
2.2.2 Euro NCAP 10
2.3 Crashworthiness Principles 11
2.4 Thin Walled Beams 12
2.5 Material Characteristics 17
2.5.1 Material Law 17
2.5.2 Heat Affected Zone 20
2.6 Finite Elements Analysis 21
2.7 Optimization Algorithms 24
2.7.1 Single-objective Optimization Algorithms 24
2.7.2 Multi-objective Optimization Algorithms 25

3 Implementation 29
3.1 Material Selection 29
3.2 Optimization Procedure 31

3.2.1 Setup of **CATIA™ V5** . . . 31
3.2.2 Primary Considerations . . . 32
3.2.3 Geometry Setup . . . 36
3.2.4 Setup of **Altair® HyperMesh®** . . . 39
3.2.5 Setup of **Altair® HyperGraph®** . . . 44
3.2.6 **MATLAB®** scripting . . . 46

4 Results **49**
4.1 Primary Structure . . . 49
4.2 Secondary Structure . . . 58
4.2.1 Sports Car . . . 60
4.2.2 Be 2.0 . . . 63
4.2.3 Big Sedan . . . 66
4.2.4 Final Comparisons . . . 69
4.2.5 Computational Cost Assessment . . . 72

5 Experimental Validation Procedure **73**
5.1 Material Validation . . . 73
5.2 Quasi-static Approximation . . . 74

6 Conclusions **79**
6.1 Achievements . . . 79
6.2 Future Work . . . 80

Bibliography **81**

List of Tables

1.1 Different vehicle topologies and corresponding weights 5

2.1 Assumed weight savings for alternative materials [12]. 8
2.2 Euro NCAP frontal tests 10
2.3 Euro NCAP lateral tests 10
2.4 Several criteria for NCAP head injury evaluation 11
2.5 Heat Affected Zone length by thickness values for MIG welding [42] 21

3.1 Selected materials for optimization comparison (adapted from [42]) 30
3.2 Aluminum tempers (adapted from [54]) 30
3.3 Description of the parameters used to build the geometry 31
3.4 Geometry parameters for mesh convergence test 33
3.5 Geometry parameters for HAZ comparison 36

4.1 Fixed geometry parameters for primary structure evaluation 50
4.2 Fixed parameters for the primary structure 51
4.3 *gamultiobj* input parameters 52
4.4 Diverged simulation results 55
4.5 Color code for each type of material 56
4.6 Symbol for each type of cross shape 56
4.7 Obtained values for selected points for the primary structure 57
4.8 Variable values for chosen points in the primary structure optimization 58
4.9 Different masses applied for secondary structure optimization 58
4.10 *gamultiobj* input parameters for secondary strcture optimization 59
4.11 Obtained values from the Sports Car structure optimization 61
4.12 Variable values for chosen points in the Sports Car optimization 62
4.13 Obtained values from the Be 2.0 structure optimization 65
4.14 Variable values for chosen points in the Be 2.0 optimization 65
4.15 Obtained values from the Big Sedan structure optimization 68
4.16 Variable values for chosen points in the Big Sedan optimization 68
4.17 Micro Car optimized structure 69
4.18 Sports Car, Be 2.0 and Big Sedan optimized structures 70

4.19 Simulation time for each optimization 72

5.1 Dimensions for the tensile test specimen (adapted from [58]) 73
5.2 Values for quasi-static and dynamic comparison 75
5.3 Quasi-static comparison between the total and half structures 76

List of Figures

1.1 Evolution of fatalities, accidents and injured EU [2]. 1
1.2 Design and production phases for a structure 2
1.3 Drop test facility [6] 3
1.4 Be project [9]. 4

2.1 UN Regulation 94 & 95 front and side impact crash tests [18]. 10
2.2 Representative force - displacement curve 12
2.3 Quadrangular cross shape with different types of graded thickness (adapted from [26]) . 13
2.4 Complete aluminium bumper and crash boxes made from extrusions for the Renault Megane (adapted from [34]) 13
2.5 Axial collapsed beams [14] 14
2.6 Fold with displacement 2H (adapted from [35]) 15
2.7 Cross-sectional geometry of tubes and typical angle elements (adapted from [35], [36]) . 16
2.8 Division of constituent elements in multi-cell hexagonal tubes (adapted from [37]) 16
2.9 Typical stress strain curve 17
2.10 Elastic plastic piecewise linear material from $RADIOSS^{®}$ [38] 18
2.11 Strain rate effect in yield stress [38] 19
2.12 Weld area, heat affected zone and properties description (adapted from [40]) 20
2.13 Collapse mode prediction for a full car FE model (adapted from [14]) 22
2.14 Difference in calculation cost between implicit and explicit solver [46] 22
2.15 Explicit integration flow chart 23
2.16 Global minimum vs global maximum search principle [47] 24
2.17 Multi-objective flow charts (adapted from [48]]) 26
2.18 Pareto front example [47]. 27
2.19 Constrained optimization [48]. 27
2.20 Pareto front ranks [47]. 28

3.1 Aluminum extrusions [53]. 30
3.2 Parametrized geometry for the primary structure 31
3.3 Parametrized geometry for both structures 32
3.4 Isometric views for both files 32

3.5 Filtered vs non-filtered curves 33
3.6 Simulation time vs mesh size. 34
3.7 Force-displacement curves for each mesh size 34
3.8 Force-displacement curves for the most refined meshes 34
3.9 Comparison between the deformed structure with different meshes 35
3.10 Bumper with the Heat Affected Zone (blue) and unchanged properties (yellow) 35
3.11 Force-dispacement curve for a structure with and without HAZ effect 36
3.12 Comparison between different approaches to analyse the structures 37
3.13 Results from a simulation with both primary and secondary structures 38
3.14 Comparison between the displacements in the structures for a separate or a joint simulation 38
3.15 Extruded geometry in positive Z direction 39
3.16 Comparison between original geometry and generated midsurfaces 39
3.17 Defined contact with $CARD\ TYPE\ 7$ 40
3.18 Structures and rigid wall 40
3.19 Created materials 41
3.20 Meshed geometry 42
3.21 Generated rigid bodies 42
3.22 Selected nodes to rigid body creation 43
3.23 Element selection for HAZ properties 43
3.24 Exported curves by HyperGraph 45
3.25 MATLAB script flowchart 46

4.1 Estimated energy absorption percentages in the frontal structure (adapted from [57]) . . 49
4.2 Curve adjustments to choose fixed parameters for optimization 51
4.3 Comparison between curves with different fixed parameters 51
4.4 Crash box shapes for optimizations 52
4.5 Optimization ouptuts example 53
4.6 Example of diverged simulation 55
4.7 Individual solutions for the primary structure 56
4.8 Final solutions for the primary structure 56
4.9 Force vs displacement curves for the selected solutions in the primary structure optimization 57
4.10 Optimized primary structure 58
4.11 Individual solutions for Sports Car structure 60
4.12 Final solutions Sports Car structure 61
4.13 Force vs displacement curves for the selected solutions in the Sports Car structure optimization 62
4.14 Force vs displacement curves corresponding to the selected optimal geometry for the sports car 63
4.15 Individual solutions for Be 2.0 structure 64

4.16 Final solutions for Be 2.0 structure 64
4.17 Force vs displacement curves for the selected solutions in the Be 2.0 structure optimization 65
4.18 Force vs displacement curves corresponding to the selected optimal geometry for the Be 2.0 Car 66
4.19 Individual solutions for the Big Sedan structure 67
4.20 Final solutions for the Big Sedan structure 67
4.21 Force vs displacement curves for the selected solutions in the Big Sedan structure optimization 68
4.22 Force vs displacement curves corresponding to the selected optimal geometry for the Big Sedan 69
4.23 Comparison between energy absorption and maximum peak force for each case 70
4.24 Optimized Sports Car structures 71
4.25 Optimized Be 2.0 structures 71
4.26 Optimized Big Sedan structures 71

5.1 Specimen parameters for the tensile test (adapted from [58]) 73
5.2 Force vs displacement curves for dynamic and quasi-static comparison 74
5.3 Trimmed force vs displacement curves for dynamic and quasi-static comparison 75
5.4 Meshed half geometry 75
5.5 Comparison between the tests with the half and total geometry 76
5.6 Comparison between the tests with the half and total geometry with trimmed curves . . . 76
5.7 Quasi-static procedure 77
5.8 Isoview of the quasi-static procedure 77

Chapter 1

Introduction

1.1 Motivation

Car accidents represent one of the largest problems in human losses in society. In the last twenty years, more than 800,000 people died on the roads of the European Union. Thanks to a joint effort of governments and some organizations, the number of deaths has been declining. Figure 1.1 shows that the reduction is occurring, although the number of zero deaths is far from being achieved.

In 2011, the goal of zero deaths was set for 2050 with a realignment of targets in 2020 [1]. The mortality reduction is happening due to improved road conditions, increased vehicle safety and greater driver awareness. By the creation of entities to regulate vehicles and road conditions, the apparently utopic goal proposed to 2050 is closer to be achieved.

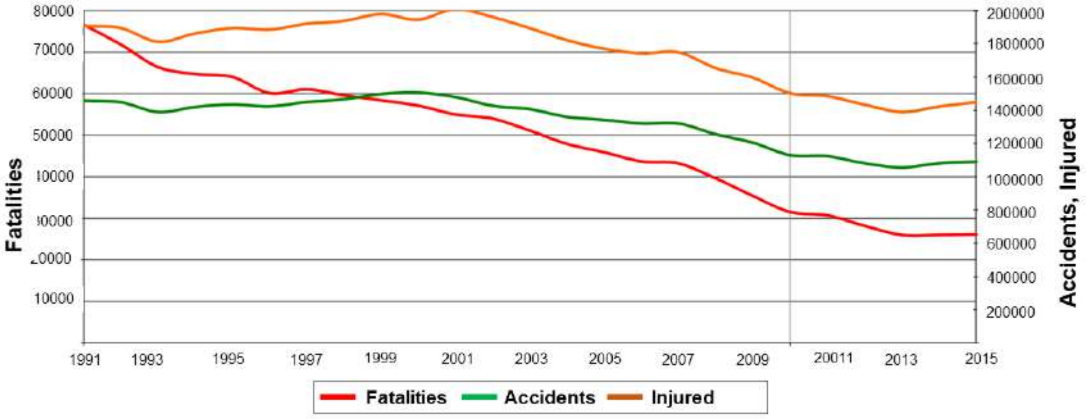

Figure 1.1: Evolution of fatalities, accidents and injured in European Union [2].

Through the European Road Assessment Programme (Euro RAP), it is possible to have a perception through a rating system of which roads need a significant improvement or more speed restrictions. With the increase in network technology, the concept of intelligent roads is being implemented. The information given in real time to drivers such as surface conditions, road works, or traffic situation prevents unexpected situations that could result in accidents and improves fluidity in road traffic [2].

In addition to quality of roads, vehicle safety took an important role in preventing road deaths by the development of sophisticated active and passive security mechanisms.

Beyond the Euro RAP that was created to measure the road safety levels, the European New Car Assessment Vehicle (Euro NCAP), was created to classify the performance and inform the consumer about safety levels in new vehicles. With these ratings, car companies compete with each other to meet consumer and market standards. The improvements imposed by these factors have led to safer vehicles and consequently a survival rate increase in case of an accident. With the development of some active safety systems such as Anti-lock Braking System (ABS), Electronic Stability Control (ESC), Intelligent Speed Adaptation (ISA), Collision Avoidance System (CAS), it is possible to avoid collisions or diminish the speed before the impact [3].

In the last few years, market trends are increasingly pushing the automotive industry toward electric power trains. The low ecological footprint associated with the high efficiency of electric motors has been translated into an alternative to the large emissions produced by conventional internal combustion engines. One of the most important aspects in an electric car, besides safety, is its autonomy. In this way, the structures developed to be in a vehicle of this type should be as light as possible. A reduction in weight translates into better performances and noticeable consumption reductions [4].

Additionally, it is important to distinguish between an high and low velocity impact. In an high velocity impact, the main objective of the structures is to absorb the kinetic energy of the vehicle while in a low velocity impact, the main objective is to diminish the damage made in the car. Analysing the statistics, front collisions are the most frequent and fatal type of crash [5], so it is very important to design passive systems such as airbags and bumpers to protect the passengers in case of an accident. In an impact of this type, the most solicited structure is the front bumper. To protect effectively the occupants, this structure needs to be robust and light enough to absorb as much energy as possible.

It is possible to predict the behaviour of the structure in case of impact before the production phase using 3D modelling software and Finite Element Analysis (FEA). This procedure can give the main characteristics of the structure such as energy absorption and decelerations. Through crashworthiness principles, it is possible to have the perception of some errors in the design stage, preventing the propagation of these errors to the production phase.

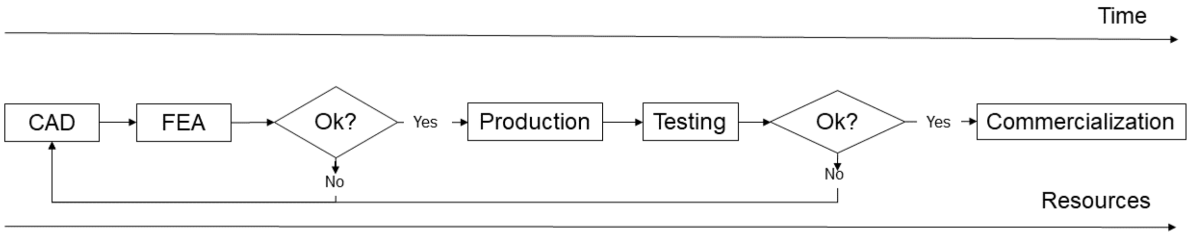

Figure 1.2: Design and production phases for a structure

Figure 1.2 shows that when an error is found at a later stage, the time and resources spent for its correction will be greater. Since the engineering process is iterative, it is natural that there are many corrections until the final product. If these corrections are made in a earlier stage, it will lead to larger savings in time and resources.

The objective of this work is to design and analyse a secondary crash management system according with different vehicle masses. It will be predicted a primary structure which will absorb the energy that corresponds to the impact by the vehicle with lower mass. The secondary structure will be responsible to absorb the remaining kinetic energy correspondent to the additional mass present in heavier vehicles.

This thesis is done with the intention of obtaining the Master of Science degree in Aerospace Engineering. Although the work focuses on aspects related to the automotive industry, the results obtained and the procedures developed can be used in the development of aeronautical products as exemplified by the drop test presented in figure 1.3.

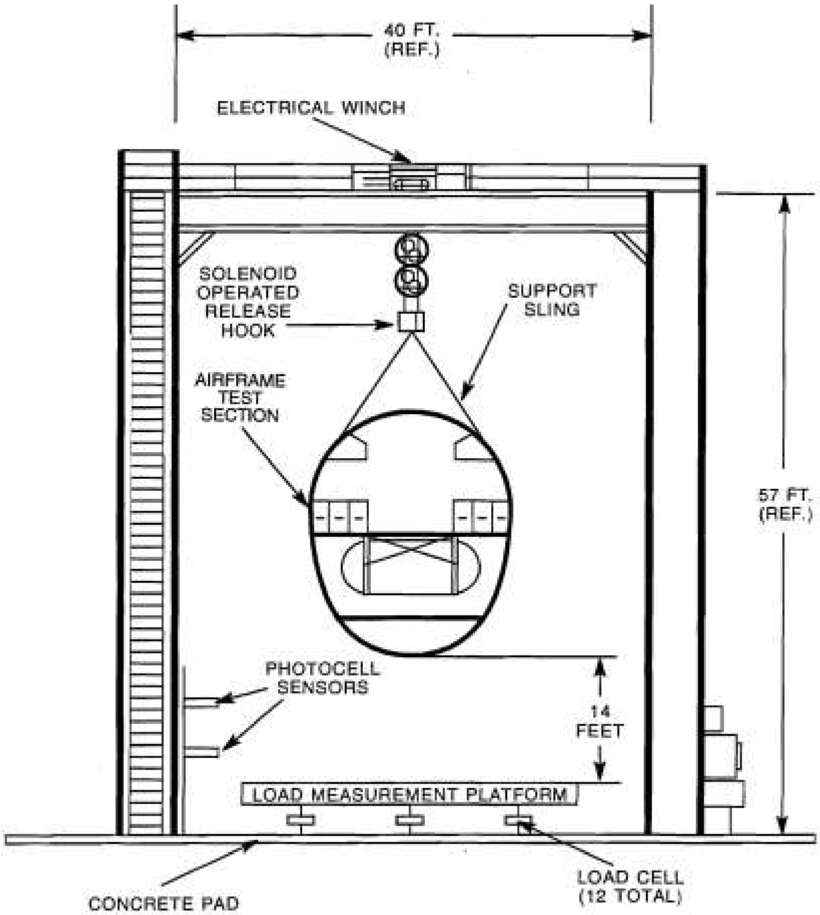
40 FT.
(REF.)
ELECTRICAL WINCH
SOLENOID
OPERATED
RELEASE
HOOK
SUPPORT
SLING
AIRFRAME
TEST
SECTION
57 FT.
(REF.)
PHOTOCELL
SENSORS
14
FEET
LOAD MEASUREMENT PLATFORM
CONCRETE PAD
LOAD CELL
(12 TOTAL)

Figure 1.3: Drop test facility [6]

With this procedure, it is possible to evaluate the fuselage performance analysing the dynamic response of the structures during the impact. The airplane part is dropped by an height of 4.27 meters with an impact velocity of 9.14 m/s [6]. Concluding, crash tests are always performed for any vehicle that needs to prove that is effective in protecting its occupants during an accident so these procedures are applied both in automotive and aeronautical areas.

1.2 Project Background

The analysis and design of the crash management system is part of a larger project led by CEiiA. The previous work developed by Nunes [7] in CEiiA was a start point to develop the secondary solutions based on the optimization procedure applied in his work.

CEiiA – Centre of Engineering and Product Development, was created in 1999 to increase the support of the Portuguese automotive industry. Located in Matosinhos - Porto, is one of the most active companies in Portugal developing new products and services. Nowadays, about 200 high qualified engineers work in CEiiA to discover and develop solid solutions in aeronautics, mobility, naval/offshore and automotive. With unique project methodologies, covering all product development phases from concept to the production of small series, and operating intelligent systems, CEiiA has become one of the most innovating organizations in Portugal [8].

The Be project

Mobicar is a research and development project for the design, testing and demonstration of the main modules that comprehend the new requirements of mobility, energy and information systems with application to different platforms for electric mobility environments. Those modules include the seat, interior, exterior, power train, and vehicle platform. The Be project, presented in 2016, is the main result of this process of development.

The goals of the Be project, illustrated in figure 1.4 are [8]:

- To attract new investment associated to new logics of motorization and mobility services;
- To develop a national industrial cluster with capacity to design, develop, industrialize and test electric vehicles and integrated services for the new environments of sustainable mobility;
- To position Portugal as a world reference in Electric Mobility and export an integrated solution.

Figure 1.4: Be project [9].

1.3 Objectives

This project aims to design the structures of energy absorption in case of impact for various types of vehicles. The construction of a modular vehicle with a common platform that includes the chassis, power train, drive train and HVAC led to the need of design an effective absorptive system for the different vehicle typologies. Thus, the main objectives to be achieved by this work are:

- The development of a process that optimize a given structure automatically taking into account the constraints for the project;
- The optimized solutions must fulfill the regulations of the Frontal Full Width Impact Assessment from Euro NCAP;
- For the lighter vehicle, the primary structure design should absorb the correspondent kinetic energy in the crash test;
- In the case of the vehicles with higher weight, a secondary structure should be designed to complement the energy absorption of the primary structure;
- The secondary structures must be responsible to lead the impact forces to the superior part of vehicle, namely to pillar A and rooftop regions to release tensions in the lower part of the vehicle preventing damages in this area;
- In the end, a comparison between the different solutions found for each type of vehicles have to be made in order to perceive the benefits or disadvantages of the secondary structure implementation.

The different vehicle typologies that will be tested for this purpose and their corresponding weights are in table 1.1.

Table 1.1: Different vehicle topologies and corresponding weights

Vehicle	Micro Car	Sports Car	Be 2.0	Big Sedan
Mass (kg)	1200	1400	1600	1800

The optimization process will include a multi-objective optimization algorithm coupled with 3D modelling tools and Finite Element Analysis, in order to have the most efficient structure, i.e, with the best energy absorption with lower decelerations during the impact.

1.4 Thesis Outline

Chapter 1 includes the initial motivations to begin the study of vehicle and occupant protection, the company and project environment that leaded to propose this work as well as the objectives to be achieved in the final solutions.

Chapter 2 contains the benefits and disadvantages of selected materials, main regulations regarding frontal impact, crashworthiness principles, some aspects about thin walled beams, material formulations to be used, the inclusion of heat affected zones in the soldering processes and, finally, the algorithms used to perform the optimizations.

In chapter 3 it is explained the process development used to optimize the structures. The materials used to perform the optimizations are selected. The script and software used in the process are detailed as well as the considerations made to achieve reliable results.

Chapter 4 shows the results for the various vehicle typologies. The optimized primary and secondary structures are detailed and the comparisons between energy absorption and the different weights are analysed.

In Chapter 5 the procedure to validate the material models is shown as well as one optimized solution to perform the necessary validation tests to compare the theoretical results with experimental data.

Finally, Chapter 6 shows the achieved conclusions, the main achievements and some proposals to complement this work.

Chapter 2

Background

The principles to implement and develop this work have to be analysed to explore the different available approaches and solutions to design a structure of this type. Thus, an analysis based on current bibliography was made to evaluate the benefits and disadvantages of selected materials, main regulations regarding frontal impact, crashworthiness principles, some aspects about thin walled beams, material formulations present in the used software, the inclusion of heat affected zones in the welding processes and the algorithms used to perform optimizations.

2.1 Materials

There have been many paradigm shifts in relation to road traffic and vehicle construction. The discovery of new materials and the improvement of others in the last few years increased the variety of ways to produce new automotive components. Thus, the designers must be aware of new trends and know how to select the best material to design a component that meets the requirements. This way, the most used materials in the automotive industry will be analysed in this section.

Since the early days of the automotive world, steel is the predominant material used to built components [10]. With the restrictions in regulations to increase the environmental protection, fuel savings and safety, automotive companies begun to search alternatives to steel in order to find lighter materials with great mechanical characteristics.

The research made in the last 40 years allowed to develop and introduce in the industry new aluminium and magnesium alloys, high strength steels and composites in order to reduce weight of automotive parts. The results show that 10 % less weight results in 6-7 % savings in fuel [11].

Besides the research in lightweight materials, improvements in vehicles such higher performances, larger sizes or equipment add weight to a vehicle. The added weight by the new technologies must be in equilibrium with the proposed solution: make the car's components as light as possible [12]. Table 2.1 resumes the weight reduction potential using new materials in comparison with conventional steel.

A brief description of these materials and their properties is presented next.

Table 2.1: Assumed weight savings for alternative materials [12].

Material	Relative Weight Savings	Weight Reduction Potential
Conventional Steel	0 %	1.0
High-Strength Steel Alloys	23 %	1.3
Aluminum Alloys	45 %	1.8
Magnesium Alloys	60 %	2.5
Plastic and Composites	50 %	2.0

Conventional Steel

As previously stated, steel was by far the material of election for a long time. The great versatility allied with low manufacturing cost made steel the most used material in automotive parts. In fact, steel is the cheapest material of all introduced in table 2.1. The stable supply, high formability, good corrosion resistance on coated steel and wide hardening ability are the main reason to place steel in the manufacturers first choice to produce new vehicles parts. Nevertheless, the high density and the risk of corrosion in uncoated parts caused a search to find lighter and more resistant alternatives [11].

High-Strength Steel Alloys

The desire to reduce weight in vehicles is the main reason of research in new High-Strength Steel (HSS) alloys. This way, automotive engineers are interested in this type of materials to replace conventional steel. Its advantages such as high tensile strengths, fatigue durability, high impact strength and large elongations at break, made HSS an excellent material to produce structural and energy absorbing parts. However, in some types of HSS there are some issues to solve regarding welding and low compatibility to mass production [11].

Aluminium Alloys

Despite being more expensive, aluminium is one of the most used alternatives to conventional steel. The cost associated with the necessity of special tools to weld or paint due to its poor characteristics in joint techniques made the implementation of this material more difficult. However, it has great characteristics such as high corrosion resistance and ease in recycling. The revolution in industry to search greener alternatives in all processes and products made aluminium a great choice for automotive parts. Furthermore, according to Nikolaevich et al. [11], an aluminium body is two times lighter than a regular steel body.

Magnesium Alloys

According to table 2.1 it is understandable that magnesium alloys are the most promising material in weight reduction due to their low density. The density of these type of alloys is 35 % smaller than aluminium and 4 times smaller than steel. Being very reactive, it is necessary to provide an appropriate coating to prevent corrosion and creep. The high material price associated with the treatments necessary to produce an alloy with great properties makes magnesium not attractive for mass production [11].

Plastic and Composites

Composites currently make about 8 % of a vehicle weight and 50% in volume [13]. The most used material of this type is the glass fiber reinforced thermoplastic polypropylene applied in non structural components such as door surrounds, instrument panel and bumpers. The ease in manufacturing and assembly of complex parts are the main advantages of this material. On other hand, carbon fiber reinforced polymer composites are more expensive but due to their high relation between strength and weight they have become a great solution for structural parts in high performance vehicles. The time required to prepare the material, price and recycling difficulties are the main disadvantages of carbon fibers [13].

2.2 Regulations

To ensure safety, governments and organizations have developed multiple programs around the world to regulate the minimum standards for homologation and certification in new vehicles. With several ratings, the consumers can have the perception regarding vehicle safety when buying a new vehicle. The increase of safety objectives made car's manufacturers to follow the market tendencies by producing safer vehicles.

To prove the vehicle performance safety in the event of an accident, tests have been planned and developed over time. These tests analyse the damage caused to eventual passengers using dummies equipped with accelerometers in several parts of the body that register accelerations during the crash event. To analyse intrusions suffered during the accident, some markers are placed in bodies to have a perception where are the principal sensible areas that might be a problem when the structure is impacted. By some calculations and comparisons, it is possible to analyse the performance of each vehicle in typical accident situations [14].

2.2.1 European Regulations

The United Nations Economic Commission for Europe (UNECE), the European regulator has created two main procedures related with vehicle safety and crash tests: the ECE-R94 for front collision and the ECE-R95 for lateral collision. In both procedures, several criteria are evaluated to perceive the vehicle safety level. The principal criteria evaluated to this purpose are chest deflection, head performance, thorax performance, chest deflection, abdomen protection and pelvis protection.

To measure these criteria, the tests performed regarding frontal impact consists of a vehicle that has to go against a rigid barrier with 40% front overlap at 56 km/h on the steering wheel side [15]. In the near future, it is predicted that the test into a full width barrier shall be performed to certificate a new vehicle [16].

Additionally, it is performed a lateral test that consists of a deformable barrier that goes perpendicularly against the vehicle at a velocity of 50 km/h [17]. Both tests are exemplified in figure 2.1.

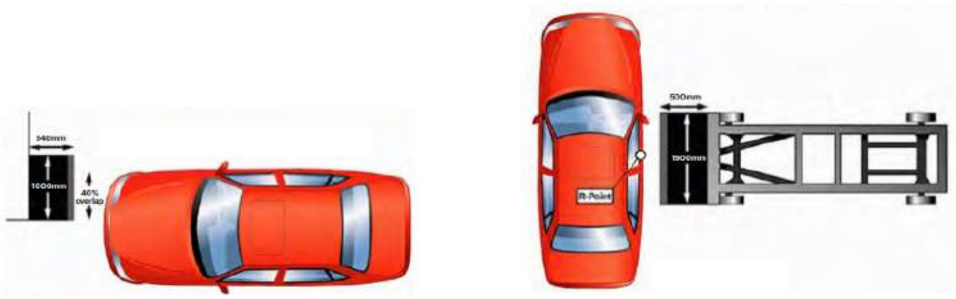

(a) Offset deformable barrier frontal test

(b) Mobile deformable barrier lateral test

Figure 2.1: UN Regulation 94 & 95 front and side impact crash tests [18].

2.2.2 Euro NCAP

European New Car Assessment Programme (Euro NCAP) was created to provide an independent safety evaluation of cars sold in Europe. This way, several additional tests are performed beyond European regulation. To evaluate the criteria descried previously, the tests described in tables 2.2 and 2.3 are performed [19].

Table 2.2: Euro NCAP frontal tests

	Offset-Deformable Barrier	**Full Width Rigid Barrier**
Velocity	64 km/h	50 km/h
Offset	40 %	-

The frontal tests ensure that the vehicle is stiff enough to guarantee the safety of a male body at 64 km/h and deformable at the same time to provide low decelerations on a small female body at 50 km/h. A compromise between these two requirements are the main goal to achieve the maximum rating score.

Table 2.3: Euro NCAP lateral tests

	Mobile Deformable Barrier	**Oblique Pole**
Velocity	50 km/h	32 km/h

Both insurance companies and most consumers are interested in these ratings. Since a vehicle rated with five stars represents a higher level of safety, thus minimizing injuries in occupants and costs.

Regarding the full width frontal impact, the criteria used to rate the vehicles about head protection in adults are the Head Injury Criteria (HIC) [19],

$$HIC = (t_2 - t_1)\left(\frac{1}{(t_2 - t_1)}\int_{t_1}^{t_2} a\,dt\right)^{2.5}, \tag{2.1}$$

where $t_2 - t_1 = 15$ correspondent the 15 ms interval and a is equal to the acceleration in g, maximum peak acceleration and mean acceleration during 3 milliseconds. The values allowed to have maximum rating score are summarized in table 2.4.

Table 2.4: Several criteria for NCAP head injury evaluation

Criteria	Maximum Value
HIC_{15}	700
Resultant Acc. 3 msec exceedence	65 g
Resultant peak Acceleration	80 g

In the next few years, the requirements will be improved to embrace new safety technologies in all vehicles, such as C-ITS (*Cooperative, connected and automated mobility*) , that will be responsible to improve significantly road safety, traffic efficiency and comfort of driving [19].

In the United States, the regulator is the NTHSA (*National Traffic Highway Safety Administration*). The test performed following the regulation FMVSS 208 to certificate a new vehicle regarding frontal impact consists on a test into a full barrier at 56 km/h [20].

2.3 Crashworthiness Principles

The main objective of an efficient crash structure is to absorb the maximum kinetic energy as possible without large decelerations. To evaluate the crash performance, several authors proposed an approach based on energy absorption efficiency and maximum peak crush force in the structure. Following Wade [21] and Tang et al. [22], the main parameters to evaluate the crash performance are the energy absorption (EA), average crush force (F_{av}), specific energy absorption (SEA) and crushing efficiency force (CFE).

The energy absorption can be expressed as the integral of the crushing force with respect to the displacement,

$$EA = \int_0^\delta F\left(x\right) dx, \tag{2.2}$$

where F(x) is the crush force and δ is the deformation distance.

The average crush force is given by the quotient between the energy absorption and the deformation distance,

$$F_{av} = \frac{EA}{\delta}. \tag{2.3}$$

With the specific energy absorption, it is possible to have a best comparison between the structures' performance. It is expressed as the ratio between the energy absorption and the system mass M as

$$SEA = \frac{EA}{M}. \tag{2.4}$$

The crushing force efficiency gives the notion about the structures' dynamics in a crashing event. It is given by

$$CFE = \frac{F_{av}}{F_{max}}. \tag{2.5}$$

The ideal crash structure should have a CFE close to unity, where the initial peak force is close to the mean force along the crushing time. If the average force is as high as the peak force, the energy absorption will be very satisfactory, because the area under the graphic is maximized. A CFE close to zero represents not only a initial large deceleration that can be harmful for the vehicle occupants but also a low energy absorption.

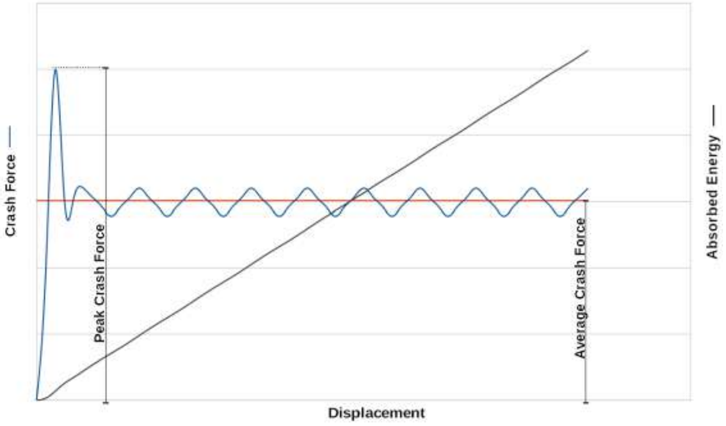

Figure 2.2: Representative force - displacement curve

Analysing figure 2.2, it is possible to understand that a higher mean crash force results in a higher absorbed energy. The area under the peak force is small compared with the rest of the area during the impact time, i.e., there is no noticeable change in energy absorption minimizing the peak force [22].

2.4 Thin Walled Beams

Thin walled beams are an object of study since the early days of the crashworthiness area. The ease to convert kinetic energy into plastic deformation energy, allied with the reduced mass, make this type of material the most common choice to design an energy absorbing system. Several studies have been developed to have a perception of which kind of parameters must be evaluated in the design phase. In frontal impacts, the principal phenomenon is the axial crushing [14].

The material absorbs the maximum energy when the plastic deformation occurs in a folding mode because this type of crush leads to the total deformation of the beam, maximizing the absorption of energy [23]. The manufacturer must ensure that the crush occurs in a controlled path, to prevent an eventual buckling of the total structure and loss of energy absorption capability.

To increase the performance, studies have been developed regarding the effect of thickness, cross sectional shape, mechanical triggers, reinforcements and tubes filled with different types of foams.

According to Kuznetcov et al. [24] a compromise between a heavier and stiff beam but with a low efficiency and a less robust beam with a low energy absorption but more efficient is the principal goal in this type of studies to size an absorbing structure.

The variable thickness along the axial tube direction has been studied resulting in a better absorption of energy [25] [26]. Other experiments show that variable thickness in square tubes along the cross sectional area have greater performance as exemplified in figure 2.3.

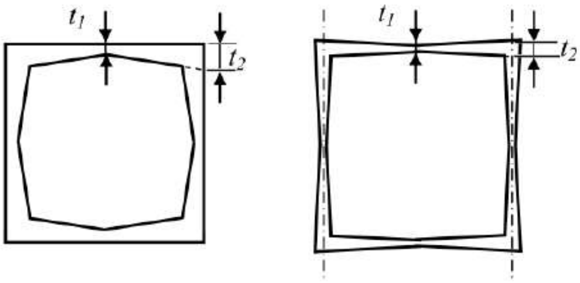

Figure 2.3: Quadrangular cross shape with different types of graded thickness (adapted from [26])

In order to improve bending resistance, Zhang et al. [27] concluded that beams with thin flanges and thick webs have a high SEA level.

The inclusion of foams inside the beams has demonstrated great increments in energy absorption and a decrease in the peak force [28]. In the current project, neither variable thickness nor reinforcement foams will be studied due to the large computational time required to analyse 3D elements.

The cross sectional shape is the most studied parameter. Quadrangular [29], circular [30] and hexagonal [31] cross shapes with or without intern reinforcements [32] have been studied, although, depending on the load factors, there are multiple combinations of solutions for the same problem due to the large quantity of variable parameters.

The effect of mechanical triggers have been proved to be a good approach in design because it leads to a controlled axial crushing, maximizing the energy absorption [33].

Based on these principles, several manufacturers have developed crash boxes and bumpers with different shapes and sizes. In figure 2.4 it is possible notice several prominences in the crash boxes corresponding to mechanical triggers and a front bumper with variable cross shape.

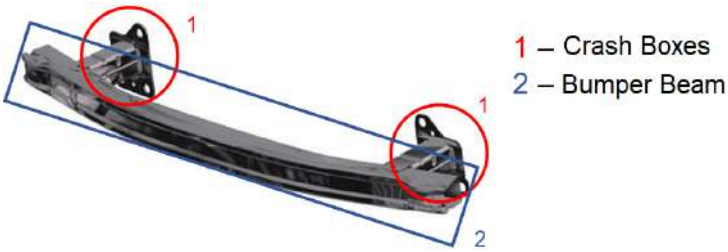

Figure 2.4: Complete aluminium bumper and crash boxes made from extrusions for the Renault Megane (adapted from [34])

Super Folding Elements

As previously stated, the axial crushing is the best way to absorb energy in this type of structures. Figure 2.5 demonstrates the typical behaviour of a folding structure under axial compression.

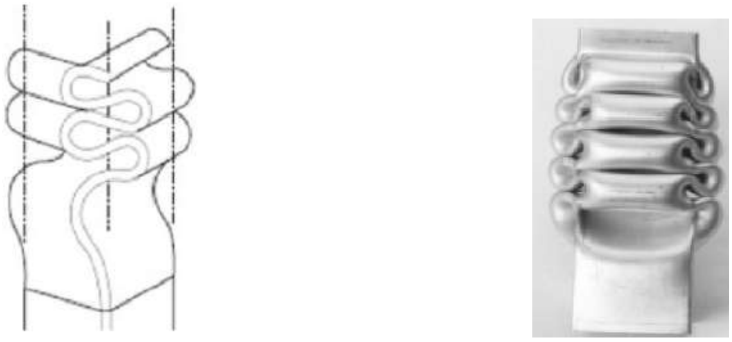

(a) Representative progressive folding

(b) Progressive folding in an aluminum beam

Figure 2.5: Axial collapsed beams [14]

The folding mechanism is one of the most studied fields in crashworthiness area. In order to develop a theoretic way to predict the behaviour of absorbing structures, several studies and models have been proposed to solve efficiently these problems. The development time of a crash structure can be significantly reduced with a credible mathematical tool capable of solve and approximate the theoretical solutions with experimental results.

Despite finite element analysis (FEA) being a helpful tool in the design stage, the computational effort required to compute crash tests is one of the main reasons that led authors to search for alternatives and complements to this method. Thus, several studies have been proven to be close to experimental results [35], [36] and [37]. The variation of cross shapes in crash boxes and bumpers are the main focus of these studies. With a rigorous prediction of the main force obtained during the impact, the energy absorbed by the structure can be extrapolated. A corresponding higher average force translates into a structure capable of absorbing more energy.

Several commercial softwares implement the super folding elements theory in tools that should be used before FEA. This way, a pre selected cross shape for each structure can be achieved, improving the solutions in the design stage.

The formulation for the absorbed energy begins with the bucking influence made by the different faces of a cross shape in axial compression [35]. The average force is calculated by the balance between external forces applied for compression and internal forces corresponding to membrane collapse and dissipated energy in folds. This energy balance is given by

$$E_{ext} = E_{int}, \tag{2.6}$$

where E_{ext} and E_{int} are the external and internal energy, respectively. The external energy is equal to the average force multiplied by the displacement. This displacement is measured as the distance corresponding to a unique fold 2H explained in figure 2.6.

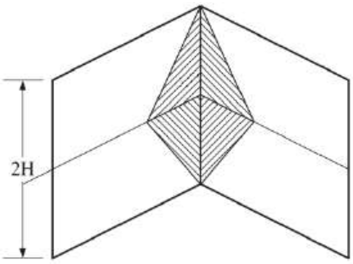

Figure 2.6: Fold with displacement 2H (adapted from [35])

The internal energy has two main contributions, one due to the membrane folding and the other to the bending energy of the tube. Substituting the displacement corresponding to the foldings and the two different types of internal energy, the equation (2.6) becomes

$$P_m 2H = \frac{1}{\eta}(E_b + E_m), \tag{2.7}$$

where E_b is the bending energy, E_m is the membrane energy, P_m is the mean crushing force and η is the effective crushing distance coefficient.

The bending energy in a tube is given by

$$E_b^{tube} = 2\pi M_0 B \tag{2.8}$$

where M_0 is the fully plastic bending moment and B is the sum of side and internal flange lengths. The fully plastic bending moment is equal to

$$M_0 = \frac{\sigma_0 t^2}{4}, \tag{2.9}$$

where σ_0 is the flow stress and t is the thickness. The flow stress is given by

$$\sigma_0 = \sqrt{\frac{\sigma_y \sigma_u}{1+n}}, \tag{2.10}$$

and σ_y is the yield stress, σ_u is the ultimate tensile stress and n is the strain hardening exponent.

The dissipated energy by the membrane is dependent on flanges present in the cross shape. This is the principal factor that influences the average force value. In the simplest case of a rectangular cross section, the membrane energy has to be calculated considering four right angles. This way, the absorbed energy is equal to four times the energy correspondent to a section with two membranes performing a right corner between them.

The absorbed energy by a right corner is

$$E_m^{rc} = 4M_0 \frac{H^2}{t}. \tag{2.11}$$

Thus, the final expression that traduces the average force in an axial solicitation of this type is given by

$$P_m 2H\eta = 2\pi M_0 B + 4(4M_0 \frac{H^2}{t}). \tag{2.12}$$

The value correspondent half wavelenght H can be calculated through the stationary situation given by $\frac{\partial P_m}{\partial H} = 0$. The value obtained for H is

$$H = \sqrt{\frac{B\pi t}{8}}. \tag{2.13}$$

Finally, the average crush force P_m is

$$P_m = 4.707\sigma_0 t^{1.5} B^{0.5} \pi^{0.5}. \tag{2.14}$$

There are numerous equations for other types of joints, and their effects on the average crush force have been studied.

Tran et al. [35] studied cross shapes with criss cross shapes, three panel angle, t-shape, four panel angle and right corners. The effect of varying the angle in 3 panel angle elements was also studied [36]. In figure 2.7 it is exemplified the different shapes mentioned above.

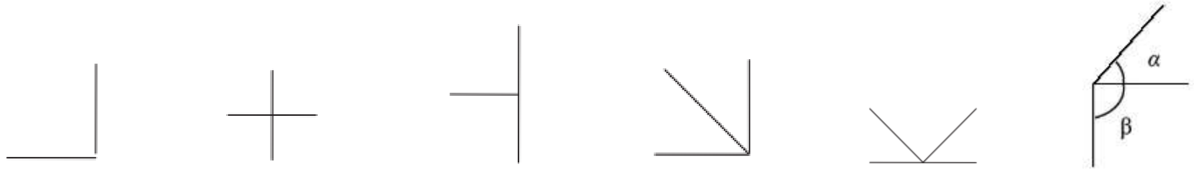

(a) Right-corner (b) Criss-cross (c) T-shape (d) 3-panel (e) 4-panel (f) 3-panel angle

Figure 2.7: Cross-sectional geometry of tubes and typical angle elements (adapted from [35], [36])

The hexagonal shapes with different types of reinforcements were studied by Qiu et al. [37]. The figure 2.8 traduces the usage of this type of simple elements in more complex cross shapes.

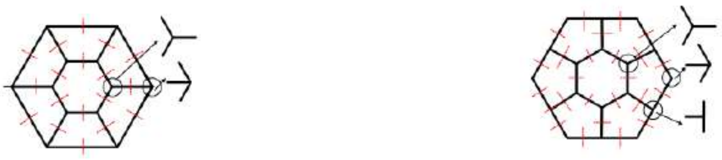

(a) Hexagonal cross shape example 1

(b) Hexagonal cross shape example 2

Figure 2.8: Division of constituent elements in multi-cell hexagonal tubes (adapted from [37])

By changing the geometries and joining various types of flanges, it is possible to obtain complex geometries with higher average forces. After finding the corresponding equations to calculate the average forces, it must be performed a study to evaluate the increase in mass due to the addition of more flanges. The compromise between these two factors must be achieved. The structure that has a better performance in both factors will be chosen to the next design stage.

Despite these equations being a helpful tool in the design phase, they only exhibit good correlations in quasi static tests. Accordingly to Tran et al. [35], the average force calculated by the resultant equations must be multiplied by a dynamic factor λ to approximate experimental data to theoretic results. Thus, the dynamic crush force is given by

$$P_m^{dyn} = \lambda P_m^{static}. \tag{2.15}$$

Concluding, the cross shape efficiency in energy absorbing is directly dependent of the material characteristics, the cross shape dimensions and thickness. This method is a helpful tool, nevertheless it cannot substitute the finite element analysis or experimental tests. Furthermore, with these equations it is not possible to predict the maximum crush force necessary to induce bucking in the structures. The Simplified Super Folding Elements (SSFE) is a tool to predict SEA, but a higher value of this parameter is obtained in a structure with a larger thickness which leads to an increase in peak force, thus reducing CFE. Being one of the most critical parameter in crashworthiness area, it becomes clear that there is a need for a methodology incorporating both FEA and SSFE.

2.5 Material Characteristics

2.5.1 Material Law

The material law to be used depends on the initial considerations and its applicability along the project. Thus, the chosen model must perform the best approximations in all stages of material deformation in order to have satisfactory results.

Through the stress strain curve, represented in figure 2.9, it is possible to define the properties of the material and its behaviour during all stages of deformation. Extrapolating these properties, it is possible to predict the material behaviour in more complex situations.

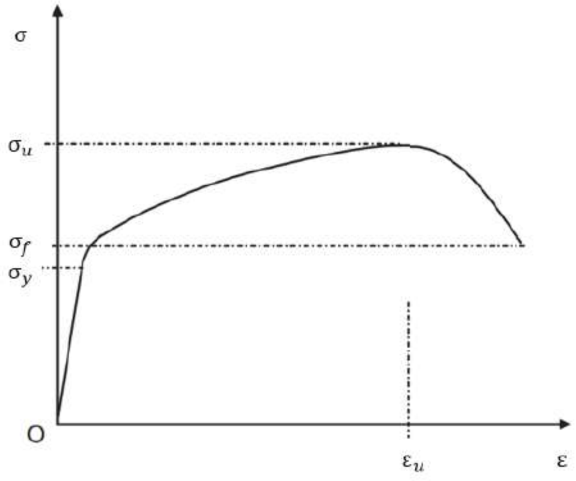

Figure 2.9: Typical stress strain curve

These type of curves represented in figure 2.9 are the typical result of an axial tensile test performed in an isotropic material. Thus, between the point O and the yield point σ_y the material is in the elastic regime. After this point, is in plastic regime presenting a non-linear behaviour. The ultimate tensile strength is given by σ_u as well as the strain at this point ε_u. In the end of the curve it is obtained the maximum displacement at failure and the strength at failure σ_f.

Depending on the analysis to be performed, the plastic regime modulation is very important because the main differences between approaches are defined in this regime. The elastic behaviour is common across all models being defined by the Hooke's Law [38]. Analysing the models provided by $Altair^{®}RADIOSS^{®}$, which is a leading structural analysis solver for highly non-linear problems under dynamic loadings, it is possible to define the best approach to perform a crash test on the structure. Thus, the relevant models available to perform the material formulation in this solver are the Elastic Plastic Piecewise Linear Material and the Johnson Cook Material Law [38].

Elastic Plastic Piecewise Linear Material

The Elastic Plastic Piecewise Linear Material defines the stress strain curve from the strain-rate value. This dependence is only notory in plastic regime, since the elastic regime is defined by the Hooke's law as mentioned before. Thus, for each strain-rate value exists a different curve and, consequently, a different yield stress in each case.

With this approximation, the maximum value of the stress strain curve can not be calculated due to the strain-rate influence. The curves presented in figure 2.10 exemplify the dependency of the material on the strain-rate value.

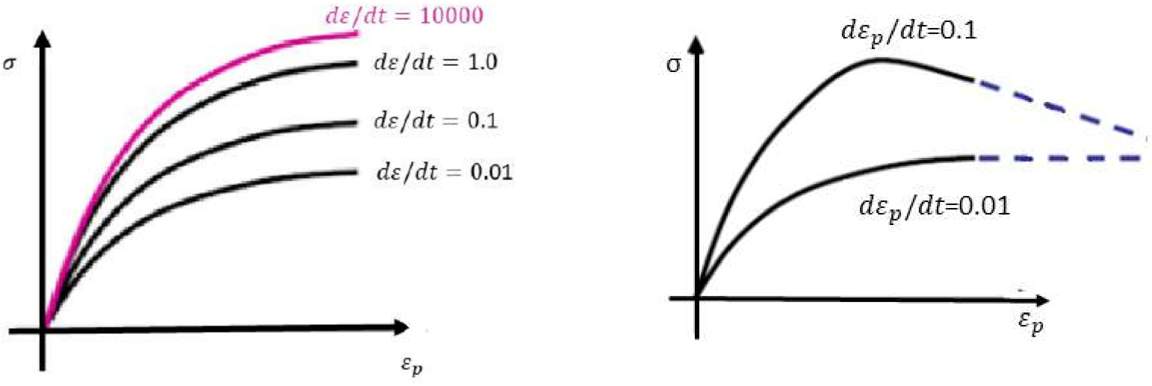

(a) Law 36 application

(b) Law 36 application limits

Figure 2.10: Elastic plastic piecewise linear material from $RADIOSS^{®}$ [38]

In crash simulations, the material behaviour is mostly plastic with large deformations. The absorption of energy is efficient if the material is capable to deform without failure in large strains. This formulation is poor to module this type of tests, so the solution in a crash test with this formulation does not have a realistic solution [38].

Johnson Cook Material Law

The Johnson Cook formulation [38] implements an adequate model for isotropic materials in elastic-plastic regimes. In this law, the plastic behaviour is only considered after the yield point. Before this point it is considered that the material has a fully elastic behaviour.

Since the interest of this project is mainly focused in energy absorption, the study will be performed regarding plasticity behaviour. Therefore, the Johnson Cook material law has in consideration the effect of the strain rate and the temperature. This formulation is valid for shell elements, truss and beams elements, which will be the case of the structure to be studied.

The stresses during the plastic deformation can be described by

$$\sigma = (a + b\varepsilon_n^p)\left(1 + c\ln\frac{\dot{\varepsilon}}{\dot{\varepsilon_0}}\right)\left(1 - T^{*^m}\right), \tag{2.16}$$

where σ is the flow stress, ε the plastic strain, a the yield Stress, b the hardening modulus, n the hardening exponent, c the strain rate coefficient, $\dot{\varepsilon}$ the strain rate and $\dot{\varepsilon_0}$ the reference strain rate. The temperature exponent is given by

$$T^* = \frac{T - 298}{T_{melt} - 298}, \tag{2.17}$$

and

$$T = T_i + \frac{E_{int}}{\rho C_\rho (Volume)}, \tag{2.18}$$

where T_{melt} is the melting temperature, T_i the initial temperature and ρC_ρ the specific heat per unit of volume.

Analysing equation (2.16), the flow stress (elastic + plastic regime) is influenced by three parameters: plastic strain, strain rate and temperature. The strain rate effect is modelled with several parameters to achieve the best approximation. If this effect is taken into account, the yield stress will be dependent on the velocity imposed on material, i.e, the structure will become more rigid. This phenomenon is exemplified on figure 2.11.

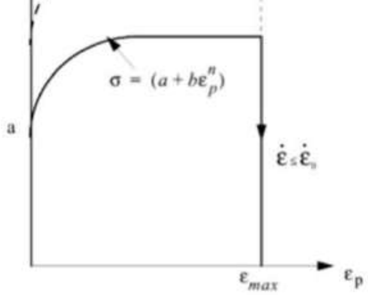

Figure 2.11: Strain rate effect in yield stress [38]

Although, a simplification can be made to remove the temperature and strain rate effect in order to achieve quicker but reliable results. Regarding the strain rate effect, Chen et al.[39], concluded that several aluminium alloys can be modelled as strain rate insensitive. The tests will be performed at room temperature (298 K) so temperature effects can be neglected. Concluding, the final formula to model the material behaviour during the plastic formulation can be approximated as

$$\sigma = (a + b\varepsilon_n^p)\,. \tag{2.19}$$

2.5.2 Heat Affected Zone

The Heat Affected Zone (HAZ) has special importance when several components of a structure are welded. When the joint is made, the band of material near the melting zone is highly affected promoting a degradation of its mechanical properties. The micro structural alterations are the main explanation to the changes in the macro characteristics of the material such yield stress and brittleness.

Figure 2.12 exemplifies the heat effect on metals with temperature treatments. The high temperatures remove the hardening made in these treatments and increase the ductility in the affected zone.

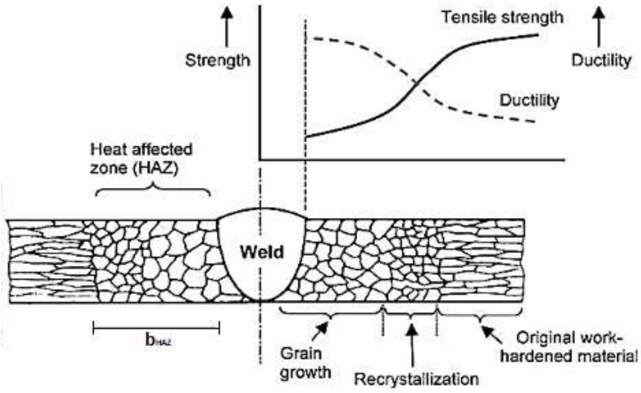

Figure 2.12: Weld area, heat affected zone and properties description (adapted from [40])

For several aluminium 5xxx and 6xxx series alloys, the reduction of the properties can be from 30% to 50% when joined by fusion welding [41]. With this high percentage, the heat effect cannot be neglected.

According to *Eurocode 9: Design of aluminium structures* [42], it is possible to obtain the properties reduction in these areas. The reference values for yield strength in several aluminium alloys can be obtained. Comparing the values between the affected and non affected areas, the reduction in yield strength is in the order of 40 %.

Moreover, the altered properties are directly dependent on the structure characteristics and welding joints. The most important parameter to take into account is the thickness. A larger piece will require more welding time and material deposit, resulting in a larger affected area.

In this project, the bumper will require two welding zones corresponding to the union between the crash boxes and the frontal structure. In order to have the perception of which area have to be considered in numerical simulations, the distance between the welding lines and the end of the affected area b_{HAZ} is summarized in table 2.5.

Table 2.5: Heat Affected Zone length by thickness values for MIG welding [42]

Thickness (mm)	b_{HAZ}
$0 \leq t \leq 6$	20
$6 \leq t \leq 12$	30
$12 \leq t \leq 25$	35
≥ 25	40

If TIG is used, the value for b_{HAZ} is equal to 30 mm in thicknesses between 0 and 6 mm due to the additional heat used in this process.

2.6 Finite Elements Analysis

The finite element method became the main analysis tool in the field of structural engineering. With the development of larger and faster processing capacities, the efficiency between reliable results and processing time has highly increased. The ease in testing the components before manufacturing made the design cycle become much faster. Crash tests are computationally time-consuming, but the dramatic reduction in costs and manufacturing time led to a great increase in the vehicle safety levels [43].

Since FEA models are analysed for a concise perception of reality, engineers need to be sure at the end of the development phase that the predictions are accurate. Similarly, if an improvement or modification is to be made, there must be a plan to ensure that any change in design do not delay the development or analysis of the product. If a modification is made at a later stage, it is necessary to make sure that the model is robust, that is, any change should not produce effects that are very different from those initially expected [14].

To fulfil the objectives above, a prior analysis of the algorithms and approaches should be done to model the crash system properly. In order to achieve reliable results, the choice of analysis type should take into account the behaviour of the material in the test scenario.

Firstly, it is necessary to understand if the analysis will be linear or non linear. In a linear analysis, it is assumed that the material will always be below the yield point, presenting an elastic regime. This type of analysis is the lighter solution in terms of computational effort. As previously mentioned, crash systems are made to absorb energy in the plastic regime, i.e., the material is always beyond the yield point. With this, it is concluded that the best analysis to be made will be non-linear, which manages to cover large deformations such as those the vehicle is subjected during impact [44].

Figure 2.13 is an example of a crash simulation computed through a finite analysis software.

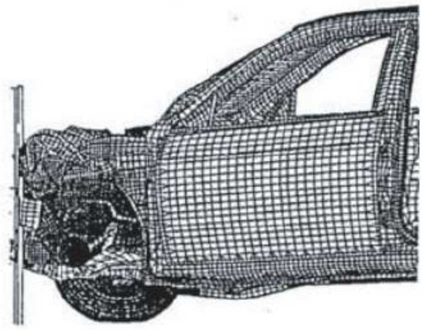

Figure 2.13: Collapse mode prediction for a full car FE model (adapted from [14])

In a crash scenario, the problem needs a solution of the type $\sum \vec{F} = m\vec{a}$ and $\sum \vec{M} = I\vec{a}$. The initial velocity and the inertial forces have a high contribution for the solutions. The best approach for an impact scenario is a dynamic analysis where it is possible to choose between an implicit or an explicit solver. The implicit analysis is stable and reliable, being used in dynamic and static studies. In static or quasi static tests, the best solution is to perform an implicit analysis. Due to large time required to solve these tests, in an explicit analysis the computational time required will become even larger because the time domain being split in an enormous quantity of intervals increase drastically the computing time. The implicit analysis has the capacity to solve these problems quicker with reliable results. In an explicit analysis, the results are computed at each time-step based on the previous time-step while in implicit analysis all systems of equations are generated and solved simultaneously. The implicit analysis requires a large usage of memory and CPU in computations when the material behaviour is highly non linear and the number of elements is too high [45].

On the other hand, the explicit analysis covers situations in which the implicit analysis is not efficient to solve. This analysis is very efficient in cases where there are many contacts and elements since contact algorithms are very efficient in explicit programs.

Figure 2.14 shows that when the complexity of the system and the number of elements and degrees of freedom become large, the computation cost increases more drastically in the implicit analysis, so it is easy to conclude that the most utilized scheme is the explicit time integration for crash analysis.

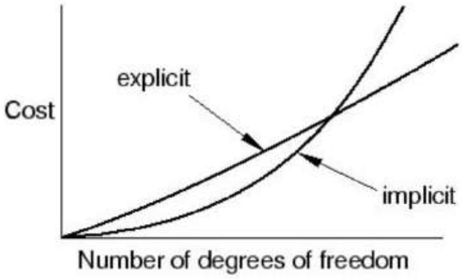

Figure 2.14: Difference in calculation cost between implicit and explicit solver [46]

In an explicit integration, the central difference scheme is implemented. The following equations are solved to calculate the displacements in each step time.

The acceleration at each time instant can be computed through the second Newton's law as

$$\ddot{u}_n = \frac{(f^n_{int} + f^n_{ext})}{m}, \tag{2.20}$$

where f^n_{int} and f^n_{ext} are the internal forces and external forces, respectively.

As the integration is explicit, i.e, the acceleration at each time step is known, it is possible to calculate the velocity $\dot{u}_n$ and the displacements u_n, respectively by

$$\ddot{u}_n = \frac{1}{h_{n+\frac{1}{2}}}(\dot{u}_{n+\frac{1}{2}} - \dot{u}_{n-\frac{1}{2}}) \Leftrightarrow \dot{u}_{n+\frac{1}{2}} = \dot{u}_{n-\frac{1}{2}} + h_{n+\frac{1}{2}}\ddot{u}_n \tag{2.21}$$

and

$$u_{n+1} = u_n + h_{n+1}\dot{u}_{n+\frac{1}{2}}, \tag{2.22}$$

where the time steps are given by $h_{n+\frac{1}{2}} = \frac{(h_n + h_{n+1})}{2}$ and $h_n = t_{n+1} - t_n$.

The computation is made in half of the time interval because the algorithm is more efficient. The flow chart of the whole process is shown in figure 2.15.

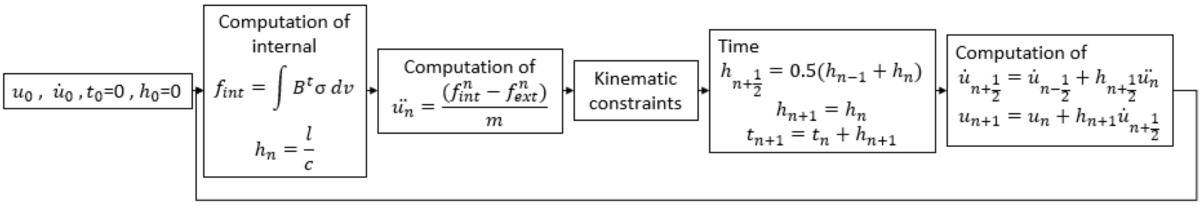
u_0 , $\dot{u}_0$, t_0=0 , h_0=0
Computation of internal
$f_{int} = \int B^t \sigma \, dv$
$h_n = \frac{l}{c}$
Computation of
$\ddot{u}_n = \frac{(f^n_{int} - f^n_{ext})}{m}$
Kinematic constraints
Time
$h_{n+\frac{1}{2}} = 0.5(h_{n-1} + h_n)$
$h_{n+1} = h_n$
$t_{n+1} = t_n + h_{n+1}$
Computation of
$\dot{u}_{n+\frac{1}{2}} = \dot{u}_{n-\frac{1}{2}} + h_{n+\frac{1}{2}}\ddot{u}_n$
$u_{n+1} = u_n + h_{n+1}\dot{u}_{n+\frac{1}{2}}$

Figure 2.15: Explicit integration flow chart

As the time intervals are constant, h can be expressed as Δt. The stability of the solution depends on numerical and physical factors. The size of the smallest element and the sound propagation speed limits the time incremental step as

$$\Delta t < \frac{l_c}{c}, \tag{2.23}$$

where l_c is the critical length of the element and c is the sound speed. For undamped systems, the condition for stability can be expressed as [45]

$$\Delta t < \frac{2}{\omega_{max}}, \tag{2.24}$$

where ω_{max} is the highest angular frequency in the system. In case of an elastic element, the incremental time is computed as

$$\Delta t = \frac{l_c}{c} = \frac{l_c}{\sqrt{\frac{E}{\rho}}}, \tag{2.25}$$

being E the elasticity modulus and ρ the specific weight [45].

2.7 Optimization Algorithms

Several algorithms have been proposed to solve optimization problems over time. The need for an optimal solution in engineering, finance or medicine problems where many parameters or variables are included have led to the creation of tools that analyse the variable combinations in convergence areas to reduce the computational effort in calculations.

There are algorithms that begin with the creation of random solutions until finding a convergence or, on other cases, searching for tendencies on solutions depending on variations in the initial variables. Thus, optimization algorithm are particularly beneficial in problems with large quantities of variables. For example, solving a problem with 200 variables with 10 possible values for each one, it will take 10^{200} computations if all combinations are tested. The high number of calculations will become impracticable. Furthermore, in complex environments where computations are slow and the prediction is difficult to find, the development of these optimization methods become of central importance.

2.7.1 Single-objective Optimization Algorithms

Single objective optimization algorithms have the main goal of minimizing or maximizing the value of a single function. These optimization methods may come from heuristic processes or gradient-based algorithms. The major problem with all these methods is the tendency to find a local rather than global extreme [47].

Analysing figure 2.16, it is easy to understand that in a point to point search algorithm finding the global minimum depends on the start point. If the starting point is within the grey region, the convergence will define the minimum as the point A while if the starting point is defined in the green zone, the convergence will be at point B. Thus, the need to find search methods that define several starting points and compare the solutions between each iteration at different start points becomes necessary if a global optimum is desired.

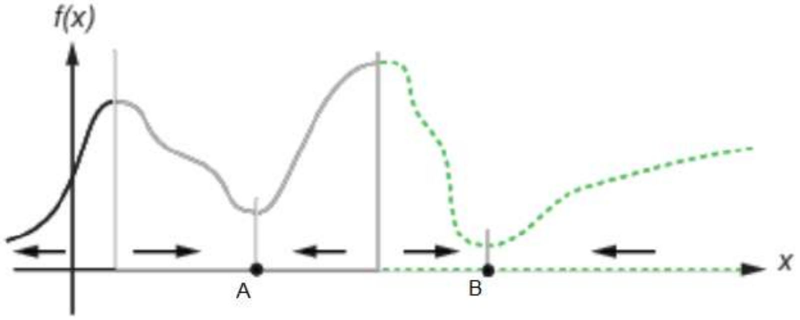

Figure 2.16: Global minimum vs global maximum search principle [47]

To solve these problems efficiently, several stochastic methods revealed a great improvement in finding global extremes. Actually, some commercial software use heuristic methods with stochastic search by parallel computations and several stating points to ensure that the initial search and the final convergence is more accurate [47].

Additionally, methods based on evolutionary biology called genetic algorithms are another alternative to either gradient or heuristic search methods. The main advantage of these approaches is to use a population of individuals at each iteration instead of using a single point as used in point-to-point search methods. At the end of the optimization it is expected that the population generated will have individuals with the best capacities. Thus, it is ensured that if there is only one global solution, the convergence will be in the region of the final population. Furthermore, if there is more than one solution, it is expected that the algorithm captures all optima in the final population [48].

2.7.2 Multi-objective Optimization Algorithms

In the case of optimization in crashworthiness area, the ideal is to maximize the SEA and the CFE simultaneously. This way, the choice of an effective algorithm that deals with several objective functions is naturally important. The multi-objective optimization functions deal with with multiple functions that are usually conflicting with each other. Thus, there should be a compromise between the ideal value of the functions. This problem exists because it is expected that a maximization in one objective causes a detriment in the other objectives. The typical formulation for a multi objective problem is given by

$$\left.\begin{array}{llr} Minimize/Maximize & f_m(\boldsymbol{x}), & m = 1,2,...,M; \\ subject\ to & g_j(\boldsymbol{x}) \geq 0, & j = 1,2,...,J; \\ & h_k(\boldsymbol{x}) = 0, & k = 1,2,...,K; \\ & x_i^{(L)} \leq x_i \leq x_i^{(U)}, & i = 1,2,...,n. \end{array}\right\} \tag{2.26}$$

It is always necessary to define the M objective f functions corresponding to the expressions that will be maximized or minimized. If the optimization formulation is constrained, the equality and inequality functions, $h(x)$ and $g(x)$, are evaluated, as well as the upper and lower bounds, $x_i^{(L)}$ and $x_i^{(U)}$.

If a solution does not fit the domain defined by the constraint functions $g(x)$ and $h(x)$, it is called *infeasible solution*. The unique relevant solutions to the optimization problem will be the *feasible solutions*, that satisfy the constraint functions [48].

According to Deb [48] it is possible convert any minimization problem to a maximization problem and vice versa multiplying any objective function by -1. Similarly, the inequation $g(x)$ can be changed from a function ”minor than” in ”major than” the same way.

There are two distinct possibilities to find the best solutions in a multi objective problem. The first one begins with the weight definition given at each objective function and then define a full objective function that will be the weighted sum of all objective functions with the respective weights. Thus, a multi objective problem becomes a single objective problem. In this approach, the algorithm does not check the trade-off between the objectives, since this is already defined before the start of optimization when the weights are defined. This case is exemplified in figure 2.17(a).

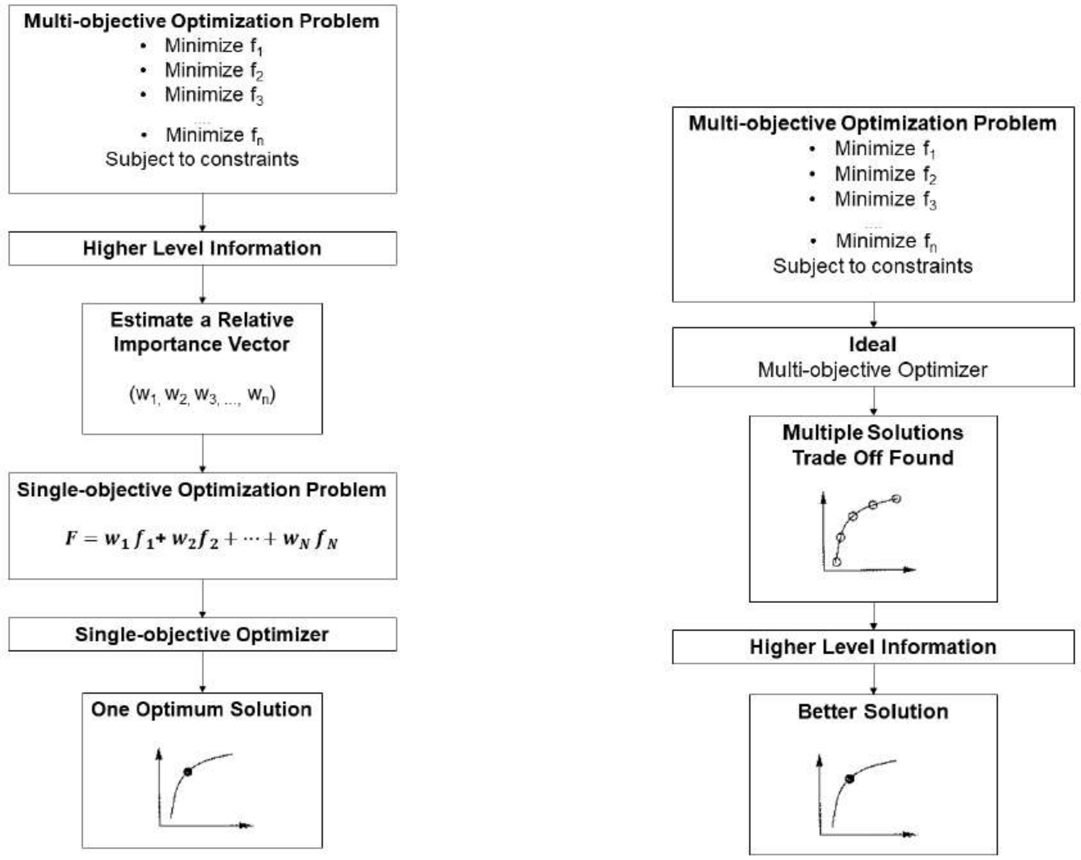
Multi-objective Optimization Problem
Minimize f_1
Minimize f_2
Minimize f_3
Minimize f_n
Subject to constraints
Higher Level Information
Estimate a Relative Importance Vector
$(w_1, w_2, w_3, \ldots, w_n)$
Single-objective Optimization Problem
$F = w_1 f_1 + w_2 f_2 + \cdots + w_N f_N$
Single-objective Optimizer
One Optimum Solution
Multi-objective Optimization Problem
Minimize f_1
Minimize f_2
Minimize f_3
Minimize f_n
Subject to constraints
Ideal
Multi-objective Optimizer
Multiple Solutions Trade Off Found
Higher Level Information
Better Solution

(a) Preference-Based Multi Optimization Optimization Procedure

(b) Ideal Multi Optimization Procedure

Figure 2.17: Multi-objective flow charts (adapted from [48]])

Additionally, when it is not possible or desired to define the relative weights of each objective before the calculation, the solution presented in figure 2.19(b) becomes the most appropriate approach. In these problems, the constraints and the objective values are obtained at each iteration and the algorithm finds the solutions in the Pareto front, i.e., the chosen solutions are the ones that present the best compromise between objectives. Finally, the best solution is chosen due to several external comparisons with additional information to decide the best trade off within the presented values [48].

Pareto Analysis

The Pareto front is a graphical tool created to express the best trade off found by the optimizer. During optimization, the search algorithm tries to find the non dominated solutions, i.e, the values corresponding to the minimum in all objective functions.

In order to define the dominance between points, equation (2.27) traduces these relations.

The point A dominates the point B when:

$$\left.\begin{array}{ll} f_m(A) \leq f_m(B) & \text{for all } m \\ f_n(A) < f_n(B) & \text{for several } n \end{array}\right\} \tag{2.27}$$

This is the equivalent to state that A dominates B exactly when B is inferior to A. Additionally, a non dominated set of points Q is a set of in P that are non dominated for any point in P.

Figure 2.18 exemplifies the optimization result in a multi objective problem. The points in the black line - Pareto front, are the non dominated solutions.

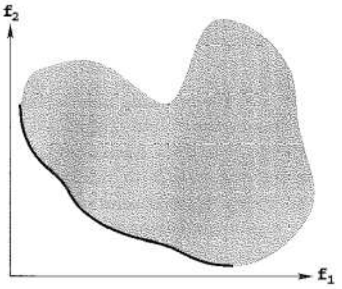

Figure 2.18: Pareto front example [47].

The convex shape of the Pareto front comes from the conflict between the two objective functions. A minimization in one function implies the maximization on another and vice versa as stated previously. Besides that, the front shape is dependent on each objective function and the constraints applied. If several constraints are present in the optimization process, the solutions domain will be defined by a constrained front. The resulting frontier will be reduced, corresponding to the *feasible* solutions.

In figure 2.19 it is evident the effect from the constraints in the final solutions.

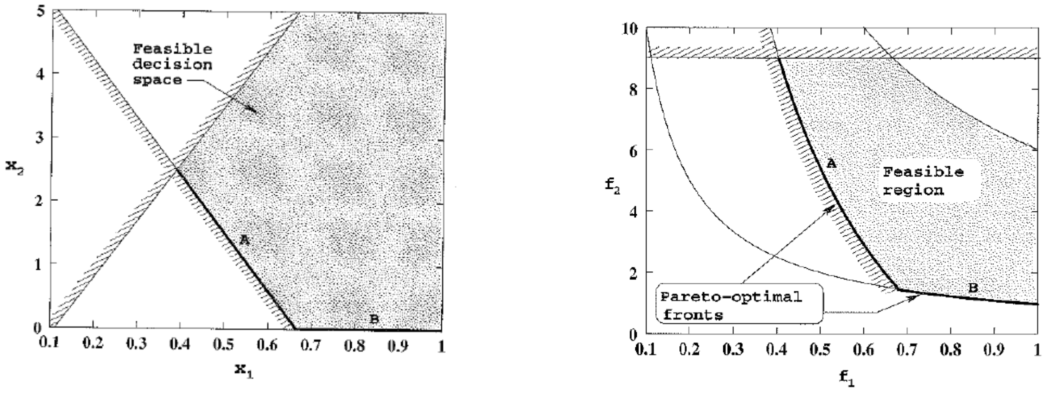

(a) Design Space Constraints

(b) Solution Constraints

Figure 2.19: Constrained optimization [48].

Multi Objective Genetic Algorithm Optimization

As explained in the beginning of this section, genetic algorithms [48] are a powerful tool in the process of finding global minima or maxima.

If finding a global minimum in a single objective optimization can be an arduous task, in case of a problem with various objectives, this task can become even more complex.

In the crashworthiness area, several studies have implemented the Non Dominated Sorting Genetic Algorithm (NGSA II) to size absorption structures [49] and front structures for full with impact and offset impact [50], achieving excellent results.

The NGSA II implemented by the function *gamultiobj* in $MATLAB^{\circledR}$ determines at each iteration the individuals with lower rank. This parameter is defined as the set of non dominated solutions by their neighbours. A lower rank implies a better chance to pass the correspondent solution for the next generations. In figure 2.20 it is exemplified the ranking given to several fronts.

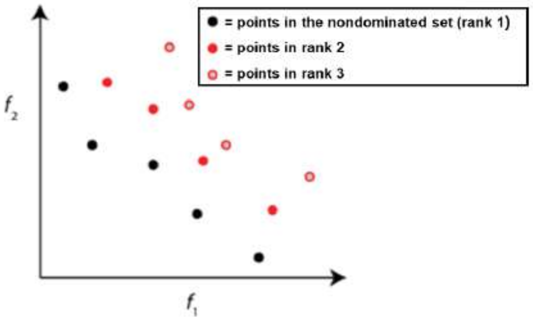

Figure 2.20: Pareto front ranks [47]

This way, it is ensured that the best solutions are passed through the next generations. From the control made by the initial parameters it is possible to achieve a better convergence of the Pareto front. These parameters are the population size, the number of generations and the stopping criteria.

Thus, defining the appropriate size of each population ensures a continuity of solutions, preventing the algorithm from finding a local optimum. It must be found a compromise between a large population to ensure convergence and a small population to reduce computational cost. The following generations are produced by evolutionary processes such as cross over and mutation. The best solution in each generation is evaluated and passed to next generations, repeating the cycle until a good convergence.

The cross over processes and elite individuals are the main responsible driving the convergence. These two processes ensure that the individuals with best characteristics are passed to the next generations, i.e., at each iteration the convergence of solutions is closer to be achieved.

Cumulatively, mutation processes ensure that there is a degree of randomness in the process, increasing the diversity of solutions. Thus, it allows to enhance the search radius, providing a robust global solution, not diverging to local minimums.

To define the stopping criteria and output the best solutions, it is necessary to provide the number of generations needed to evaluate the Pareto spread. To stop the optimization, the spread along the Pareto front must be less than x in m generations. The values of x and m are defined by the user [47].

Chapter 3

Implementation

In this chapter it will be presented the materials used to perform the optimizations. The different considerations such as the the signal filtering, the mesh convergence, the inclusion of the heat affected zone and the software used to build the optimization procedure are explained. Finally, the script organization to implement the optimization algorithm is presented.

3.1 Material Selection

The selection of materials should take into account costs, design principles, environmental conditions and manufacturing constraints. With the world focused on green choices, new products in markets must have a reduced ecological footprint. To build an electric car, factories must take into account weight reduction to maximize autonomy and reduce energy consumption.

Composites, High Strength Steel and Magnesium alloys are a great choice when costs are not a constraining factor. The lightweight factor of this type of materials is great, but the associated costs are the main reason that postpone the widespread implementation of these materials in industries. Steel is the cheapest material, but its weight reduces the possibility of making the vehicle lighter.

Due to manufacturing constraints, stamping process is not possible, so the choice is to produce the components by simpler processes. Thus, with the previous analysis of the materials made in chapter 2.1, the best choice to achieve design objectives is aluminium.

Aluminium is widely used in a variety of automotive components and its features are excellent for manufacturing the structure. The wide variety of alloys and properties are the main reason for choosing this material. The extraction of aluminium is a high energy process, but the possibility of recycling the material is a chance to reduce the expended energy and the emitted gases without quality loss in the final product [51]. The material characteristics to take in account when a crash system is being built are the capacity to absorb energy, its durability and the ease of fabrication.

Aluminium extrusion allows to produce almost any cross section design [34]. The shaping capacity with the cost-efficiency and the ease to riveting, welding, brazing or soldering makes this material ideal to make the structure. The resistance to corrosion comes from the fact that when the raw aluminium surface is exposed to air, a layer of aluminium oxide is created giving the material a high natural resistance [52]. An example of several complex extrusion shapes in aluminium are exemplified in figure 3.1.

Figure 3.1: Aluminum extrusions [53].

In order to maximize the properties of this material, some materials are added to aluminium in order to make alloys with improved capabilities depending on the final application. The different types of aluminium alloys are referred in European Standards by four digits according to its constitution. The most common used alloys in automotive industry are the 6xxx and 7xxx. However, the 6xxx alloys are more easily extruded than 7xxx. With several types of heat treatment, it is possible to achieve the properties required for the bumper and crash boxes [34].

Thus, the characteristics of materials chosen to perform the numerical simulations are in table 3.1. The main characteristics such as Yield Strength (YS), Ultimate Tensile Strength (UTS) and Elongation at break (A) of each alloy are given as well as the respective values for the HAZ.

Table 3.1: Selected materials for optimization comparison (adapted from [42])

Material	YS (MPa)	UTS (MPa)	A %	YS - HAZ (MPa)	UTS - HAZ (MPa)
6060 T64	120	180	12	60	100
6061 T4	110	180	15	95	150
6061 T6	240	260	8	115	175
6082 T6	250	290	8	125	185

The material choice was made taking into account the most relevant characteristics for a crash test. As stated previously, the desired material has to be ductile and with a high yield stress to increase the area under the stress-strain curve, that is a measure of the absorbed energy. The tempers used to treat the materials in this design are in table 3.2.

Table 3.2: Aluminum tempers (adapted from [54])

Temper	Description
T4	Solution heat treated and naturally aged
T6	Solution heat treated and fully artificially aged
T64	Solution heat treated and artificially under-aged

The 6060 T64 and 6061 T4 alloys have a lower yield strength but a higher ductility, while the 6161 T6 and 6082 T6 alloys have the inverse characteristics. These choices were made to provide a wide range of solutions and have the perception of which properties have the major influence in the final results. With different characteristics, it is expected a wider spread in Pareto solutions.

3.2 Optimization Procedure

In this section it will be introduced the optimization process for both structures. In order to achieve final results, several steps were performed from the creation of geometry to the analysis of final results by the developed script.

3.2.1 Setup of $\mathrm{CATIA^{TM}\ V5}$

The $CATIA^{TM}\ V5$ development software is a powerful 3D modelling tool that supports almost any type of geometry. This program is used to generate the geometries that will serve as input for finite element analyses.

The initial geometry for analysis and optimization was designed in a parametrized way. By changing the parameters through a macro that is controlled externally by $MATLAB$, it is possible to change the geometry easily. The parameters to change by the program in a file with one structure and two structures are presented in figure 3.2 and 3.3, respectively as well as a brief explanation in table 3.3.

Table 3.3: Description of the parameters used to build the geometry

Parameter	Description
t	thickness
tl	total length
tw	total width
bh	height of the bumper
lc	length of the crash box side
rb	bumper radius
lb	width of the bumper
dcb	distance between crash boxes
d	distance between structures

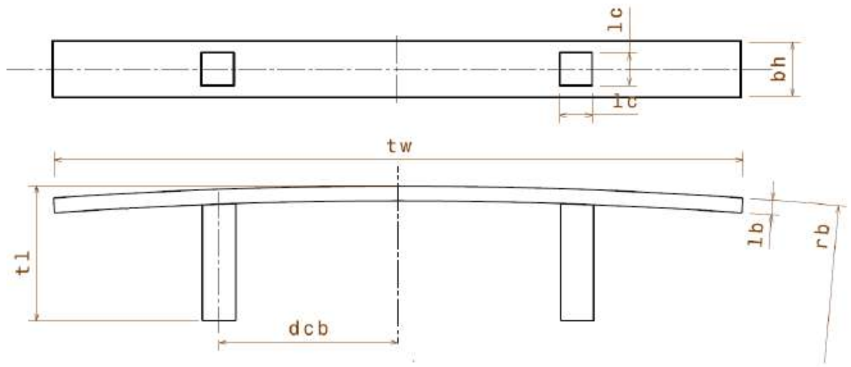

Figure 3.2: Parametrized geometry for the primary structure

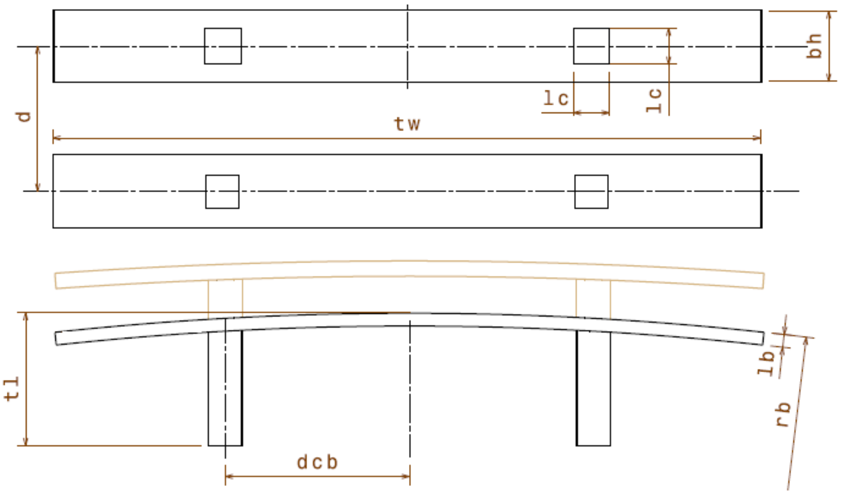

Figure 3.3: Parametrized geometry for both structures

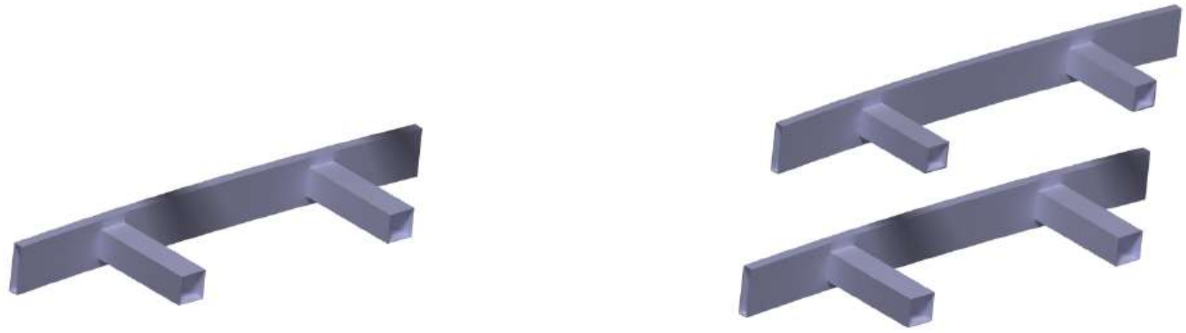

(a) Geometry for the primary structure

(b) Geometry for both structures

Figure 3.4: Isometric views for both files

Both files are parametrized in the same way. The difference is in the parametrization of the file with both parts. In this case, the parameters of the primary structure are fixed to the values obtained in the respective optimization. Only the values for the secondary structure are modified in the macro.

Both structures were designed with a 2 mm thickness with an offset of 1 mm for each side of the parameters references in order to have the mid-surfaces directly in the desired coordinates.

The geometry is updated when the script passes to the command line the $CATIA^{TM}\ V5$ executable with the macro modified previously as argument.

3.2.2 Primary Considerations

Several aspects must be in consideration before the optimization setup. To achieve reliable results, some preliminary tests must be performed in order to have the best solutions in the end of optimizations. This way, the effects in signal filtering, mesh size, heat affected zone and the possibility of optimize both structures separately will be evaluated.

Filtering

Due to interferences in measurements of accelerations during impact against the rigid barrier, it is necessary to filter the data before analysis. The recordings of the experimental tests are regulated by the *Full Width Frontal Test Protocol by Euro NCAP* [19]. Moreover, data acquisition, instrumentation and filtering have to be in accordance with the regulation *SAE J211: Instrumentation for Impact Test - Part 1 - Electronic Instrumentation* [55]. The acceleration measurement in this project for structure optimization is based on Head Injury Criteria (HIC) and maximum accelerations suffered by head. The guidelines for this type of recording acquisition are to use the CFC (Channel Frequency Class) 1000. Figure 3.5 traduces the difference between the filtered and original curve. Due to the vibration in the frontal part of the bumper that amplifies the vibrations caused by the folding on crash boxes and another interferences, there are high frequency oscillations that have to be filtered.

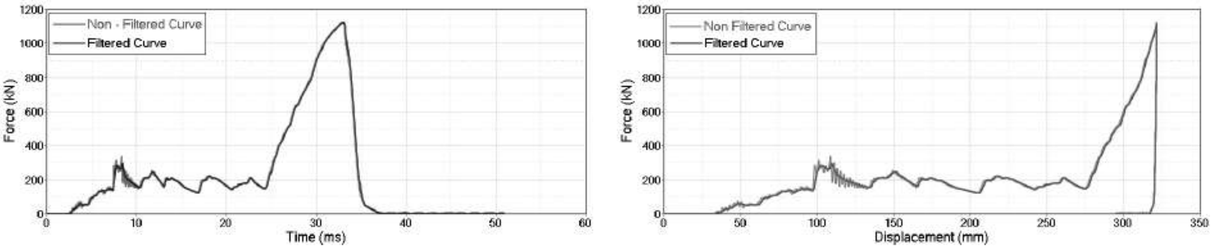

(a) Time Force Filtered vs Non Filtered curve

(b) Force Displacement Filtered vs Non Filtered curve

Figure 3.5: Filtered vs non-filtered curves

Mesh Convergence

In an explicit simulation, the mesh size is exponentially correlated with the simulation effort. From equation (2.25), it is understandable that a reduction in the element size leads to a reduction in the time step and so the solver has to make not only more iterations but also more calculations due to the increase in elements number. In order to evaluate the effects between different time steps and mesh sizes, a single geometry was created to perform several impact tests to have a comparison basis. The mass imposed for these test was 750 kg. The parameters used are in table 3.4 respecting the description given by the table 3.3.

Table 3.4: Geometry parameters for mesh convergence test

Parameter	t	lc	tl	tw	rb	dcb	bh
Size (mm)	3	80	300	1300	3000	700	100

The results were analysed regarding simulation time, force vs displacement curve and deformation patterns. The main objective is to find a good compromise between simulation time and a mesh size able to demonstrate the right deformation in foldings and a force vs displacement curve similar with those of more refined meshes.

Figure 3.6 was obtained after the tests to have a perception of the simulation time vs mesh size being achieved an exponential relation between these two aspects. With a small reduction in the element size, the computational time shows a large increase. For example, between a mesh with 6 mm and 7 mm, the computational time went from 40 to 100 minutes.

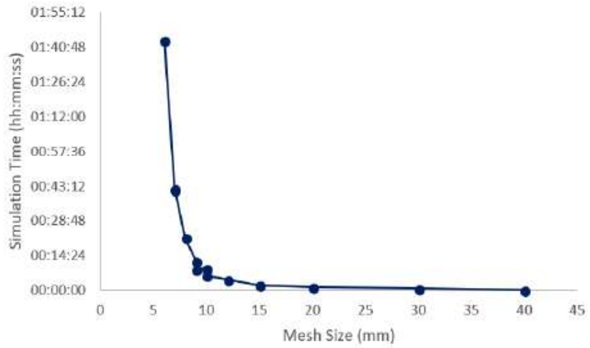

Figure 3.6: Simulation time vs mesh size.

The simulation time was evaluated comparing different time steps (TS) and nodal time steps (TN). The nodal time step is a control present in RADIOSS that sets the minimum time step that the solver needs to compute the simulation. If the time step has to be less than this value, the solver adds mass to the nodes to control the damping, resulting in a lower frequency.

The force-displacement graphic for each mesh size is shown in figure 3.7.

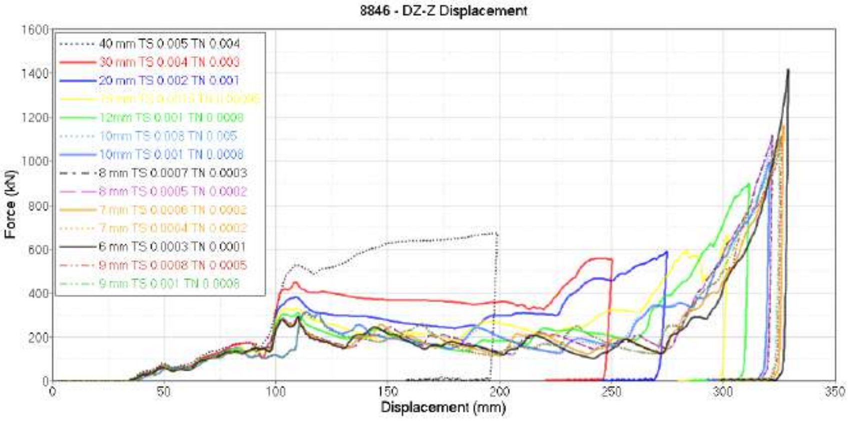

Figure 3.7: Force-displacement curves for each mesh size

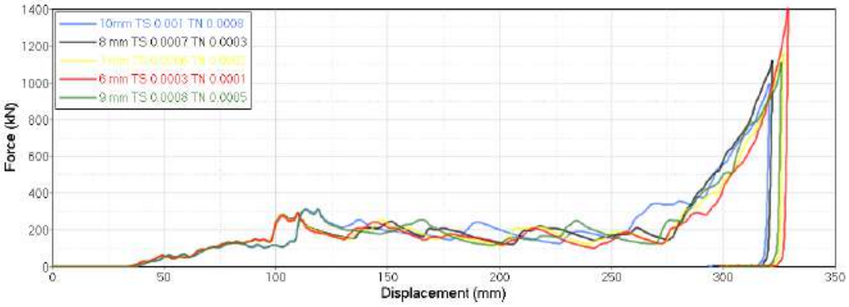

Figure 3.8: Force-displacement curves for the most refined meshes

Analysing figure 3.8, it is concluded that the best compromise between the results and the computational time is the 8 mm mesh. Moreover, to evaluate the deformation pattern between the most refined mesh and the 8 mm mesh it is necessary compare the different folds for each size wich is shown in figure 3.9.

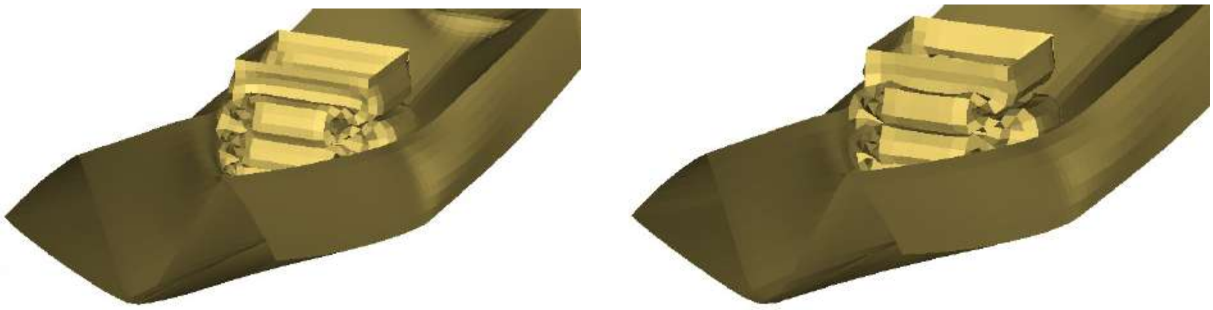

(a) 6mm meshed structure

(b) 8mm meshed structure

Figure 3.9: Comparison between the deformed structure with different meshes

It can be seen that the deformation pattern is not affected with the coarser mesh. Thus, it is expectable that the final results with a $8mm$ mesh are close to a $6mm$ mesh. Finally, the relative difference between the energy absorption (EA) between the these two meshes was

$$Difference = \frac{EA_{8_{mm}} - EA_{6_{mm}}}{EA_{6_{mm}}} = \frac{65757.3 - 65269.2}{65269.2} = 0.007478 = 0.7478\%, \tag{3.1}$$

which is found to be negligible. Concluding, the 8mm mesh revealed the best compromise between reliable results and computation time.

HAZ Comparison

The weld zones were evaluated regarding heat effects in order to percept the effect on the overall performance of the structure. Kokkula et al. [56] included this effect in numerical simulations, showing a peak force reduction. This way, a FEA was made to understand the heat influence in these type of strucutres.

Thus, the elements in the junction between the crash box and the bumper were selected to define the HAZ properties. The figure 3.10 shows the selected elements. The thickness was defined as constant and the 6061 T6 material properties was assigned as in table 3.1.

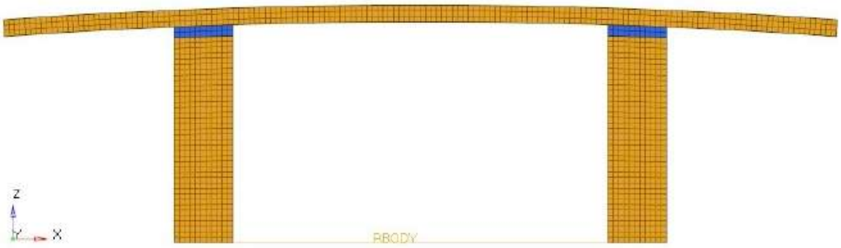

Figure 3.10: Bumper with the Heat Affected Zone (blue) and unchanged properties (yellow)

The parameters respecting table 3.3 used to design the geometry in figure 3.10 are summarized in table 3.5.

Table 3.5: Geometry parameters for HAZ comparison

Parameter	t	lc	tl	tw	rb	dcb
Size (mm)	3.5	90	250	1250	9000	650

To compare the structures with the HAZ modelled or non modelled, it was made a crash test against a rigid wall with an imposed mass on the rigid body of 600 kg and with an initial velocity of 13.8 m/s. From the Force vs Displacement curves for both structures it was possible compare the effects. The obtained curves are in figure 3.11. The explanation of the rigid body and rigid wall is in section 3.2.4.

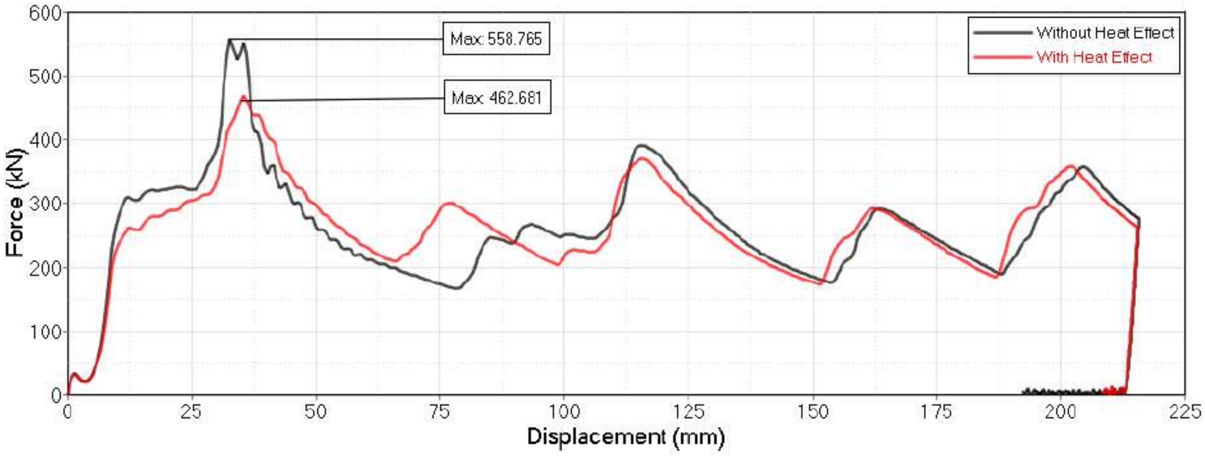

Figure 3.11: Force-displacement curve for a structure with and without HAZ effect

Thus, comparing both curves it is understandable a reduction of the maximum peak force in the structure with the HAZ modelled. This consideration implies an improvement in the global results since the CFE is dependent from the maximum peak force and the average force, i.e, as both these parameters are close from each one, the CFE value will increase. Furthermore, the SEA value is not affected because the mass is equal on both structures.

The reduction of the maximum peak force is mainly due to the yield stress reduction in the HAZ, causing the structure to deform in this area with a lower applied force.

Concluding, the HAZ revealed a significant impact in the final results, making its modelling to be taken into account.

3.2.3 Geometry Setup

To find the best way to analyse the structures, a study was carried out to understand the advantages or disadvantages between a computation with both structures or separately.

One of the benefits to compute the structures separately is saved time. In this approach, first the primary geometry is studied to obtain the force vs displacement curve of this optimal structure. Then, the secondary structure is analysed based on the primary, i. e. both graphs are added together to obtain the force vs displacement curve of the overall system. The NCAP restrictions are verified in the final curve considering the effect of both structures.

The following analysis focuses on the relativization of results and the feasibility of this hypothesis. Figure 3.12 shows the tests made to percept both approaches. In the first one, a 900 kg mass was added to the rigid body and in the second one, a 600 kg mass was added to the primary structure and a 300 kg mass is added to the secondary. In both tests, the initial velocity was 13.8 m/s.

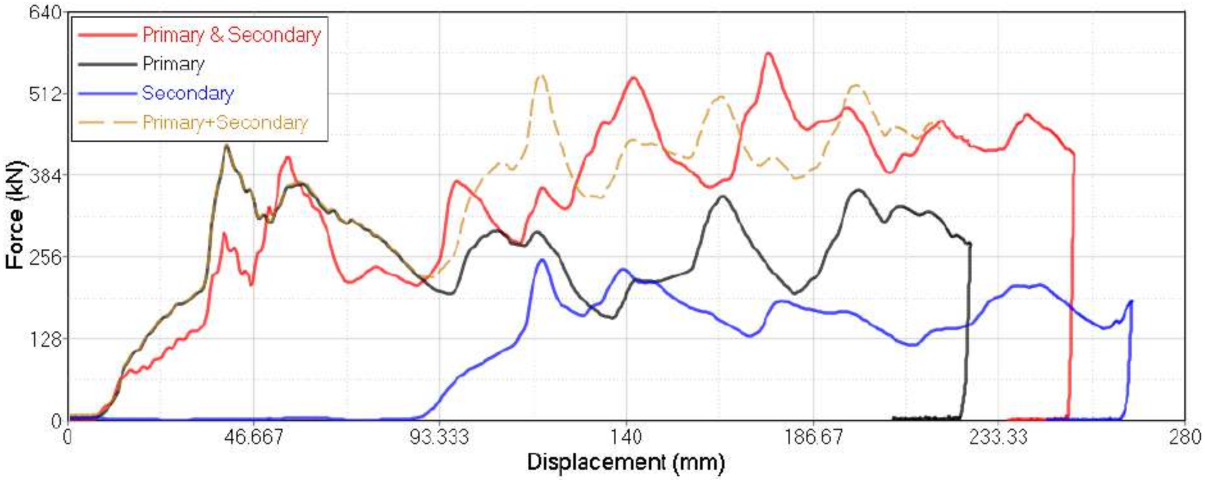

Figure 3.12: Comparison between different approaches to analyse the structures

By the analysis of the curves, it can be verified that there is a gap between the curve obtained in the simulation with both structures and in the curve corresponding to the sum of the primary and secondary curves. Despite the area under each graph is approximately equal, the shape of the curve, which is the most important factor in this type of study, is different.

Besides that, there is the problem of the maximum deformation of the two structures being different when there is a weight differentiation in the case of the separate study. The primary structure being sized for an impact with 600 kg in the rigid body, will deform until it reaches the correspondent energy. Additionally, the same will happen with the secondary structure when absorbing the 300 kg.

In the joint study, it is obvious that the energy that will be distributed by both structures will be different from the $600kg/300kg$ ratio. Furthermore, in the test with both structures, the deformation stops at the same time being equal in both structures in the end of the test. In the separate study this is impossible to simulate. Concluding, the hypothesis of making separate tests are not feasible.

To prove the results in a common simulation for both structures, figure 3.13 shows the graphic exported by this calculation. Analysing the figure, it can be seen that the problems of the sum of the curves and the limitation of the displacements are overcome. Besides this approach requires a longer simulation time due to the increase in the number of elements to be analysed, it has proved to be the most effective way to have viable results.

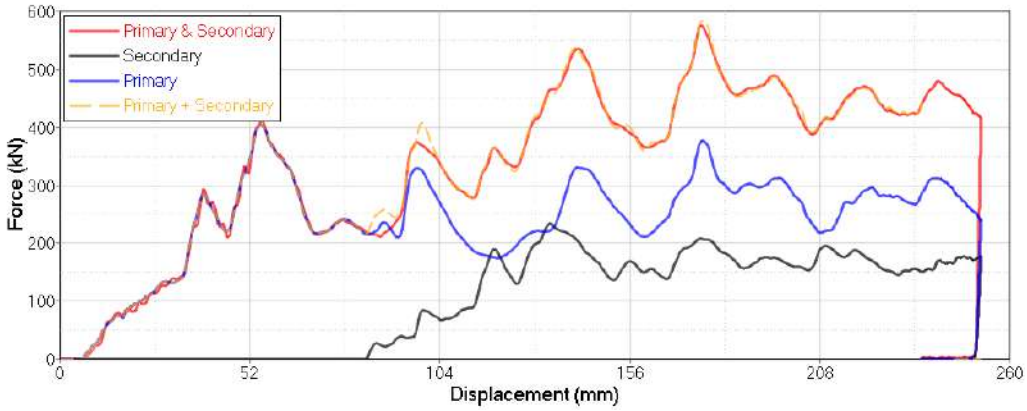

Figure 3.13: Results from a simulation with both primary and secondary structures

The figure 3.14 shows the deformation results for each type of test.

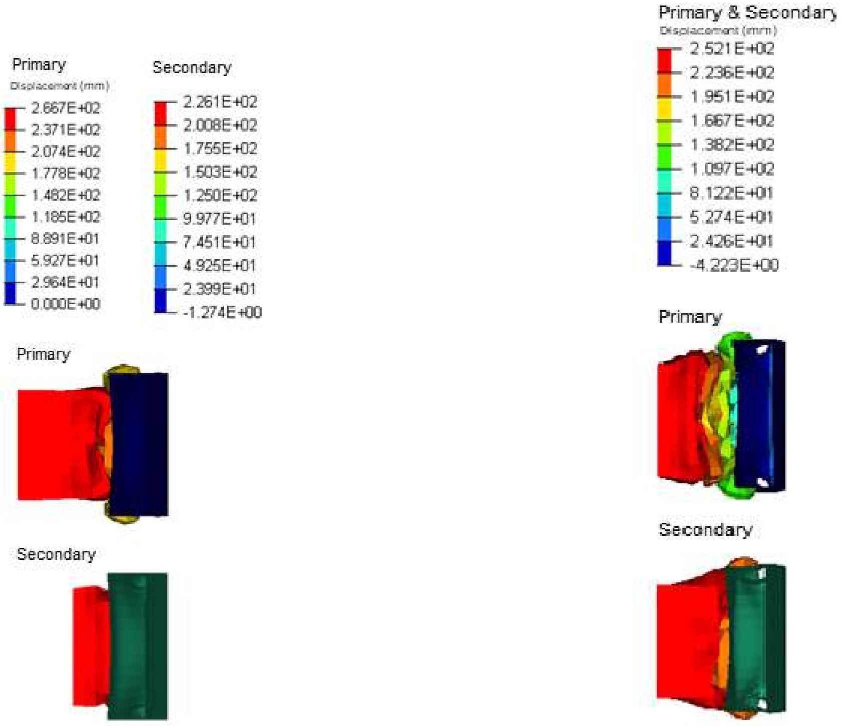
Primary
Displacement (mm)
2.667E+02
2.371E+02
2.074E+02
1.778E+02
1.482E+02
1.185E+02
8.891E+01
5.927E+01
2.964E+01
0.000E+00
Secondary
2.261E+02
2.008E+02
1.755E+02
1.503E+02
1.250E+02
9.977E+01
7.451E+01
4.925E+01
2.399E+01
-1.274E+00
Primary
Secondary
Primary & Secondary
Displacement (mm)
2.521E+02
2.236E+02
1.951E+02
1.667E+02
1.382E+02
1.097E+02
8.122E+01
5.274E+01
2.426E+01
-4.223E+00
Primary
Secondary

(a) Separated simulation

(b) Joint simulation

Figure 3.14: Comparison between the displacements in the structures for a separate or a joint simulation

As expected, the deformation patterns different between the two approaches. In the separated simulation, the secondary structure have a larger deformation than the primary, equal to the maximum displacement in its respective curve in figure 3.12. On other hand, in the joint simulation, both structures have the same displacement since the deformation stops at the same time as shown in figure 3.13.

3.2.4 Setup of Altair® HyperMesh®

$Altair$® $HyperMesh$® was used to apply the mesh, thicknesses, boundary conditions and solver specific inputs. Defining a macro in Tcl it is possible to control $HyperMesh$® automatically without user intervention. In this software, all the instructions and definition are given by the control cards that sets the specific inputs in the file to be read by the solver. This way, a process was defined to setup the crash test to fulfill the requirements.

Thus, two different macros were created: one for the primary structure optimization and another for the secondary structure optimization.

To simplify the scripting in this phase, the geometry is always designed in the same planes. The cross shapes are always drawn in the XOY plane and the geometry extruded in the positive Z direction as shown in figure 3.15.

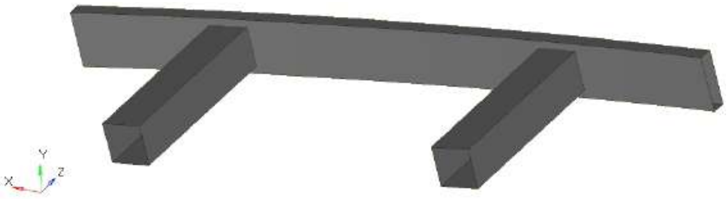

Figure 3.15: Extruded geometry in Z direction

Midsurfaces

The $HyperMesh$® process begins with the import of the geometry exported by $CATIA^{TM}$. Then, it is generated the mid-surface. This mid-surface is the base to mesh the geometry posteriorly. Figure 3.16 shows the difference between the original geometry with the respective thickness and the obtained mid-surface.

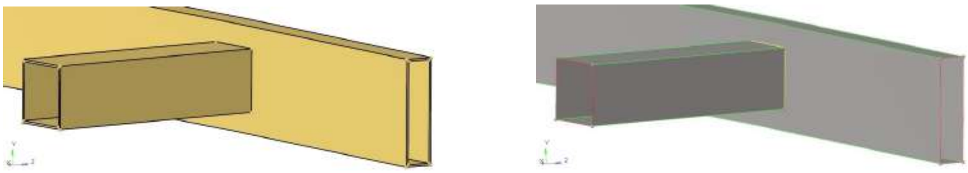

(a) Original Geometry (3D)

(b) Generated midsurfaces (2D)

Figure 3.16: Comparison between original geometry and generated midsurfaces

Components

Subsequently, the respective components are created to define properties and materials to the selected geometry. In the case of the single geometry, two components have been created to distinguish the properties between the HAZ and non-HAZ zones. In the two macro to test both geometries, four components were created. Thus, as in the macro for the single geometry, a HAZ and a non-HAZ component were created for each geometry.

Contact definition

It is necessary to define the relative displacement conditions between nodes to calculate the contact forces between the part itself and apply constraints in deformations. Therefore, the contact definition is made to prevent undesired penetrations or contacts. To define this parameter, all the components were selected as master and slave nodes. This selection defines the behaviour of the nodes and elements when they are close to each other. Thus, a contact $CARD\ TYPE\ 7$, that is a general use case, was defined revealing reliable results.

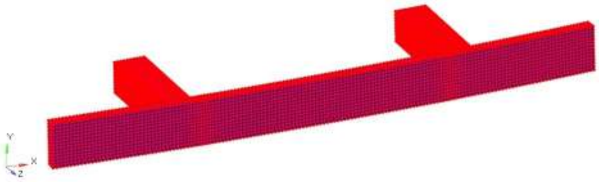

Figure 3.17: Defined contact with $CARD\ TYPE\ 7$

Rigid wall

To simulate the wall of the NCAP test, a rigid wall was defined. Firstly, a node was created to define the position of the rigid wall. This node was generated before the meshing process to associate it the ID 1. This way, it is easy to select it in the Tcl script. To prevent additional time in simulation due to the distance between the front structure and the rigid wall, the coordinates of this node are changed on the Tcl script by the $MATLAB$ script externally. Defining the base node close to the structure saves computational time since the phase where there is no contact between the wall and the structure is not relevant for this project.

The rigid wall was defined in the XOY plane with normal direction on positive Z vector to be parallel with the cross shapes plane. Figure 3.18 exemplifies the setup geometry with the rigid walls defined. This control card has as mandatory inputs the master and slave nodes to define the type of contact between the structure and the wall. In this case, the geometry was defined as slave and the wall as master.

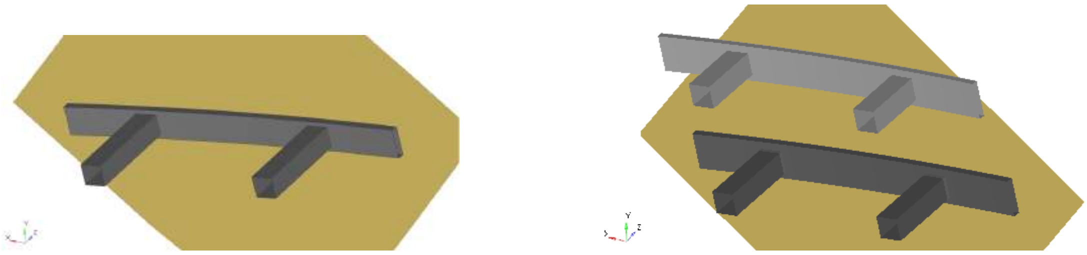

(a) Primary structure and rigid wall

(b) Primary and secondary structure and rigid wall

Figure 3.18: Structures and rigid wall

Properties

In the properties definition of the structure, a card $SHELL$ was chosen to instruct the solver to assume only 2D elements. This type of elements were chosen because the geometries will be constituted only by thin walled structures in which the thickness value is always much smaller than the other two dimensions. Thus, this approximation will simplify the computation process and save time in calculations. In the card definition is set the thickness of the elements associated to the defined property. For the optimization procedure, a property for each structure was created to define different thicknesses separately.

Material definition

The definition of the material is done through the card *M2 PLAS JOHN ZERIL* corresponding to Johnson Cook's law, explained in section 2.5.

Two materials were created in the case of the macro for one geometry and four in the case for two geometries. It was necessary to create two additional materials to give the different yield stress and ultimate tensile strength in the HAZ and non HAZ zones. Figure 3.19 exemplify the four material cards created.

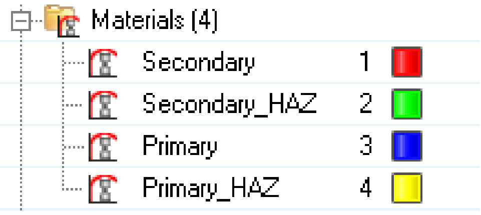

Materials (4)

Secondary	1	🟥
Secondary_HAZ	2	🟩
Primary	3	🟦
Primary_HAZ	4	🟨

Figure 3.19: Created materials

On the other hand, the $RADIOSS^{TM}$ has the option of a simplified input in which it is possible to provide only the yield strength ($SIGMA\_Y$), the ultimate tensile strength (UTS) and the strain elongation at break (E_UTS). This way, the coefficients a, b and n are computed by the program before the simulation.

The failure prediction was not formulated in this project due to the large size of elements used to analyse the structures. In $RADIOSS^{TM}$ formulation, when a shell element is in failure it is eliminated in order to decrease the strength in this area. Therefore, since the elements used are large, the strength reduction would be larger than the real failure.

In the end, it is predictable that the deformation pattern in the structures will be stable and reliable, preventing unexpected results and divergences in the simulations.

Meshing process

The mesh was then applied to the geometries. As stated before, only 2D elements were considered for the simplicity of the geometry, since the thickness is constant throughout the geometry, and also for the reduced computation time of these elements in comparison with the 3D elements. Using the $BatchMesher$, it is possible to define from two files - parameter and criteria files, the mesh size.

In this project it was defined a crash mesh with the $QEPH24$ formulation with 5 integration points [43]. These elements revealed reliable results, reducing the Hourglass effect. Figure 3.20 shows an example of a meshed geometry.

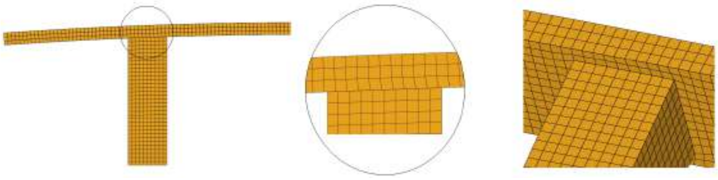

Figure 3.20: Meshed geometry

Rigid bodies and Boundary conditions

To ensure that the imposed boundary conditions are uniform in the crash boxes section, a rigid body was created to transmit these conditions uniformly. The rigid bodies are an existing property in the software that allow to apply the boundary conditions simultaneously to different nodes. The nodes defined as slave will have the same conditions as the master node.

Thus, an initial velocity of 13.89 m/s corresponding to the Euro NCAP front crash test was imposed to the master node. Assuming that the vehicle is a singular mass on the back of the bumper, the respective mass was added to the master node. In figure 3.21 the rigid bodies created for this purpose are represented and the master node in the center selected in white.

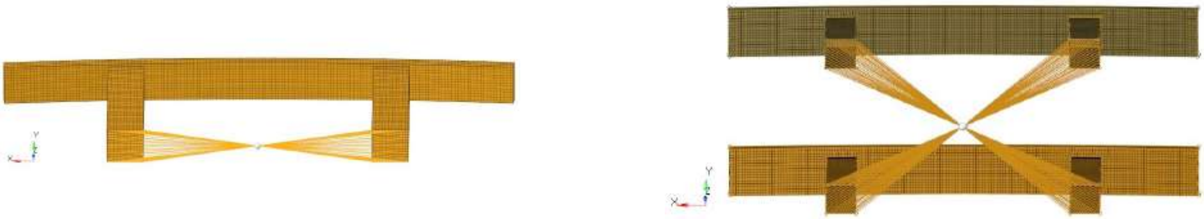

(a) Created rigid bodies for one geometry macro

(b) Created rigid bodies for two geometry macro

Figure 3.21: Generated rigid bodies

The designed geometries have the crash boxes section always in the same place, as shown in figure 3.22, so the node selection was made using a search method that finds the nodes in the XOY plane with a certain tolerance. This way, the nodes are selected and there is the possibility to calculate the master node as the cartesian average coordinate of all slave nodes.

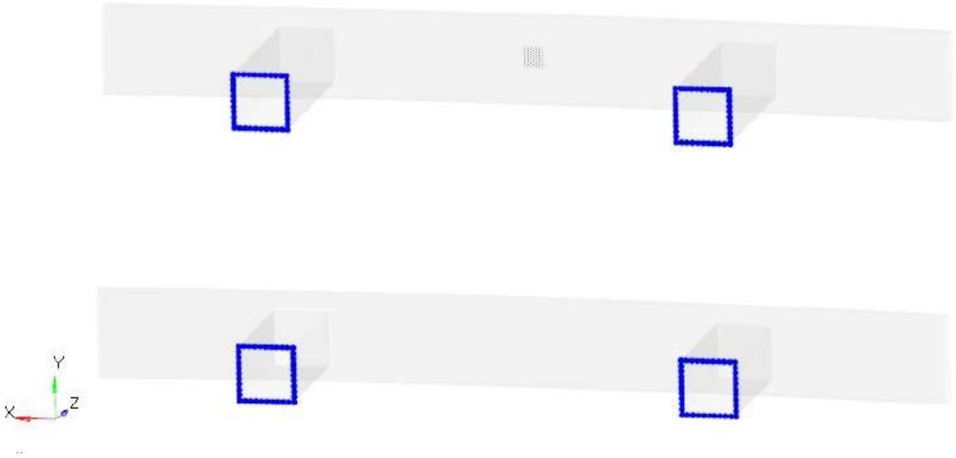

Figure 3.22: Selected nodes to rigid body creation

A boundary condition was defined to constrict the motion of the structure. This way, only the translation in the Z direction was allowed. This may be a poor approach since in a real context, the structure can deform more in one side than another due an asymmetrical impact or an asymmetrical distribution of the car's weight. In the end, it is possible that the structures are sub dimensioned for the crash test. Since the Be 2.0 is in a early stage of development, the mass distribution is not defined so it was not possible to define these mass distributions. In the current simulations, the impact is totally frontal and the centre of mass is in the middle of the crash boxes leading to a symmetrical deformation. This is only false if the mesh was not generated in a symmetric way, which is not verified.

HAZ elements selection

To select the elements between the crash boxes and the frame rail, a method had to be used through boxes. This way, two points were given to define the extremes of the box to select the elements to assign the HAZ properties. Figure 3.23 is an example of this procedure.

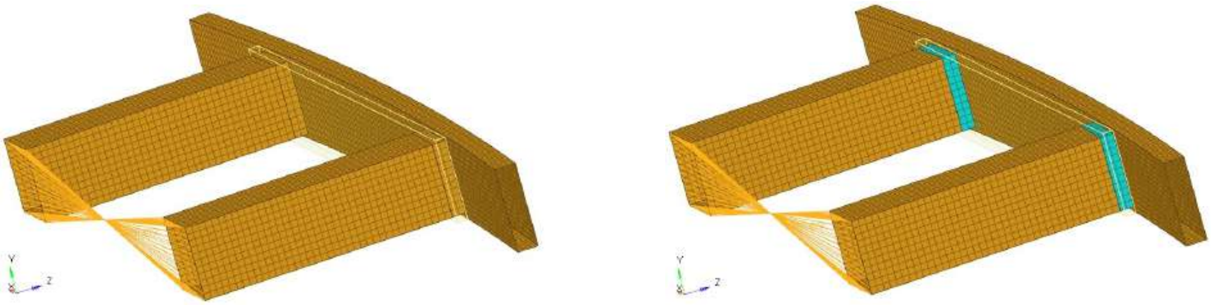

(a) Elements before selection (b) Elements after selection

Figure 3.23: Element selection for HAZ properties

By changing the Tcl script it was possible to select the desired points with a relationship between the total length of the structure, the width of the bumper and the radius.

Output blocks

To obtain the desired plots, it is necessary to define in $HyperMesh^{TM}$ which are the outputs to be exported. This way, the rigid body was defined for the measurement of the forces during the impact since this is the point that simulates the car structure and passengers. The absorbed energy is measured creating an output that exports the internal energy of the structure.

As stated in section 2.3, the SEA is calculated between the absorbed energy and the mass of the structure. Thus, it was necessary to define an output block to export the structure's mass. This output is defined for the total geometry, so in the SEA calculation it is necessary to subtract the mass from the rigid body to obtain the structure's mass.

Engine Keywords

To define the main parameters of the solver, it was necessary to define some $CONTROLCARDS$ to specify the solver parameters to run the simulation. These parameters define the time step, the outputs, and the files exported by the solver after the simulation.

Using these tools it is possible to define the writing frequency of the animation files and when the results record starts. It is also possible to define the general outputs of the simulation as forces, displacements and contact forces.

Since the time step control is fundamental to avoid results divergence, it was necessary to use the $DT/NODA$ card that defines the minimum time step for the simulation where mass is added to the nodes when it is necessary to compute with a time step lower than the assigned value for this card.

To define the maximum and initial time step, it was used the $DTIX$ card. In section 3.2.2 it is possible to understand the time steps used for each tested mesh.

The RUN card allows to define the simulation time. The computation stops when this value is reached.

Besides the defined outputs, it is necessary to create a $TFILE$ card where it is selected the frequency of the results in the output files.

3.2.5 Setup of Altair® HyperGraph®

This software aims to transform the $TFILE$ file into readable values and export the requested plots. Thus, a $session.mwv$ file was created to select which curves will be exported. It is noteworthy that the order in which the curves are selected is important. This way, figure 3.24 explains the order of the exported curves.

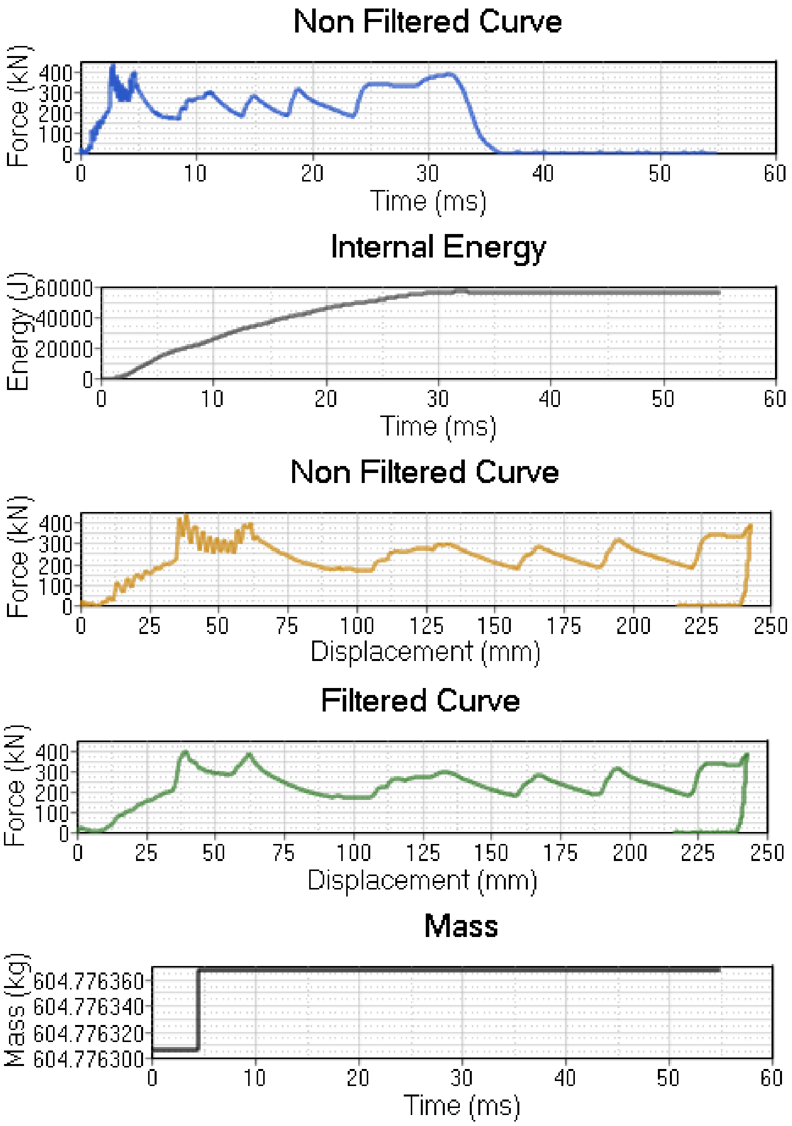

Figure 3.24: Exported curves by HyperGraph

To obtain the filtered signal, it was necessary to select the curves in temporal domain. This way, the force vs time curve was requested first and filtered and only then, using the *crossplot* tool present in $HyperGraph$®, the junction between the displacement vs time curve was made, obtaining the filtered force vs displacement curve. These force curves were obtained defining the master node of the rigid body as a measurer while the rest of the curves are obtained selecting all elements.

The $session.mwv$ is not capable of exporting the curves by itself. Therefore, it was necessary to create a macro in Tcl in which it is defined the $session.mwv$ file to be opened and the exported file type.

The selected way to read data after export was to create $.csv$ files that are supported by $MATLAB$®. Knowing the order of the curves, it was possible to calculate all values necessary to characterize the crash test and proceed to the optimization cycle.

3.2.6 MATLAB® scripting

Following the explanation about the used software to model the geometries and to apply boundary conditions, the implementation of the $MATLAB$® code that regulates all operations of these programs in sequence will be explained.

In order to execute the programs, the *dos* [47] function was used to pass the arguments to the windows command line to run the applications. The operation of this script is explained in figure 3.25.

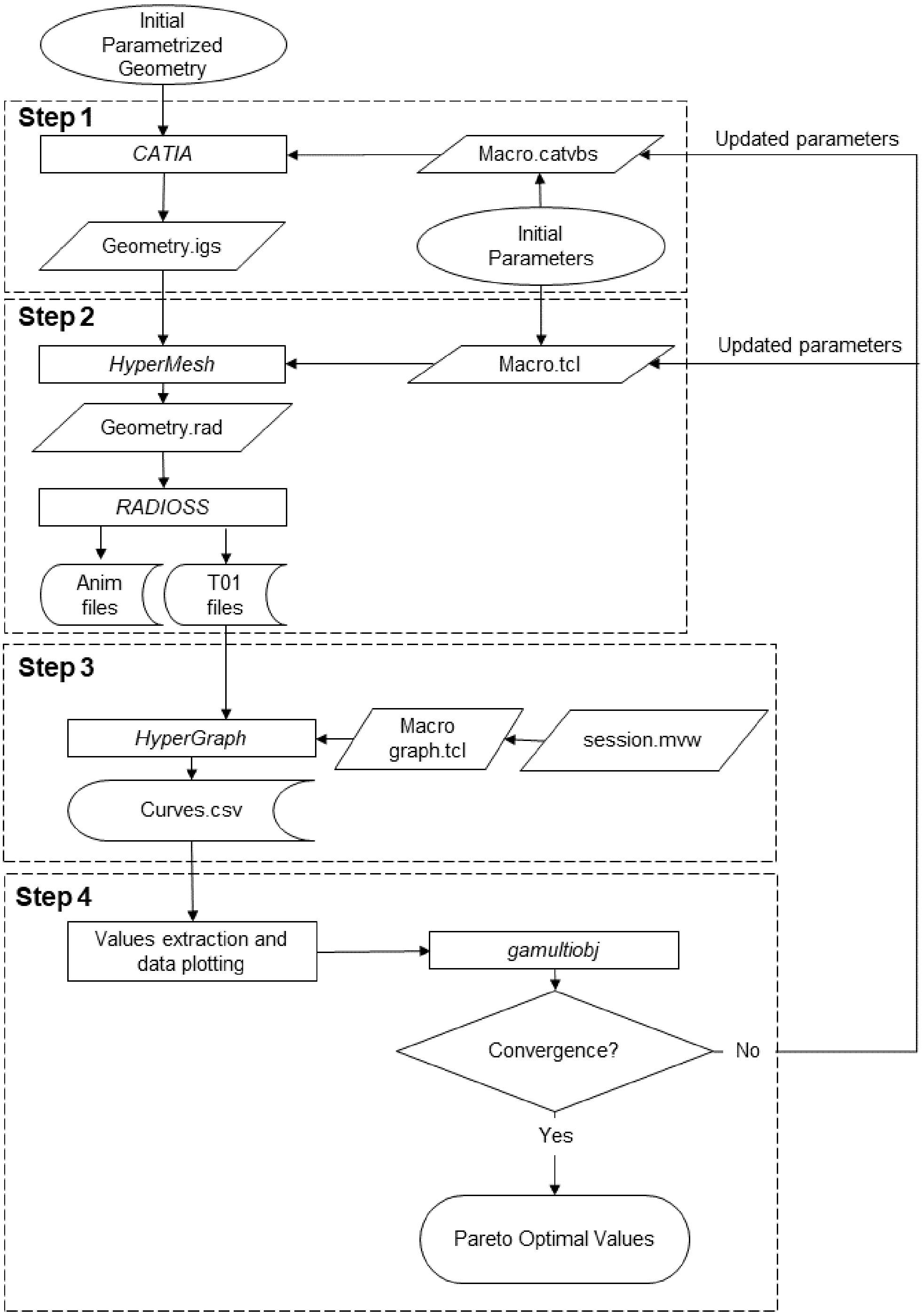
Initial Parametrized Geometry
Step 1
CATIA
Macro.catvbs
Updated parameters
Geometry.igs
Initial Parameters
Step 2
HyperMesh
Macro.tcl
Updated parameters
Geometry.rad
RADIOSS
Anim files
T01 files
Step 3
HyperGraph
Macro graph.tcl
session.mvw
Curves.csv
Step 4
Values extraction and data plotting
gamultiobj
Convergence?
No
Yes
Pareto Optimal Values

Figure 3.25: $MATLAB$ script flowchart

Step 1

Firstly, $CATIA^{TM}$ is modified depending on the parameters to be changed in the geometry. Then, the dos function runs the program in batch mode (without graphical interface) to have a faster execution. Additionally, in the $.catvbs$ macro it is expressed the export of the $.igs$ geometry that will be imported by $HyperMesh^{\circledR}$ afterwards.

Step 2

$HyperMesh^{\circledR}$ is then executed, being passed by argument the macro with the changed parameters. Thus, a *.rad* is exported and read by $RADIOSS^{\circledR}$. In this stage, the solution is computed. After the computation, the $TFILE$ and animation files are exported.

Step 3

To obtain the curves referred in section 3.2.5, the $.tcl$ macro is executed by $HyperGraph^{\circledR}$ on the command line. The export is then done in $.csv$ format and the resulting curves are then analysed by the $MATLAB^{\circledR}$ script.

Step 4

After the values calculation, they are evaluated by the $gamultiobj$ algorithm. In case of no convergence, new parameters are created, being passed to the initial macro to be read by $CATIA^{TM}$ until the convergence is achieved. In case of convergence, the Pareto is shown, representing the optimal values for the optimization. At this step, both CFE and SEA values are evaluated at each iteration to obtain the structures with better properties.

Chapter 4

Results

In this chapter the results of optimizations will be presented for the primary and secondary structure.

Applying the *gamultiobj* from *MATLAB* referred on in section 2.7.2, the optimizations were made always with the purpose to comply the Euro NCAP regulations regarding the full width impact test protocol presented in section 2.2.2.

Thus, to parametrize the geometries in a simple way, it only was considered basic shapes for the cross shapes of crash boxes and for the bumper.

4.1 Primary Structure

This section will focus on the optimization for the primary structure. Therefore, the vehicle with lower mass corresponding to the Micro Car in table 1.1 will be used as reference to design and analyse a single structure to fulfill the requisites.

According to Campos et al. [57], the percentage of energy that has to be absorbed by the front structures must be 50 % in the first half of the frontal structure in a vehicle as explained in figure 4.1. The remaining energy is absorbed in the vehicle parts beyond the frontal CMS.

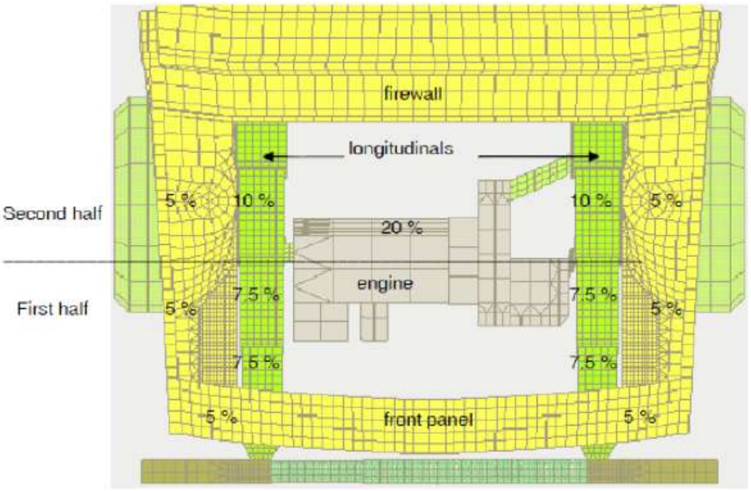

Figure 4.1: Estimated energy absorption percentages in the frontal structure (adapted from [57])

Since the Micro Car has a mass equal to 1200 kg, the value that has to be considered for the optimization process will be 600 kg to make the correspondence with the half of the kinetic energy of the vehicle. Following the Euro NCAP regulations, the initial velocity to be imposed will be 13.8 m/s as presented in table 2.2.

Thus, the energy absorbed by the structure has to be equal to the kinetic energy relative to the imposed initial conditions. The initial kinetic energy is given by

$$E_c = \frac{1}{2} \cdot M \cdot V^2 = \frac{1}{2} \cdot 600 \cdot 13.89^2 = 57879J. \tag{4.1}$$

Consequentely, after the definition of the initial conditions it was necessary to perceive the principal parameters to have into account in the optimization process. So it was necessary to evaluate the importance of several variables in the final results and ensure that the parameters to be used are those with more relevance to the final solution.

In addition, if the optimization can be done with fewer design variables, then a faster convergence, and consequently less simulations required to achieve the final results, will be obtained.

Initial considerations

As explained in section 2.4, the parameters that influence the most the energy absorption and the peak force reduction are those related with the crash box shape. Thus, the parameters non related with the dimensions of the crash boxes were evaluated to find some values that could be applied for the optimization process. The initial defined parameters are summarized in table 4.1 according with the descriptions given in table 3.3.

Table 4.1: Fixed geometry parameters for primary structure evaluation

Parameter	t	lc	tl	dcb	tw
Size (mm)	4	80	1250	650	1250

To evaluate the values that were to be fixed for rb, lb and bh, some tests were performed to find values that fit in the intended objective. The values of dcb and tw were also fixed due to project inputs.

Firstly, it was necessary to find some combinations of parameters that result in an anticipation of the peak force. Ensuring a peak in the primary structure in an earlier stage of the deformation will be translated in more room to deform the secondary structure. In an extreme case, the resultant curve will be a perfect rectangle, maximizing CFE. This is based on the assumption that the secondary structure will have its respective peak force after the one of the primary. Figure 4.2 explains the principle used to perform these tests and the desired objective. Thus, anticipating the peak force in both structures will ensure a minimization of the total deformation of the structure.

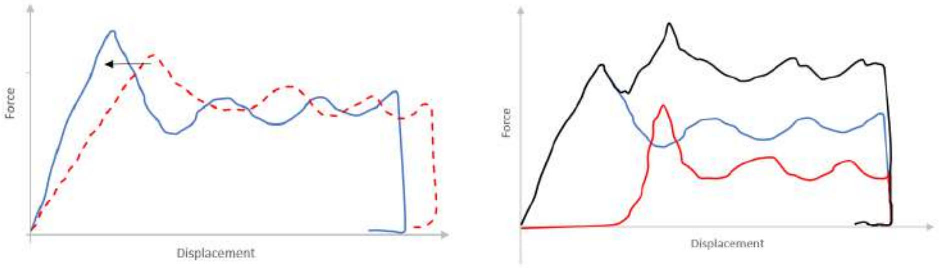

(a) Peak anticipation example (b) Primary and secondary curve sum

Figure 4.2: Curve adjustments to choose fixed parameters for optimization

Consequently, the effect of changing the values of rb, lb and bh were tested by three different simulations and the results compiled in figure 4.3.

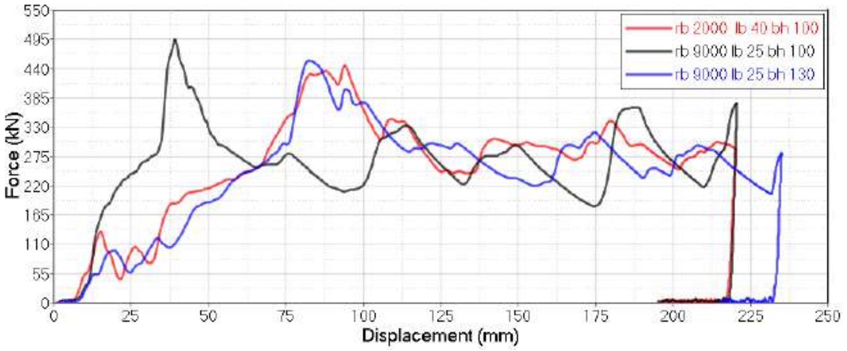

Figure 4.3: Comparison between curves with different fixed parameters

Analysing the figure it is possible to notice that the change in the value of bh does not produce significant impact in the resultant curve. However, the change in rb and lb produced exactly the desired result. With the fixed values as 9000 mm for rb and 25 mm for lb the curve has its peak almost 50 mm earlier. This happened because the peak is strongly dependent on the initial deformation of the crash boxes. With a small value of lb and a straighter bumper it is ensured that the deformation of the crash boxes begins earlier. Thus, the fixed parameters for the primary structure are in table 4.2.

Table 4.2: Fixed parameters for the primary structure

Parameter	rb	lb	bh
Size (mm)	9000	25	100

Crash box shapes

To define the best geometries to perform the optimizations of both structures, it was necessary to decide which are the most suitable shapes to design.

Even though several authors studied complex shapes and reinforcements as explained in section 2.4, it was decided to use only simple shapes to prevent errors in meshing, reduce the generated elements, minimize costs and to ease the parametrization between different geometries but with reliable results.

The shapes and the parametrization for the crash boxes are represented in figure 4.4, where letter S, C and H will designate the quadrangular, circular and hexagonal shapes, respectively.

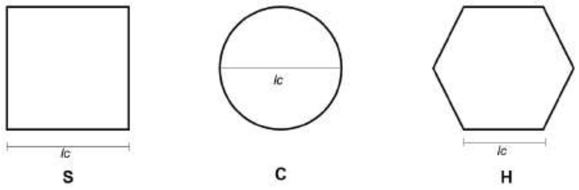

Figure 4.4: Crash box shapes for optimizations

Specific inputs for *gamultiobj*

To define the optimization problem, it was necessary to specify the inputs for the $gamultiobj$ from $MATLAB$ to obtain a good convergence and reliable results. This way, it was defined the number of generations, the population size, the number of stall generations, the function tolerance and the lower and upper bounds. The values given as input for the optimization function are summarized in table 4.3.

Table 4.3: *gamultiobj* input parameters

Parameter	**Value**
MaxGenerations	50
PopulationSize	10
MaxStallGenerations	5
FunctionTolerance	0.005
LowerBound$_{S/C}$	[2.5 60 90]
UpperBound$_{S/C}$	[5 90 350]
LowerBound$_{H}$	[2.5 25 90]
UpperBound$_{H}$	[5 55 350]

The number of generations used was defined to have a good convergence in the end. With a higher value, it is ensured that the Pareto front will have the best individuals in the end of the optimization. The population size was defined by a trade off founded between reliable results and a shorter computation time. The $MaxStallGenerations$ with the $FunctionTolerance$ are used to define the stopping criteria. If the Pareto spread is less than the value defined on $FunctionTolerance$ in the last number of $MaxStallGenerations$, the optimization stops an the final results are presented.

Addittionaly, the lower and upper bound are defined by a matrix composed by the desired parameter values to be changed in optimization. In this case, the matrix was defined by the following parameters explained in table 3.3.

$$[\boldsymbol{t} \;\; \boldsymbol{lc} \;\; \boldsymbol{tl}]$$

These values are differentiated between the hexagonal shape and the square/circular shapes because there is a different relation between lc and bh for each case.

Optimization example

One of the main disadvantages of the process described in section 3.2 is the impossibility to perform the optimizations with different cross shapes and materials at the same time varying these parameters along the computation. Thus, it was necessary to perform separate optimizations for each combination of material and cross shape, joining the results in a final Pareto.

Thus, during the optimization, the algorithm only has in consideration the values obtained for a specific material and cross shape not having access to the global problem values.

So in the end, the optimized values have to be chosen by an external entity as described in figure 2.17 by a *High Level Information*.

For instance, during each optimization, it was possible to output several plots to indicate the evolution of the structure. Thus, the force vs displacement curves, the graph CFE vs SEA as variables being used were ploted at each simulation. Figure 4.7 is an example of the control made during an optimization of a structure with 6061 T6 aluminum and a quadrilateral cross shape.

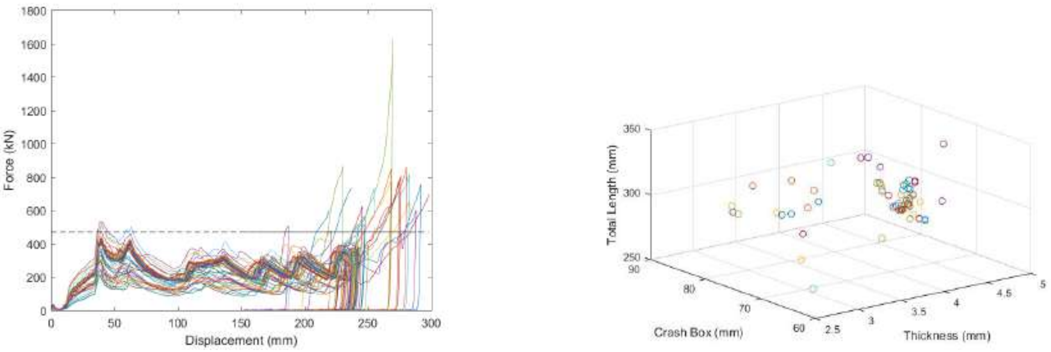

(a) Force diplacement curves for square AL6061 T6

(b) Variable combinations

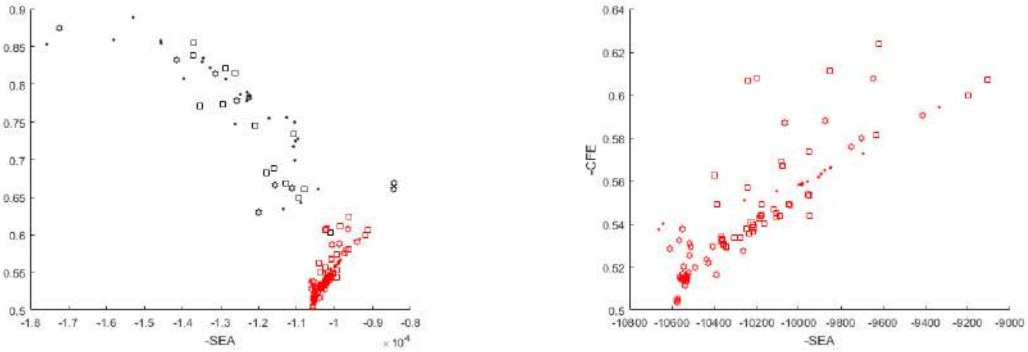

(c) Feasible and infeasible solutions for AL6061 T6 square structure

(d) Feasible solutions for AL6061 T6 square structure

Figure 4.5: Optimization ouptuts example

In figure 4.5(a) the values for the F_{max} admitted are shown in the horizontal black line. The value converted from acceleration to force was calculated by

$$F = M * a = 600 * 80 * 9.8 = 470,400N = 470.4kN. \tag{4.2}$$

This value corresponds to the Euro NCAP maximum force limit as represented in table 2.4, i.e, 80 g. The formula gives an approximation because it does not take into account the addition of the rigid body and the structure mass being calculated.

In addition, it can be viewed the convergence of the curves for a region where the energy absorption and the requirements are satisfied. Moreover, in figure 4.5(b) it is possible to perceive the convergence in the variables region given as input to the optimizer which translates in the final convergence of the solutions.

Analysing the figure 4.5(c) it is noticeable that the *infeasble* solutions have a large spread. However, the *feasible* solutions are concentrated in the lower part of the plot, corresponding to the variable convergence given in the figure 4.5(b) that satisfy the constraints.

In figure 4.5(d) it can be seen that the Pareto front does not have many solutions. This happens because the small variations in parameters are not enough to cause a greater dispersion in solutions. Due to the high computational time, the number of iterations was not enlarged. Furthermore, the obtained results meet the assumptions so it has not become strictly necessary to increase the number of simulations to find more optimal solutions.

Preliminary aspects

To find the best design for the primary structure, 12 optimizations were performed corresponding to the 3 cross shapes shown in figure 4.4 and the 4 chosen materials.

According to what was described in section 2.7.2, a maximization problem can be converted in a minimization process multiplying the objective function by -1. This way it is possible to maximize CFE and SEA giving as input for the optimization function the values of -SEA and -CFE because function $gamultiobj$ only solves minimization problems.

Additionally, the non linear constraints were defined through the Euro NCAP regulations. These conditions are evaluated by $gamultiobj$ at each calculation as

$$\begin{cases} a_{3ms} - 65 \leq 0 \\ HIC_{15} - 700 \leq 0 \ , \\ a_{max} - 80 \leq 0 \end{cases} \tag{4.3}$$

where the values are in accordance with table 2.4. The acceleration is obtained from the relation between the mass and the calculated force in simulation by the formula $a = \frac{F}{Mass \cdot g}$.

In addition, the diverged simulations were evaluated to find the effects in the final solutions. Normally, these simulations fulfil the three conditions presented in equation (4.3) but the energy absorption is not satisfied. Thus, to prevent the inclusion of these results in the final simulations, it was created a flag to signal which simulations do not reach the end of simulation time. By the total simulation time and the output frequency, it is possible to calculate the vector size of the resultant curve as $\frac{T_{total}}{f_{out}}$. If the vector does not have the size specified, the values of CFE and SEA are given by a low value to increase the rank of these simulations. This ensures that these solutions are not taken into account for the subsequent generations.

The diverged solutions normally happen in the beginning of the optimizations because the algorithm tests random combinations of variables. Thus, the structure will become soft if the thickness given by the algorithm is not enough to absorb the energy being imposed, causing a large peak in the end of the deformation. This will result in large contact forces that will make the solution diverge. Figure 4.6 illustrates a diverged simulation that was not calculated to the end. This curve was obtained with a quadrangular shape and a 6061 T4 aluminum with inputs $[2,5\ 60\ 250]\ mm$.

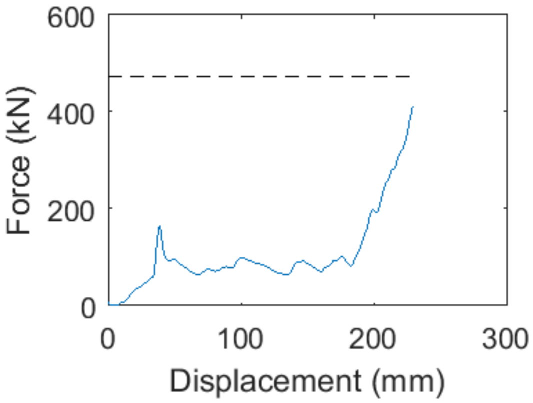

Figure 4.6: Example of diverged simulation

Additionally, the $MATLAB$ script developed computes the value of CFE based on the maximum value from the force vs displacement curve so it will consider the final value of the vector instead of the initial peak resulting in an unrealistic solution. The simulation results from the computation of the curve in figure 4.6 are in table 4.4.

Table 4.4: Diverged simulation results

CFE	SEA (J/kg)	Mass (kg)	EA (J)	F_{max} (kN)	a_{max} (g)
0.374	8476.760	2.810	23819.696	413.434	69.984

Analysing the table it is verified that the structure does not meet the presumed requirements. Despite presenting a reasonable SEA and CFE, the results should be discarded and the optimizer should search in other regions to find *feasible* solutions.

Pareto Analysis

With the previous considerations, the optimization for the primary structure was performed. To find the optimum structure to absorb the correspondent energy given by equation (4.1), several Pareto sets were analysed. The results presented in figure 4.7 represent the junction between the simulations for each crash box with the same material. The plots are organized in the configuration explained in tables 4.5 and 4.6 and, additionally, the *infeasible* solutions are represented in black.

Table 4.5: Color code for each type of material

Material	6060 T64	6061 T4	6061 T6	6082 T6
Color	red	blue	green	magenta

Table 4.6: Symbol for each type of cross shape

Cross Shape	Q	C	H
Symbol	□	●	⬡

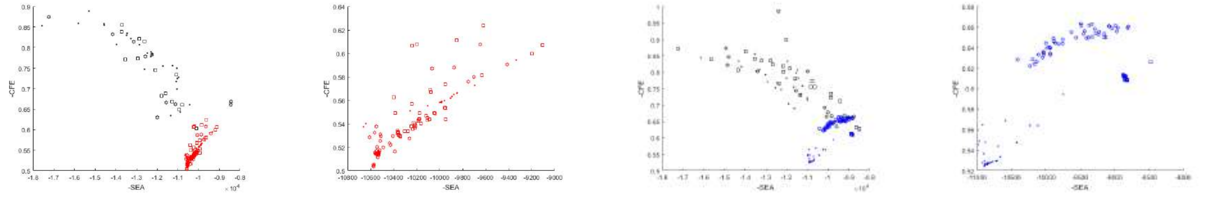

(a) Feasible and infeasible solutions for AL6060 T64 structure

(b) Feasible solutions for AL6060 T64 structure

(c) Feasible and infeasible solutions for AL6061 T4 structure

(d) Feasible solutions for AL6061 T4 structure

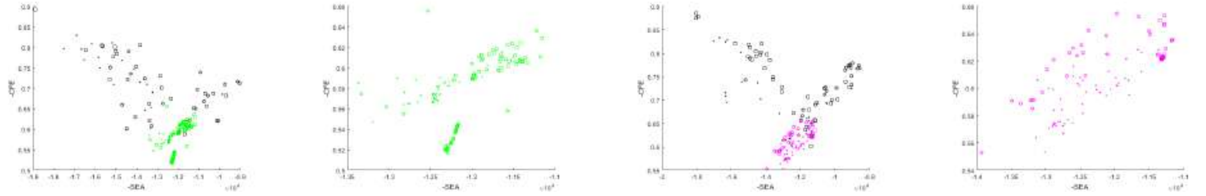

(e) Feasible and infeasible solutions for AL6061 T6 structure

(f) Feasible solutions for AL6061 T6 structure

(g) Feasible and infeasible solutions for AL6082 T6 structure

(h) Feasible solutions for AL6082 T6 structure

Figure 4.7: Individual solutions for the primary structure

By combining all values into a single Pareto, it is possible to choose some solutions to perform a posterior study to select the most suitable structure for the purpose of this project. Figure 4.8(b) shows the considered solutions.

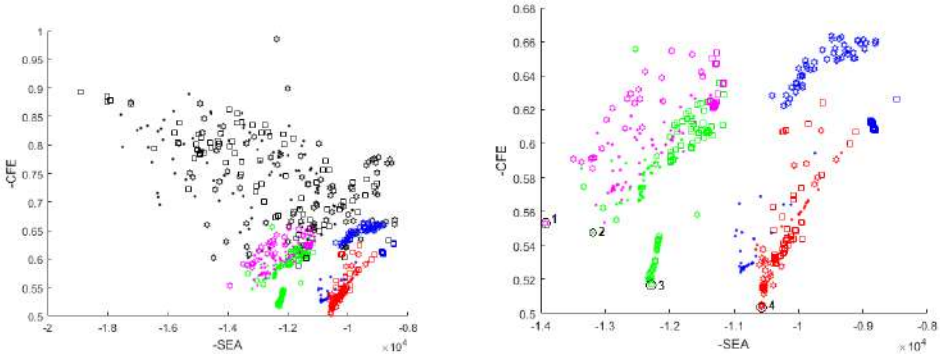

(a) Feasible and infeasible solutions

(b) Feasible solutions

Figure 4.8: Final solutions for the primary structure

As seen in figure 4.8, there are four solutions that can be chosen to make the comparison. This way, it is evident that the points in a front with a high or low declive can be selected among the other solutions as exemplified by point 3. In this region, there are 3 points that belong to Pareto front, but a small increase in SEA will be traduced in a high decrease on the CFE value. Thus, the point 3 was chosen because it reveals the best trade off in comparison with the points in the same region. Table 4.7 contains the selected points with the respective constraint values and the displacement (δ) and mass to have a greater perception on the structure characteristics.

Table 4.7: Obtained values for selected points for the primary structure

Point	**CFE**	**SEA** (J/kg)	**Mass** **(kg)**	HIC_{15}	a_{3ms} (g)	a_{max} (g)	δ **(mm)**
1	0.447	13930	4.105	220.7	53.4	61.2	261.1
2	0.452	13190	4.379	233.2	57.1	60.4	259.4
3	0.483	12286	4.664	232.8	55.9	56.4	248.6
4	0.496	10574	5.424	166.9	48.7	53.8	258.6

The value of a_{3ms} comes from the NCAP regulations in which is calculated the mean acceleration in intervals of 3 ms during impact. The maximum value of this calculus is given to the optimizer to be used as a constraint condition as given in equation 4.3. Moreover, to select the best primary structure, it is necessary to evaluate the resultant force vs displacement curves in order to have the perception about the behaviour of the different solutions during impact. The obtained curves by the selected structures are presented in figure 4.9.

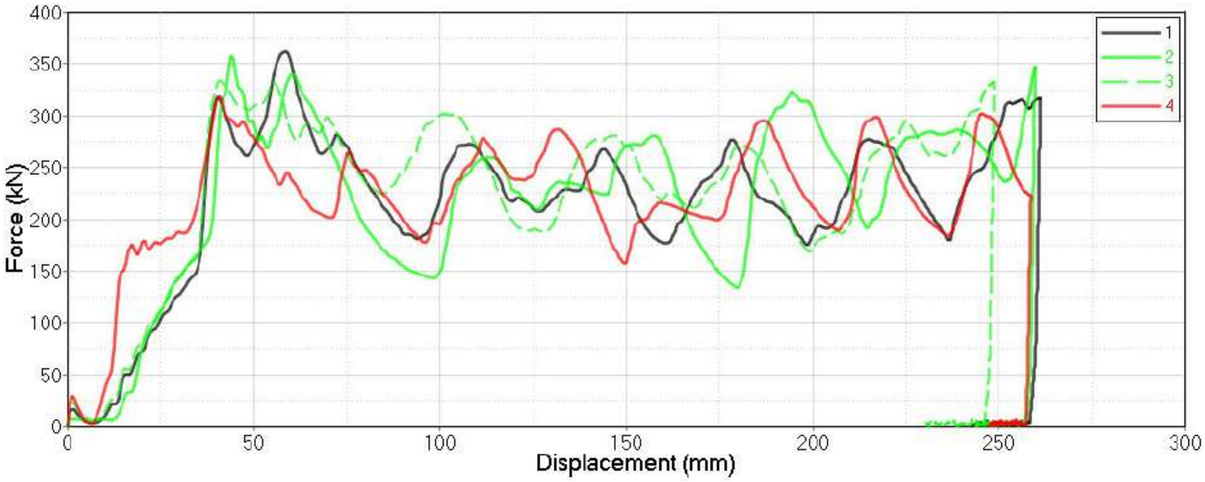

Figure 4.9: Force vs displacement curves for the selected solutions in the primary structure optimization

Analysing the figure, it can be seen that all the curves have the same pattern and the maximum displacements are almost equal. The parameters values for each structure are shown in table 4.8.

Table 4.8: Variable values for chosen points in the primary structure optimization

Point	**Cross Shape**	**Material**	***t* (mm)**	***lc* (mm)**	***tl* (mm)**
1	H	6082 T6	3.7	30.1	318.7
2	C	6161 T6	3.6	79.7	306.3
3	H	6161 T6	4.2	29.6	318.3
4	H	6060 T64	4.0	54.7	319.3

By the values obtained and subsequent information it is possible to verify that the best choice to chose as primary structure is the point 1. Besides being the structure with smaller mass, i.e, with better SEA, it has the same length as the others. On other hand, a lower thickness eliminates the risk of oversize the structure. This way, the designed structure will always deform, providing the required absorption in the imposed conditions, avoiding damage to the structures behind the bumper in case of impact with a lower speed.

Concluding, the chosen geometry and its deformed shape for the primary structure are represented in figure 4.10.

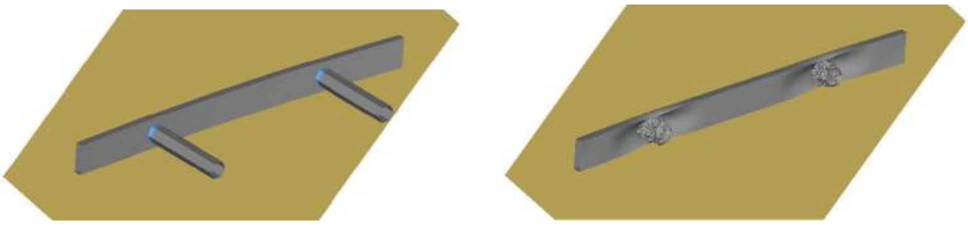

(a) Primary structure (b) Deformed primary structure

Figure 4.10: Optimized primary structure

4.2 Secondary Structure

To find the best geometry to be used as secondary structure, the optimization will be performed always in parallel with the same primary structure for every vehicle typology.

This way, table 4.9 explains the masses that will be imposed in the rigid bodies to perform the simulations. According to figure 4.1, the energy to be absorbed in the impact must be equal to 50 % of the total energy [57]. Thus, the respective masses to be added to the rigid bodies (RB) correspond to half of the total vehicle mass being analysed.

Table 4.9: Different masses applied for secondary structure optimization

Vehicle	Sports Car	Be 2.0	Big Sedan
Mass (kg)	1,400	1,600	1,800
Mass RB (kg)	700	800	900

In these cases, the optimization for the secondary structure will take into account all the variables that can be changed. Therefore, with more parameter combinations, it is possible to obtain more geometries that might fit better in the deformation pattern in parallel with the primary structure.

Thus, the only parameters set, according to table 3.3 were the dcb and tw that are defined by the inputs of the project. Moreover, the distance between both structures d was not parameterized since it was assumed that there are no movements in X and Y in the support which results in no applied moments when the primary structure is impacted. In the end, the torsion in the support plane of both geometries are negligible. This approximation can be made since it is assumed that the modeled structure in the anterior part of the CMS by the rigid body is indeformable. Therefore, the distance between both structures are not relevant because the results do not change with this parameter.

The parameters used to define the optimization of the secondary structures are summarized in table 4.10.

Table 4.10: *gamultiobj* input parameters for secondary strcture optimization

Parameter	**Values (mm)**
MaxGenerations	50
PopulationSize	15
MaxStallGenerations	5
FunctionTolerance	0.005
LowerBound$_{S/C}$	[1.5 60 150 2000 51 15]
UpperBound$_{S/C}$	[5 90 318 10000 70 40]
LowerBound$_{H}$	[1.5 25 150 2000 51 15]
UpperBound$_{H}$	[5 55 318 10000 70 40]

The lower and upper bounds are defined in a different way comparing with the parameters used in primary optimization. In this study, the parameters to be evaluated respecting the description in table 3.3 are the following:

$$[\boldsymbol{t} \;\; \boldsymbol{lc} \;\; \boldsymbol{tl} \;\; \boldsymbol{rb} \;\; \boldsymbol{bh} \;\; \boldsymbol{lb}]$$

This way, the lower and upper bounds were defined for the secondary structure optimization considering six variables. The maximum value of tl was defined as the value of the primary structure tl to ensure that the secondary structure is always shorter than the primary.

The number of population was increased from 10 to 15 due to the necessity of having more solutions in the Pareto front.

Applying the constraints defined in equation (4.3), it was possible to obtain the curves for the different structures. In the next sections it will be described the optimizations made for each type of vehicle and the optimized solutions.

The approach used to optimize the geometries was the same as that of the primary structure. To find a structure to fulfil the requisites, the three different cross shapes given in figure 4.4 and the four materials were combined and the best solutions were chosen. The optimization will be made from the lighter to the heavier vehicle.

4.2.1 Sports Car

This vehicle typology, has a mass of 1400 kg and the imposed mass in the rigid body will be 700 kg. Thus, the energy to be absorbed by the two structures is

$$Ec = \frac{1}{2} \cdot m \cdot v^2 = \frac{1}{2} \cdot 700 \cdot 13.9^2 = 67526J. \tag{4.4}$$

Therefore, the maximum force allowed in the tests is

$$F = m \cdot a = 700 \cdot 80 \cdot 9.8 = 548880N = 548.9kN. \tag{4.5}$$

With the previous considerations, the optimization for the Sports Car structure was performed. To find the optimum structure to absorb the energy given in equation (4.4), several Pareto sets were analysed. The results presented in figure 4.11 represent the junction between the simulations for each crash box with the same material.

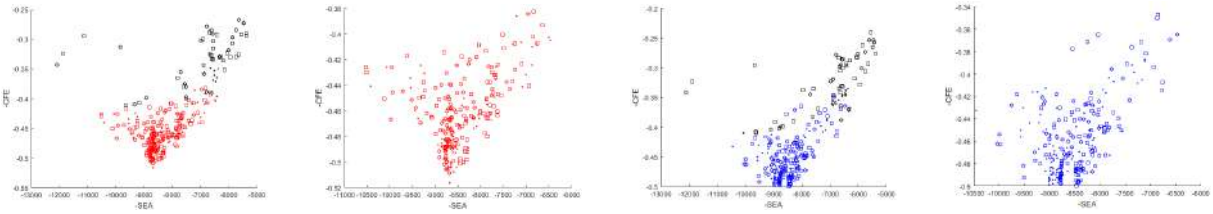

(a) Feasible and infeasible solutions for AL6060 T64 structure

(b) Feasible solutions for AL6060 T64 structure

(c) Feasible and infeasible solutions for AL6061 T4 structure

(d) Feasible solutions for AL6061 T4 structure

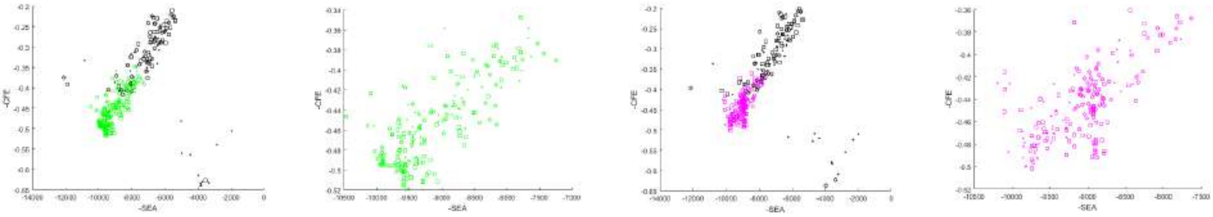

(e) Feasible and infeasible solutions for AL6061 T6 structure

(f) Feasible solutions for AL6061 T6 structure

(g) Feasible and infeasible solutions for AL6082 T6 structure

(h) Feasible solutions for AL6082 T6 structure

Figure 4.11: Individual solutions for Sports Car structure

Starting from figure 4.12(a) that shows all values combined into a single Pareto, it is possible to choose some solutions to perform a posterior study to select the most suitable structure for the purpose of this project. Figure 4.12(b) shows the considered solutions.

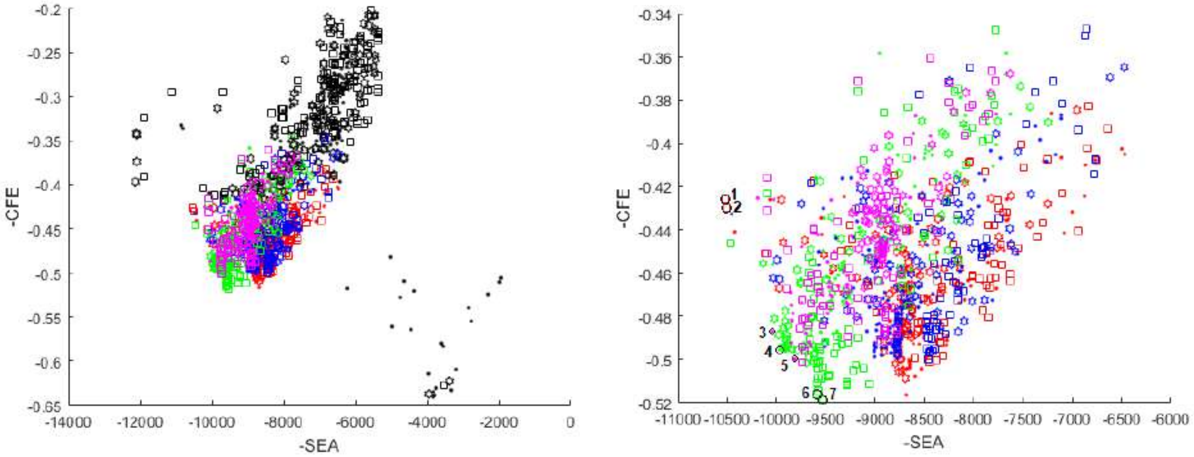

(a) Feasible and infeasible solutions

(b) Feasible solutions

Figure 4.12: Final solutions Sports Car structure

In this optimization it is possible to notice that the slope of the Pareto front is relatively high, i.e., from point 1 to 7 the value of CFE increased considerably but the value of SEA did not change in the same way. Therefore, the solutions to be compared were selected to perceive the effects of different materials and cross shapes. In table 4.11 the selected points are presented with the respective constraint values, the displacement (δ) and mass to have a greater perception of the structure characteristics.

Table 4.11: Obtained values from the Sports Car structure optimization

Point	**CFE**	**SEA** (J/kg)	**Mass** **(kg)**	HIC_{15}	a_{3ms} *(g)*	a_{max} *(g)*	δ **(mm)**
1	0.430	10511	6.357	302.5	61.4	64.0	267.6
2	0.446	10461	6.388	283.5	60.4	61.5	257.9
3	0.487	10043	6.655	252.0	55.0	56.3	247.3
4	0.495	9945	6.728	245.7	54.0	55.2	239.3
5	0.500	9820	6.810	259.2	54.4	54.8	244.4
6	0.501	9735	7.115	224.9	55.4	58.6	240.5
7	0.519	9534	7.018	229.0	50.6	52.6	242.7

Moreover, to select the best structure, it is necessary to evaluate the resultant force vs displacement curves in order to have the perception about the behavior of the different solutions during impact. The obtained curves by the solutions referenced in the table are presented in figure 4.13.

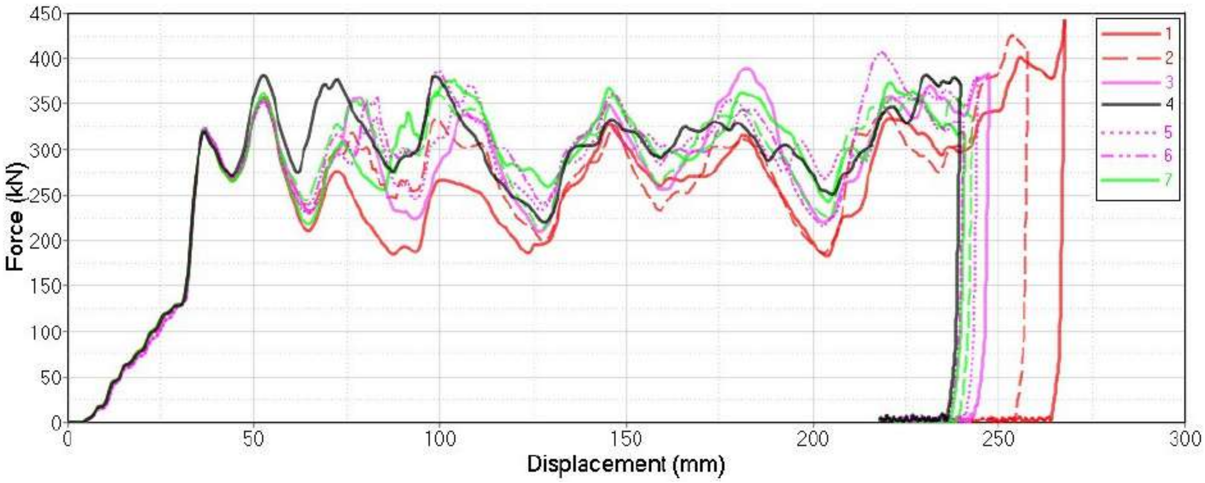

Figure 4.13: Force vs displacement curves for the selected solutions in the Sports Car structure optimization

Analysing the figure, it is possible to understand the beginning of the deformation of the secondary structures when there is a dispersion in the graphics around the 50 mm of displacement. The parameters values for each structure are shown in table 4.12.

Table 4.12: Variable values for chosen points in the Sports Car optimization

Point	**Material**	**Shape**	***t*** **(mm)**	***lc*** **(mm)**	***tl*** **(mm)**	***rb*** **(mm)**	***bh*** **(mm)**	***lb*** **(mm)**
1	6060 T64	S	1.7	64.2	221.2	2955.1	55.5	21.3
2	6060 T64	S	1.5	65.0	271.8	4813.9	57.4	22.0
3	6082 T6	C	1.7	60.4	150.5	3654.5	62.2	19.9
4	6061 T6	H	2.0	30.1	283.4	4747.1	56.2	20.6
5	6082 T6	C	1.8	66.0	268.4	4814.5	56.9	20.6
6	6082 T6	S	2.0	68.5	268.1	5684.2	57.9	21.4
7	6061 T6	S	2.0	65.5	273.3	4835.4	56.7	23.0

For this optimization, it is possible to notice the difference between some curves. Comparing curve 1 and 2 with the others it can be seen a large difference in the maximum displacement and in the shape. It is concluded by the shape of the curve one and two that the energy is absorbed in the limit because there is a peak in the end of the curve making these solutions not appropriate to be chosen.

On other hand, curves from 3 to 7 are very similar. In this optimization, structure number 4 was chosen because it has the lowest displacement and its mass are in the middle of the interval in comparison with the other solutions. The force-displacement curves for both primary and secondary structures corresponding to point 4 are presented in figure 4.14.

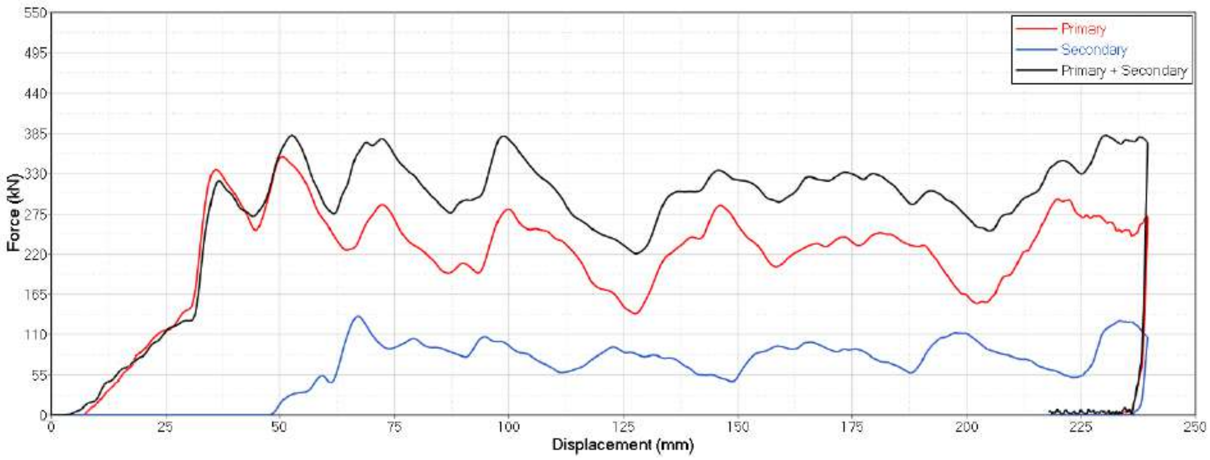

Figure 4.14: Force vs displacement curves corresponding to the selected optimal geometry for the Sports Car

Analysing figure 4.14 it can be seen that both structures deforms until the same displacement. Moreover, the maximum peak force for the overall structure is not correspondent to the sum of the maximum peaks of both primary and secondary structure.

Figure 4.24 represents the final structures with and without deformation. The crash boxes are fully deformed in the end of the crash, exhibiting the desired performance for this project.

4.2.2 Be 2.0

This vehicle typology has a mass of 1600 kg and the imposed mass in the rigid body will be 800 kg. Thus, the energy to be absorbed by the two structures is

$$Ec = \frac{1}{2} \cdot m \cdot v^2 = \frac{1}{2} \cdot 800 \cdot 13.9^2 = 77172J. \tag{4.6}$$

Therefore, the maximum force allowed in the tests is

$$F = m \cdot a = 800 \cdot 80 \cdot 9.8 = 627,200N = 627.2kN. \tag{4.7}$$

With the previous considerations the optimization for the Be 2.0 structure was performed. To find the optimum structure to absorb the correspondent energy given in equation (4.6), several Pareto sets were analysed. The results presented in figure 4.15 represent the junction between the simulations for each crash box with the same material.

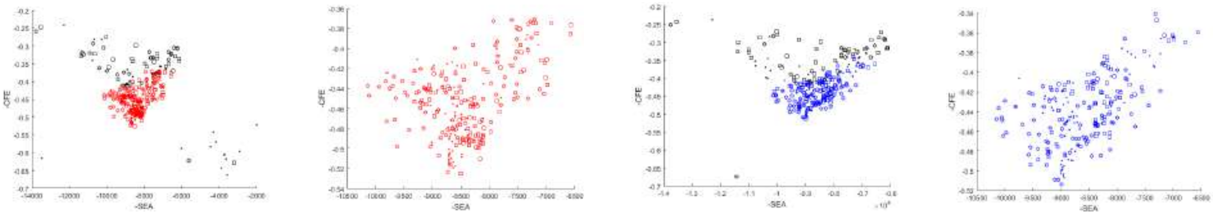

(a) Feasible and infeasible solutions for AL6060 T64 structure

(b) Feasible solutions for AL6060 T64 structure

(c) Feasible and infeasible solutions for AL6061 T4 structure

(d) Feasible solutions for AL6061 T4 structure

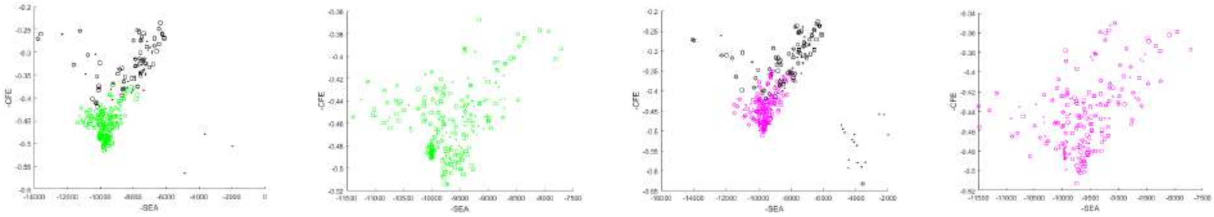

(e) Feasible and infeasible solutions for AL6061 T6 structure

(f) Feasible solutions for AL6061 T6 structure

(g) Feasible and infeasible solutions for AL6082 T6 structure

(h) Feasible solutions for AL6082 T6 structure

Figure 4.15: Individual solutions for Be 2.0 structure

Starting from figure 4.16(a) that shows all values combined into a single Pareto, it is possible to choose some solutions to perform a posterior study to select the most suitable structure for the purpose of this project. Figure 4.16 shows the considered solutions.

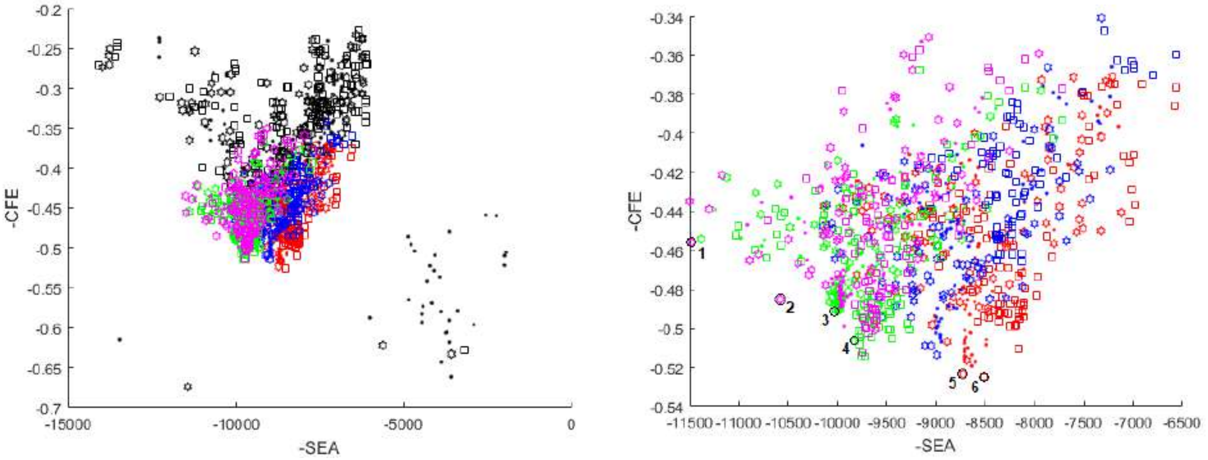

(a) Feasible and infeasible solutions

(b) Feasible solutions

Figure 4.16: Final solutions for Be 2.0 structure

The solutions presented were chosen to have different materials and cross shapes in the next evaluation. In table 4.13 the selected points are presented with the respective constraint values, the displacement (δ) and mass to have a greater perception of the structure characteristics.

Table 4.13: Obtained values from the Be 2.0 structure optimization

Point	**CFE**	**SEA**	**Mass**	HIC_{15}	a_{3ms}	a_{max}	δ
		(J/kg)	**(kg)**		*(g)*	*(g)*	**(mm)**
1	0.456	11481	6.780	311.2	59.0	60.1	263.1
2	0.485	10581	7.221	264.0	55.9	56.6	253.5
3	0.491	10020	7.630	291.9	54.9	55.9	257.2
4	0.514	9756	7.833	230.6	50.6	53.2	247.9
5	0.523	8727	8.766	241.6	51,5	52.1	252.9
6	0.525	8505	9.001	223.3	51.8	51.9	260.9

Moreover, to select the best structure, it is necessary to evaluate the resultant force vs displacement curves in order to have the perception about the behavior of the different solutions during impact. The obtained curves by the solutions referenced in the table are presented in figure 4.17.

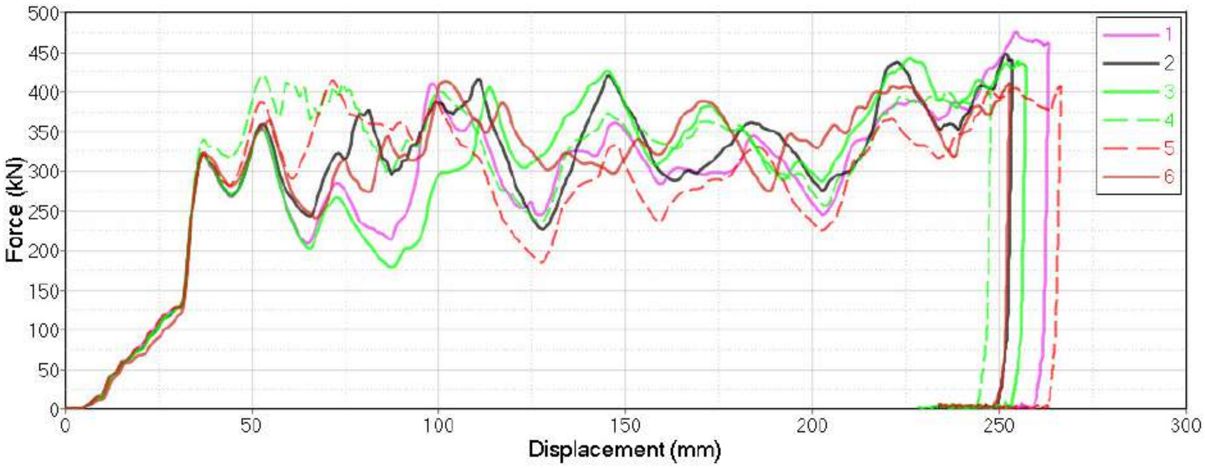

Figure 4.17: Force vs displacement curves for the selected solutions in the Be 2.0 structure optimization

The parameters values for each structure are shown in table 4.14.

Table 4.14: Variable values for chosen points in the Be 2.0 optimization

Point	**Material**	**Shape**	***t*** **(mm)**	***lc*** **(mm)**	***tl*** **(mm)**	***rb*** **(mm)**	***bh*** **(mm)**	***lb*** **(mm)**
1	6082T6	H	2.0	30.9	255.0	3796	57.0	21.9
2	6082T6	H	2.0	41.1	271.9	5608	59.5	23.0
3	6061T6	H	2.7	27.7	238.0	5849	59.4	22.0
4	6061T6	S	2.4	73.9	290.6	4970	58.8	23.9
5	6060T64	H	2.7	45.1	270.5	8431	65.7	28.0
6	6060T64	S	2.8	81.2	269.1	5969	65.8	27.5

Analysing the graphics, it is possible to notice the similarity between the curves. In this case all the curves have proven to be efficient absorbing the total energy. Therefore, the values used to select the best geometry was the maximum displacement and the mass of the structure. In these aspects, structure number 2 has a lower displacement than almost the other structures and a lower mass with exception of structure 1. Moreover, curve number 1 presented a higher peak in the end of the deformation, being a sign that the structure may not withstand a slight positive variation in the speed at impact and thus the conditions could be not respected in a more rigorous test.

Concluding, the chosen geometry was structure number 2 that is presented in figure 4.25. The force-displacement curves for both primary and secondary structures in this test are presented in figure 4.18.

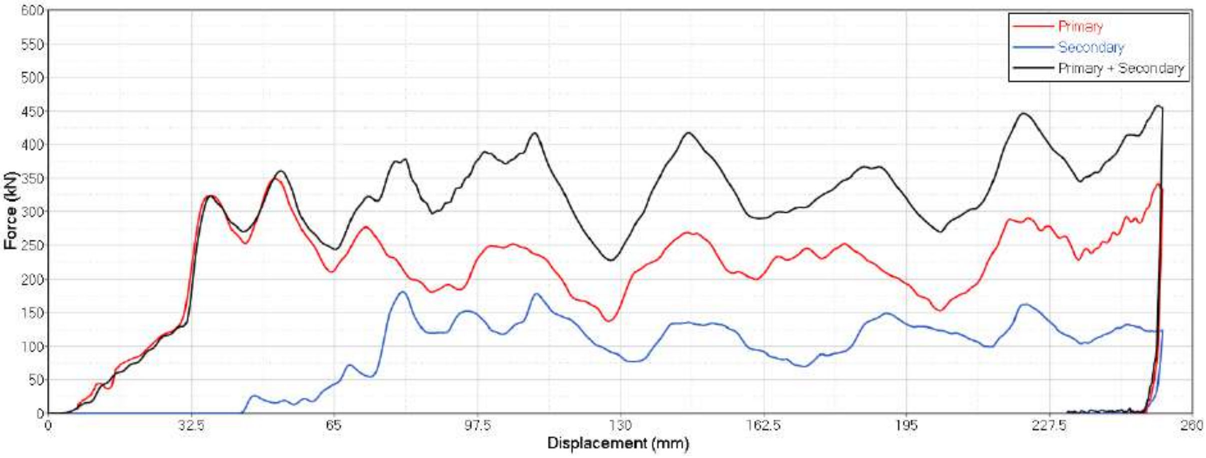

Figure 4.18: Force vs displacement curves corresponding to the selected optimal geometry for the Be 2.0 Car

4.2.3 Big Sedan

This vehicle typology has a mass of 1800 kg and the imposed mass in the rigid body will be 900 kg. Thus, the energy to be absorbed by the two structures is

$$Ec = \frac{1}{2} \cdot m \cdot v^2 = \frac{1}{2} \cdot 900 \cdot 13.9^2 = 86945J. \tag{4.8}$$

Therefore, the maximum force allowed in the tests is

$$F = m \cdot a = 900 \cdot 80 \cdot 9.8 = 705,600N = 705.6kN. \tag{4.9}$$

With the previous considerations the optimization for the Big Sedan structure were performed. To find the optimum structure to absorb the correspondent energy given in equation (4.8), several Pareto sets were analysed. The results presented in figure 4.19 represent the junction between the simulations for each crash box with the same material.

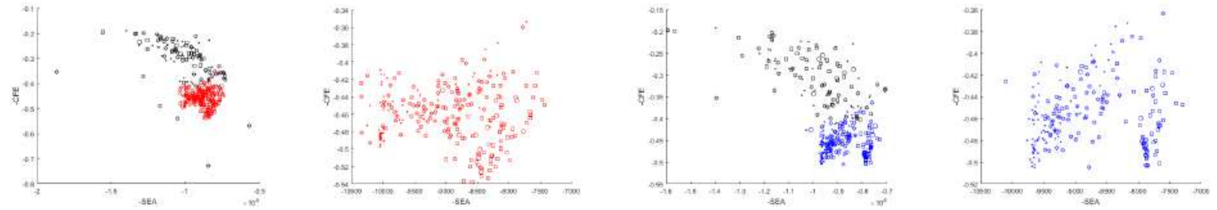

(a) Feasible and infeasible solutions for AL6060 T64 structure

(b) Feasible solutions for AL6060 T64 structure

(c) Feasible and infeasible solutions for AL6061 T4 structure

(d) Feasible solutions for AL6061 T4 structure

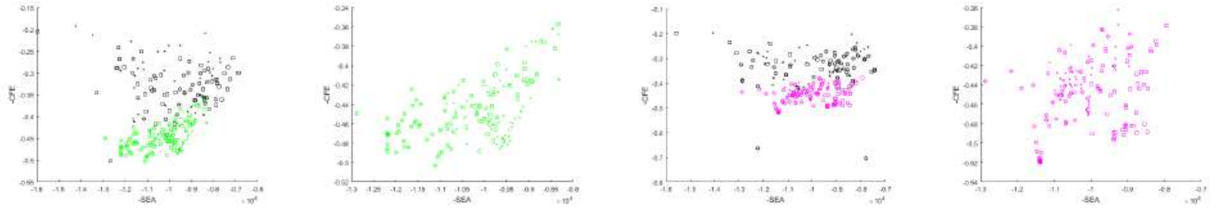

(e) Feasible and infeasible solutions for AL6061 T6 structure

(f) Feasible solutions for AL6061 T6 structure

(g) Feasible and infeasible solutions for AL6082 T6 structure

(h) Feasible solutions for AL6082 T6 structure

Figure 4.19: Individual solutions for the Big Sedan structure

Starting from figure 4.20(a) that shown all values combined into a single Pareto, it is possible to choose some solutions to perform a posterior study to select the most suitable structure for the purpose of this project. Figure 4.20(b) shows the considered solutions.

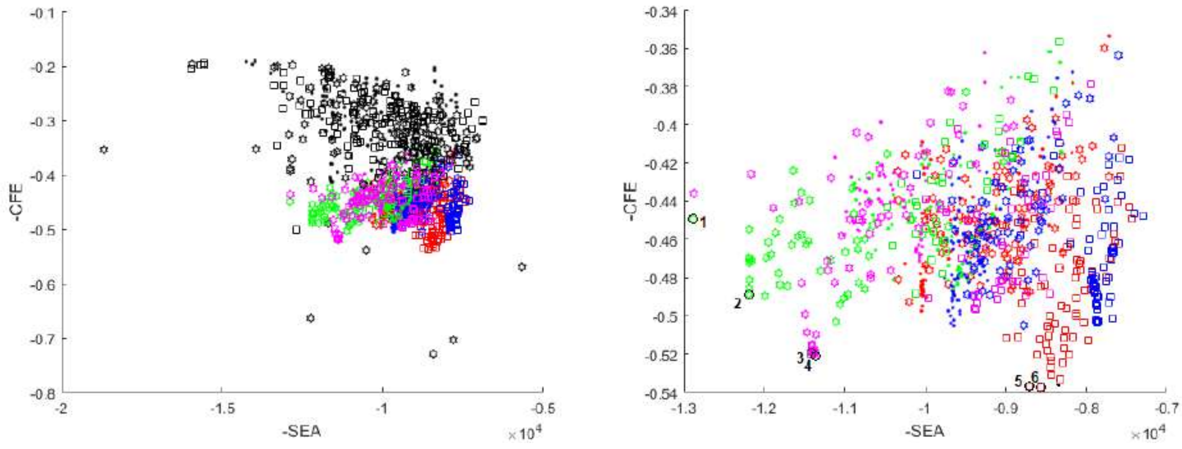

(a) Feasible and infeasible solutions

(b) Feasible solutions

Figure 4.20: Final solutions for the Big Sedan structure

The solutions presented were chosen to have different materials and cross shapes in the next evaluation. In table 4.15 the selected points are presented with the respective constraint values, the displacement (δ) and mass to have a greater perception of the structure characteristics.

Table 4.15: Obtained values from the Big Sedan structure optimization

Point	**CFE**	**SEA** $(\mathrm{J/kg})$	**Mass** **(kg)**	HIC_{15}	a_{3ms} *(g)*	a_{max} *(g)*	δ **(mm)**
1	0.449	12887	6.646	268.9	60.4	61.3	266.8
2	0.489	12190	7.039	276.5	55.1	56.0	264.6
3	0.520	11398	7.545	188.0	48.2	52.5	247.9
4	0.520	11370	7.548	188.4	48.2	52.5	247.6
5	0.537	8711	9.887	228.4	50.0	50.7	260.3
6	0.537	8574	10.041	218.2	49.5	50.8	260.0

Moreover, to select the best structure, it is necessary to evaluate the resultant force vs displacement curves in order to have the perception about the behavior of the different solutions during impact. The obtained curves by the solutions referenced in the table are presented in figure 4.21.

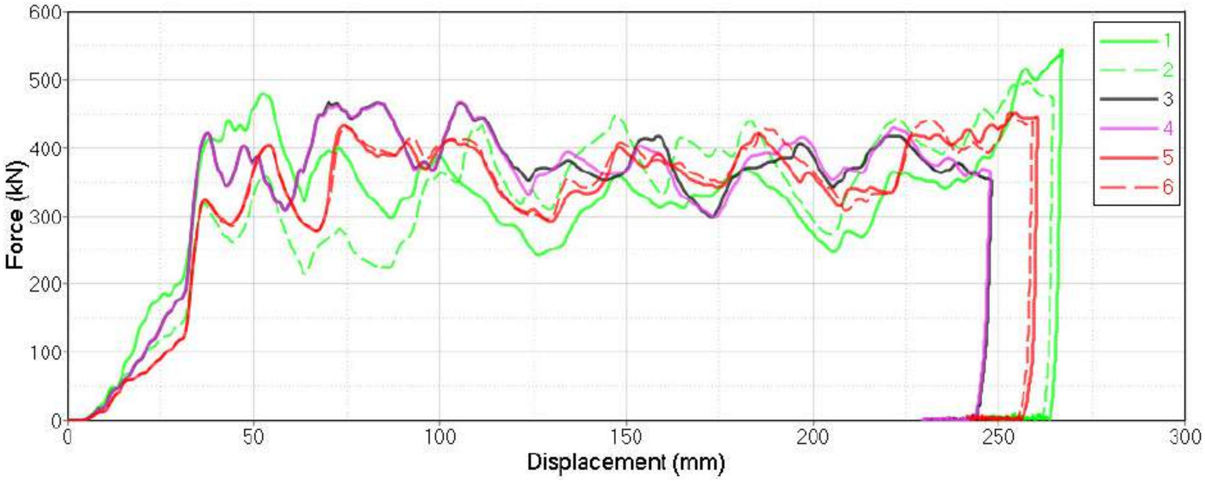

Figure 4.21: Force vs displacement curves for the selected solutions in the Big Sedan structure optimization

The parameters values for each structure are shown in table 4.16.

Table 4.16: Variable values for chosen points in the Big Sedan optimization

Point	**Material**	**Shape**	***t*** **(mm)**	***lc*** **(mm)**	***tl*** **(mm)**	***rb*** **(mm)**	***bh*** **(mm)**	***lb*** **(mm)**
1	6061 T6	H	1.8	53.7	309.2	7945	50.9	26.0
2	6061 T6	H	2.5	39.6	243.5	5137	52.0	24.5
3	6082 T6	H	2.4	43.9	304.4	4627	56.5	24.4
4	6082 T6	H	2.4	43.9	304.3	4627	56.5	24.4
5	6060 T64	S	3.9	37.3	284.7	8676	65.5	28.5
6	6060 T64	S	4.0	37.2	283.6	8435	65.8	28.5

Analysing the graphics and the tables, it is possible to perceive that structures number 3 or 4 are almost equal. Making the analysis from the Pareto for the main characteristics, it is natural that the curves are similar since they came from the same region in the solutions space and the input variables are almost equal. Even so, the graphics from structures number 1 and 2 have the peak force at the end of the deformation which implies that the structures are in the limit to withstand the impact, being not desirable their use to have an improved safety level. Additionally, structures 5 and 6 are heavier with a larger deformation, being not desirable to choose none of these structures. Consequently, the chosen structure was the number 3, and it is practically indifferent to choose the 4 as well. The geometry number 3 is represented in figure 4.26. The force-displacement curves for both primary and secondary structures in this test are presented in figure 4.22.

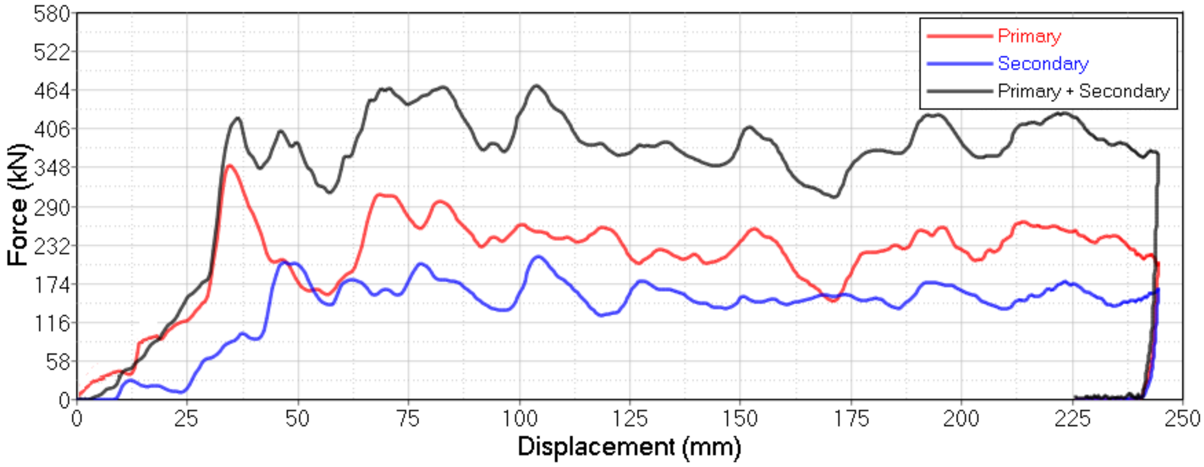

Figure 4.22: Force vs displacement curves corresponding to the selected optimal geometry for the Big Sedan

4.2.4 Final Comparisons

Finally, it is then possible to verify the efficiency of the structures obtained comparing the performance of these. Thus, analysing tables 4.17 and 4.18 it is possible to compare the energy absorption as well as the maximum peak force and the mass for each CMS. In the case of the vehicle typology with both structures the letters P, S and T represent the primary, secondary and both structures, respectively. The difference value respecting energy absorption or mass represented in table 4.18 is given by the quotient between the values of both structures for each case relative to the Sports Car.

Table 4.17: Micro Car optimized structure

Structure	F_{max} **(kN)**	a_{max} **(g)**	**EA (J)**	**Mass (kg)**
Primary	362.1	61.1	56979	4.105

Table 4.18: Sports Car, Be 2.0 and Big Sedan optimized structures

Vehicle	**Sports Car**			**Be 2.0**			**Big Sedan**		
Structure	**P**	**S**	**T**	**P**	**S**	**T**	**P**	**S**	**T**
F_{max}	352.3	134.4	381.6	348.7	180.2	457.0	351.6	212.9	555.0
a_{max}	50.9	19.4	55.1	44.1	22.8	57.8	39.5	23.9	62.4
Mass (kg)	4.105	2.623	6.728	4.105	3.116	7.221	4.105	3.440	7.545
Difference$_{Mass}$						+7.3 %			+12.1 %
EA (J)	52113	15390	67502	54604	22463	77071	52800	33808	86607
Difference$_{EA}$						+14.2 %			+28.3 %

In order to have a better perception about the behaviour of the structures, figure 4.23 was made to explicit the differences between the energy absorption and the peak force for each case.

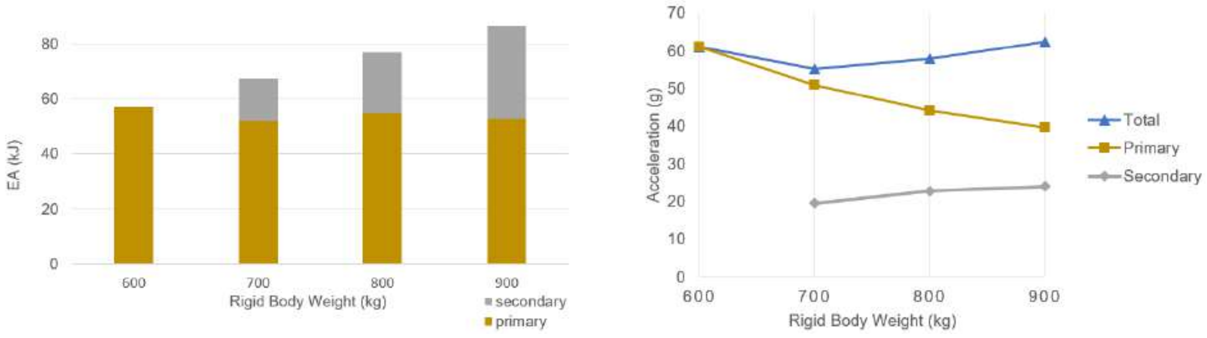

(a) Energy absorption comparison

(b) Maximum crush force comparison

Figure 4.23: Comparison between energy absorption and maximum peak force for each case

Analysing the tables and figures, it is possible to conclude that the primary structure absorbs almost the same energy in the different crash tests. This comes from the fact that the initial geometry is not oversized for the condition established in the 600 kg test. Thus, in the tests with a heavier vehicle, the structure is totally deformed, absorbing the energy that are supposed to. This phenomenon was predicted in the initial objectives, being accomplished in all optimized structures.

Moreover, the peak force is not directly related with the vehicle's mass neither with the sum of the peaks from the primary and secondary structure. As previously stated, the peak force from both structures do not occur at the same time as seen in figures 4.14, 4.18, and 4.22. However, if the objective of this project was to study a single structure to absorb the energy for each case, this parameter would be critical.

This way, the secondary structure implementation revealed a successful approach to fulfill the requisites.

Furthermore, the maximum peak for each structure must be taken into account in the next vehicle design phase. The structures that will support the crash management systems have to be strong enough to carry the maximum forces imposed in the crash tests or, in an extreme case, to begin the deformation after the entire crush of the absorbing structures.

Moreover it can be stated that with an increase of 7,3 % and 12,14 % in mass, the absorbed energy increased 14,18 % and 28,3 % making the comparison between the Be 2.0 and Big Sedan values relative to the Sports Car, respectively.

Finally, the final optimized geometries are shown in figures 4.24, 4.25 and 4.26. The structures are always designed with the darkest grey for the primary structure and the lighter for the secondary structure.

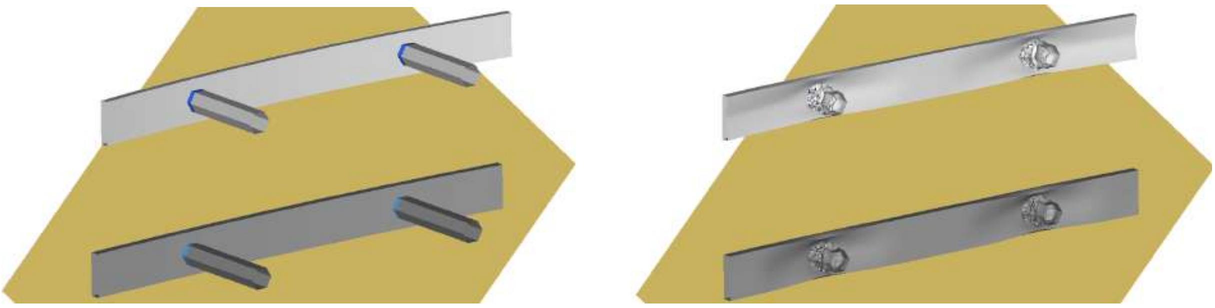

(a) Primary and secondary structures (b) Deformed primary and secondary structures

Figure 4.24: Optimized Sports Car structures

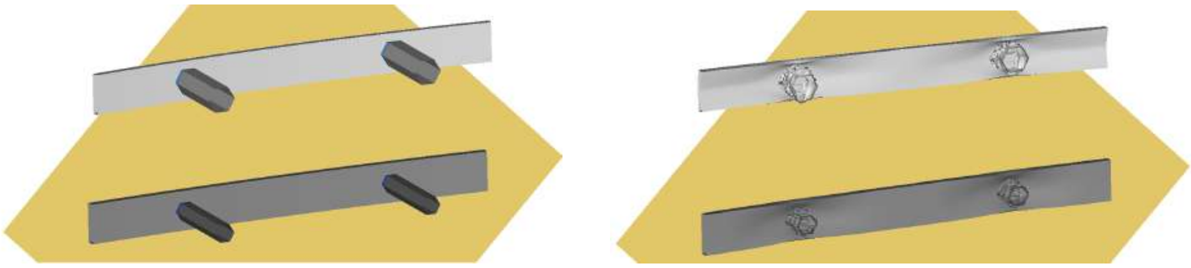

(a) Primary and secondary structures (b) Deformed primary and secondary structures

Figure 4.25: Optimized Be 2.0 structures

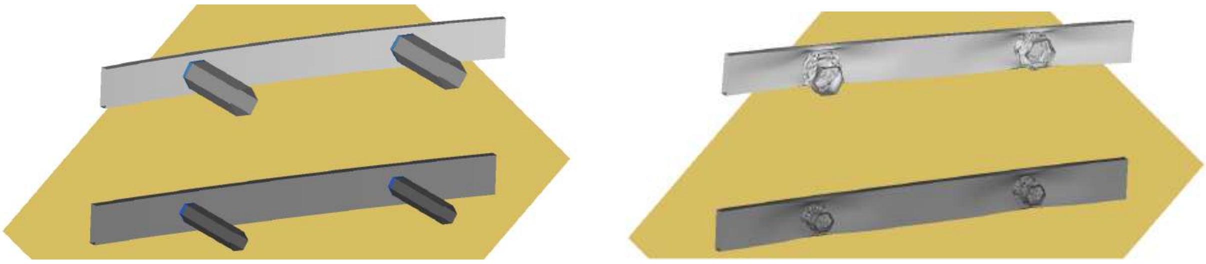

(a) Primary and secondary structures (b) Deformed primary and secondary structures

Figure 4.26: Optimized Big Sedan structures

Analysing the figures, it is noticeable the increase of robustness of the structure from the lighter to the heavier vehicle. This confirms the assumptions defined throughout the project. For the most demanding tests, it is necessary a structure with more material to absorb the additional kinetic energy that results from the impact.

Concluding, the primary and secondary structures have proven to be effective in the vehicle protection, overcoming the imposed constraints from the Euro NCAP regulations regarding full width frontal impact.

4.2.5 Computational Cost Assessment

The obtained solutions required a large computational effort. Table 4.19 shows the different simulation times that took to optimize each structure. The values presented for the simulation time are an approximation since each simulation have a different time to solve due to the difference in elements number. The nodal time step referred in section 3.2.2 was increased to 0.0004 ms in simulations with both primary and secondary structures to balance the increase in number of elements and simulation time. Thus, it was ensured faster simulations without major interferences in the final results.

Table 4.19: Simulation time for each optimization

Vehicle	**Simulation time (min.)**	**Number of simulations**	**Total time (min.)**
Mini Car	15	828	12420
Sports Car	27	1272	34344
Be 2.0	27	1295	34965
Big Sedan	27	1235	33345

Concluding, the total computational time to make the calculations was estimated in $12420 + 34344 + 34965 + 33345\ min. = 115074\ min. = 79.9\ days$ which was possible thanks to the two computers available at the time of this work.

Chapter 5

Experimental Validation Procedure

The final results and the material model must be validated to ensure the reliability of the process and the solutions. This way, a tensile test must be performed to identify the real characteristics of the material to be used and compare the material formulation with the experimental results. During the course of the project, it was not possible to acquire the material, so this chapter will serve to indicate what kind of tests and procedures have to be performed to implement the achieved solution in a real context.

5.1 Material Validation

The validation of the material [58] is performed by an uni-axial or biaxial tensile test in order to find the stress vs strain curve. In the context of this work, the best approach would be to compare the curves from the four materials. The HAZ do not need to be checked in this phase because the effects of soldering can be studied in the full test model.

Thus, according to the *ASTM B557M-15 - Standard Test Method for Tension Testing (Metric)* [58], the specimen for each material must be in accordance with the dimensions in table 5.1 referring to figure 5.1.

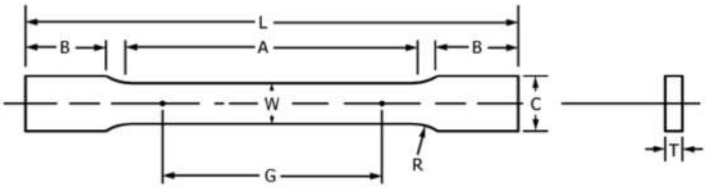

Figure 5.1: Specimen parameters for the tensile test (adapted from [58])

Table 5.1: Dimensions for the tensile test specimen (adapted from [58])

Parameter	G	W	T	R	L	A	B	C
Dimensions (mm)	50,0 ± 0,1	12,5 ± 0,2	t	12,5	200	57	50	20

The parameter T is equal to the thickness of the material portion to be analsyed.

According to Nunes [7], it is possible to test the specimens in CEiiA installations with a servo-hydraulic MTS test machine with a 50 kN load cell (SN 429175) and a biaxial extensometer model 632.85F-05.

From the tests, several curves must be obtained for each material to compute the mean curve to minimize the errors in measuring. The main results from this test will be the Young's modulus, yield strength, Poisson's ratio and elongation at break, making possible the comparison between the theoretical prediction from the FE models and the real material.

5.2 Quasi-static Approximation

It was studied the possibility to perform a dynamic test with the setup presented in FEM analysis. These tests would require an additional effort to acquire the material and large facilities to perform the crashes. Moreover, in a high velocity impact it is very difficult to capture all the frequencies during the test, so the sensors must be capable of record these data within a very high frequency.

Although, there is the option to use the servo-hydraulic MTS test machine with a 250 kN load cell (SN 10317357) present in CEiiA to validate the deformation pattern in the primary optimized structure. This way, it is necessary to verify if the quasi-static test have the same resultant characteristics as the dynamic. For this purpose, three tests are made to find out the similarities between the two type of approaches. Thus, two quasi-static tests are computed to compare with the dynamic test. The resultant curves from the simulations are in figure 5.2. It is impossible to simulate a real quasi static test with an imposed velocity in the range of mm/min due to the simulation time required to perform these tests. Consequently, the curves obtained have to be computed with a larger velocity in order to achieve results in a feasible time.

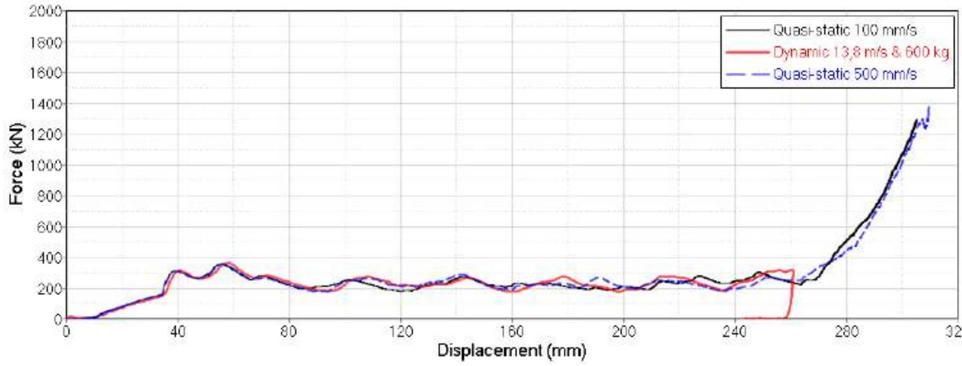

Figure 5.2: Force vs displacement curves for dynamic and quasi-static comparison

To compare the curves, only the values until the final displacement from the dynamic test have to be into account. The further values do not have significant relevance since they are leading to a greater force due to the imposed displacement that the structure are not capable to absorb. Thus, the curves are trimmed, and the values for comparison are in figure 5.3 and table 5.2.

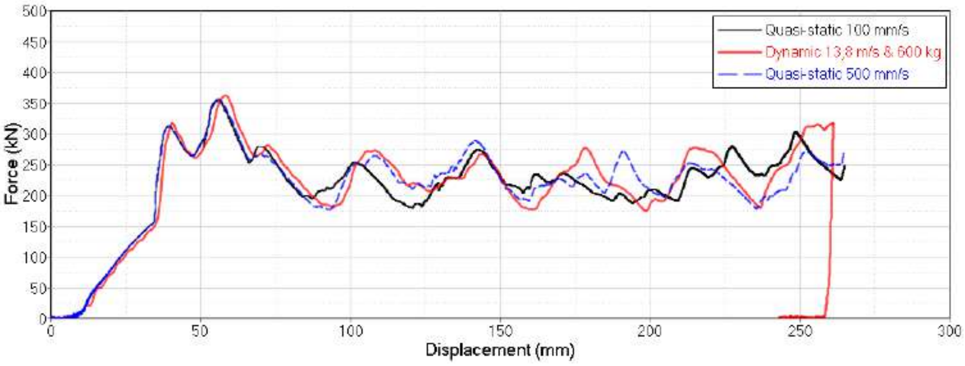

Figure 5.3: Trimmed curves force vs displacement for dynamic and quasi-static comparison

Table 5.2: Values for quasi-static and dynamic comparison

Test	**EA** **(J)**	F_{max} **(kN)**
Dynamic 13,8 m/s & 600 kg	56979,7	362,118
Quasi-static 100 mm/s	57057,9	354,491
Quasi-static 500 mm/s	57253,6	356,621

As seen, the values for each test are close to each other, so the quasi-static procedure can be a good approach to replace the dynamic test in an accessible place with the desired conditions. This way, the maximum force to perform the test in CEiiA installations has to be less than 250 kN. As seen in table 5.2, this value is always exceeded. Thus, the solution is to perform the quasi-static test in half of the structure since it is symmetric. The figure 5.4 represents the used half geometry to make the comparison between aproaches after the meshing process in Hypermesh.

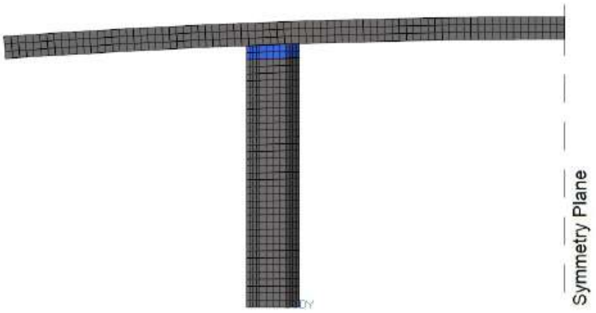

Figure 5.4: Meshed half geometry

To prove the effectiveness of this solution to provide the structure's characteristics in an experimental test, the obtained solutions for half of the structure are in figure 5.5 and table 5.6. The curves were multiplied by two since it is assuming that the test is performed in a symmetric way. Thus, to have a simpler comparison, the curves are in the same region in the graphics.

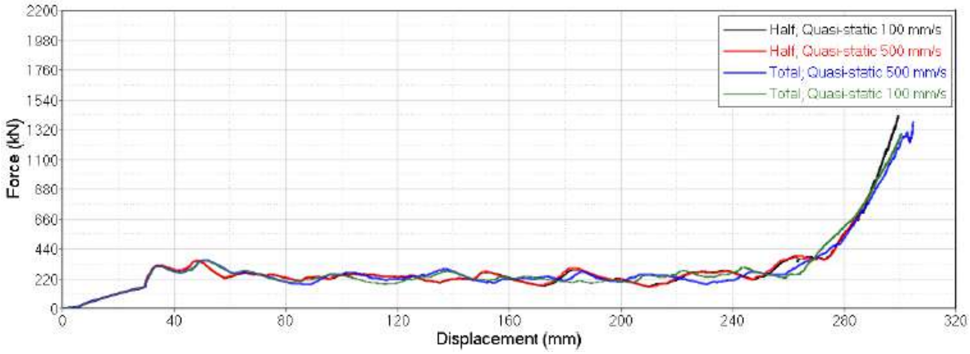

Figure 5.5: Comparison between the tests with the half and total geometry

As stated before, the values to be into account only have relevance for the displacement values presented in the dynamic test. This way, the graphs from figure 5.5 are cut to in order to obtain the values to have the final comparison between the different tests as presented in figure 5.6

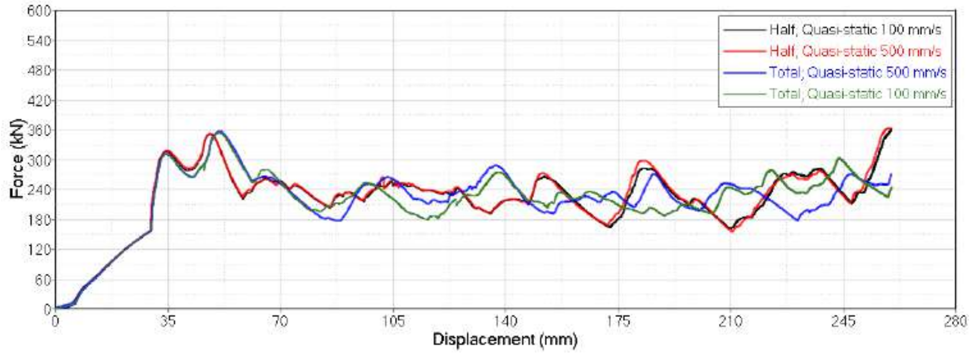

Figure 5.6: Comparison between the tests with the half and total geometry with trimmed curves

Table 5.3: Quasi-static comparison between the total and half structures

Test	**EA (J)**	F_max **(kN)**
Half; 500 mm/s	58003,7	352,44
Half; 100 mm/s	57545,9	351,4
Total; 500 mm/s	57185,2	359,92
Total; 100 mm/s	57000,9	354,46

Analysing figure 5.6 and table 5.3 it is concluded that it is possible to test the structure through a quasi-static test with the resources available in CEiiA since the values for both approaches are similar .

The structure have a curvature in the front part, so it needs a fixing point in the symmetry plane and in the other half to perform the test in a realistic way. Thus, it is ensured that the structure do not deform in the non solicited half. Figure 5.7 and 5.8 show the developed procedure to the quasi-static test.

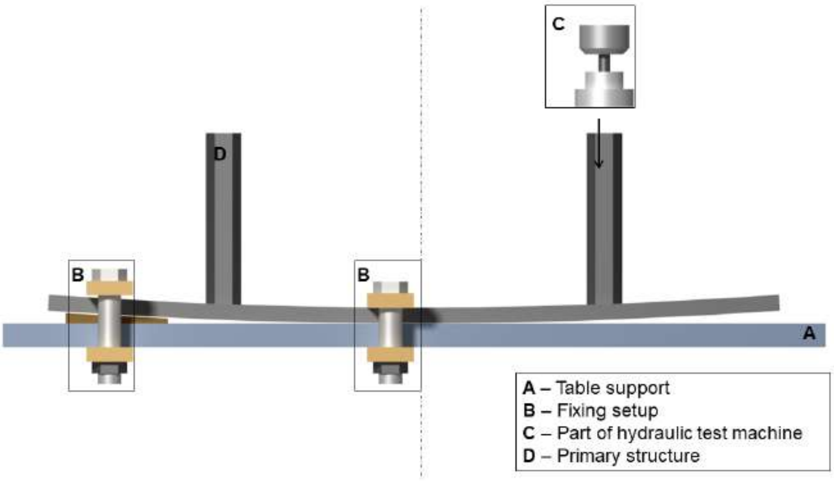
C
D
B
B
A
A – Table support
B – Fixing setup
C – Part of hydraulic test machine
D – Primary structure

Figure 5.7: Quasi-static procedure

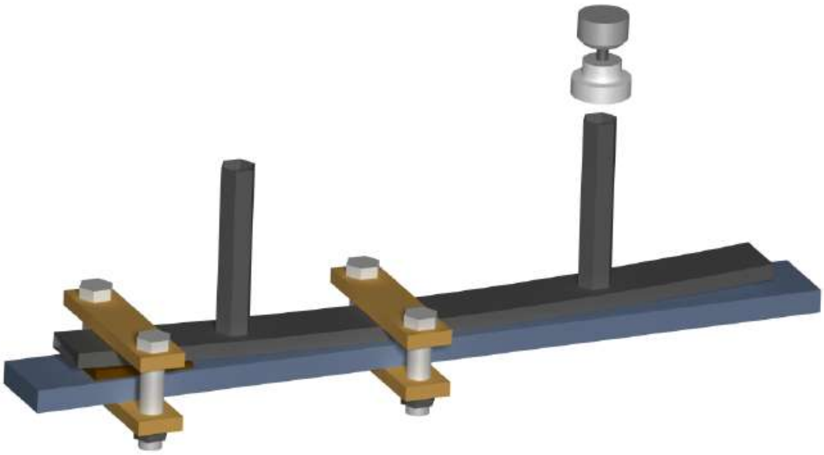

Figure 5.8: Isoview of the quasi-static procedure

As seen, the fixing point must be next to the center line in the opposite side of the hydraulic press. With this experimental procedure it is expected to achieve results in accordance with the curves presented in figure 5.6.

Chapter 6

Conclusions

The developed optimization process made possible to optimize different crash management systems to protect the occupants of four different vehicle typologies.

The process using a $MATLAB$ script to implement the *NGSA II* optimization algorithm obtained the desired solutions. Besides that, all solutions fulfils the Euro NCAP regulations regarding the full width frontal impact protocol.

The primary structure to be used in all vehicle topologies revealed the desired behaviour in all tests, protecting effectively the vehicle with lower mass.

Moreover, the optimized secondary structures to complement the primary structure in the heavier vehicles had a good relation between increase in mass and energy absorption.

The primary structure absorbed almost the same amount of energy in all tests, being the secondary structures responsible to absorb the energy remaining due to the mass addition.

The solutions in the Pareto front are mainly obtained by those made with the 6061 T6 and 6082 T6 alloys. It can be concluded that the value of the yield strength is the most important parameter with more importance for crashworthiness effects.

To achieve reliable results the best approach was to compute the impact tests in the both structures simultaneously.

Finally, it is expectable that a quasi-static experimental test in half of the structure would be enough to validate the achieved solution for the primary structure.

6.1 Achievements

The achievements in this work were:

- The development of a procedure based on a $MATLAB$ script to implement the NGSA II algorithm to optimize any desired structure to be crashed into a rigid wall;
- The modulation of the HAZ in the soldering between the crash boxes and the front bumper revealed beneficial in the peak force reduction;

- It was concluded that for secondary structure it is necessary the impact tests in both structures simultaneously;
- The primary structure has proven efficient in all tests even in the vehicle with higher masses;
- The implementation of the secondary structure was a good approach leading to a structure that can fulfil the requirements within the given bounds by the design;
- The use of hexagonal cross shapes and the 6061 T6 or 6082 T6 alloys proved to have the best trade off between CFE and SEA for these cases.

6.2 Future Work

To complement the work developed along this project, experimental quasi-static test can be performed to compare the theoretical results with the experimental data.

On the other hand, the test with a deformable barrier has to be done for the crash management systems to be approved in the homologation tests.

The head injury criteria has to be calculated with more accuracy with a dummy in order to acquire the correct values of the head accelerations.

The rigid behaviour of the car structures attached to the crash boxes has to be modulated as an elastic body instead of a rigid body to have more realistic solutions.

Additionally, as the cross shapes of the crash boxes were simple, the next steps are to include several internal reinforcements with cellular shapes, some types of metallic foams, the effect of mechanical triggers as well as different materials.

Finally, as the materials that come from the suppliers do not have always the dimensions obtained from the optimization processes, it would be interesting to test the geometries made with the standard measures.

Bibliography

[1] European Commission Directorate General for Mobility and Transport. DaCoTa (2012) Roads. `www.dacota-project.eu`, Accessed April 2018.

[2] European Commission Directorate General for Mobility and Transport. Road Safety Evolution in EU. `https://ec.europa.eu/transport/road_safety/sites/roadsafety/files/pdf/observatory/historical_evol.pdf`, Accessed April 2018.

[3] European Commission Directorate General for Mobility and Transport. Vehicle Safety Systems. `https://ec.europa.eu/transport/themes/its/road/application_areas/vehicle_safety_systems_en`, Accessed April 2018.

[4] A. Isenstadt, J. German, P. Bubna, M. Wiseman, U. Venkatakrishnan, L. Abbasov, P. Guillen, N. Moroz, D. Richman, and G. Kolwich. Lightweighting technology development and trends in U.S. passenger vehicles. *International Council On Clean Transportation*, 2016.

[5] European Commission Directorate General for Mobility and Transport. What are main crash injury situations? `https://ec.europa.eu/transport/road_safety/specialist/knowledge/vehicle/key_issues_for_vehicle_safety_design/what_are_main_crash_injury_problems_en`, Accessed April 2018.

[6] F. A. T. U.S. Department of Transportation. Vertical Drop Test of a Narrow-Body Fuselage Section With Overhead Stowage Bins and Auxiliary Fuel Tank on Board, 2002.

[7] T. M. Encarnação Nunes. Multi-objective design optimization of a frontal crash energy absorption system for a road-safe vehicle. Master's thesis, Instituto Superior Técnico, Portugal, 2017.

[8] CEiiA. CEiiA - About Us. `https://www.ceiia.com`, Accessed August 2018.

[9] Meios e Publicidade. Sete Presidentes e Um Festival de Criatividade. `http://www.meiosepublicidade.pt/2013/05/sete-presidentes-e-um-festival-de-criatividade`, Accessed September 2018.

[10] J. Happian-Smith, editor. *An introduction to Modern Vehicle Design*. Butterworth-Heinemann, 2002.

[11] S. A. Nikolaevich, A. A. Valerievich, G. A. Igorevich, S. A. Alexandrovich, and S. M. Alexandrovich. *Advanced materials of automobile bodies in volume production*. European Transport, 2014.

[12] D. Mackenzie, J. Heywood, and S. Zoepf. Determinants of U. S. passenger car weight. *Int. J. Vehicle Design*, 65(1):73–93, 2014.

[13] L. W. Cheah. *Cars on a Diet: The Material and Energy Impacts of Passenger Vehicle Weight Reduction in the U. S.* PhD thesis, Massachusetts Institute of Technology, U.S.A., 2010.

[14] P. D. Bois, C. C. Chou, B. B. Fileta, A. I. King, H. F. Mahmood, H. J. Mertz, and J. Wismans. Vehicle crashworthiness and occupant protection. American Iron and Steel Institute, 2004.

[15] Uniform provisions concerning the approval of vehicles with regard to the protection of the occupants in the event of a frontal collision. 2017. Addendum 93: Regulation No. 94.

[16] European Comission. Saving lives: Boosting car safety in the EU. 2016.

[17] Uniform provisions concerning the approval of vehicles with regard to the protection of the occupants in the event of a lateral collision. 2014. Addendum 94: Regulation No. 95.

[18] Democratising Car Safety - Road Map for Safer Cars 2020. `http://www.globalncap.org/wp-content/uploads/2015/04/road-map-2020.pdf`, Accessed September 2018.

[19] European New Car Assessment Programme (Euro NCAP). `https://www.euroncap.com/en`, Accessed September 2018.

[20] National Highway Traffic Safety Administration. `https://www.nhtsa.gov`, Accessed April 2018.

[21] B. Wade. *Capturing the Energy Absorbing Mechanisms of Composite Structures under Crash Loading*. PhD thesis, University of Washington, U.S.A., 2014.

[22] T. Tang, W. Zhang, H. Yin, and H. Wang. Crushing analysis of thin-walled beams with various section geometries under lateral impact. *Thin-Walled Structures*, 102:43–57, 2016.

[23] L. Morello, L. R. Rossini, G. Pia, and A. Tonoli. *The Automotive Body*, volume II : System Design. Springer: Mechanical Engineering Series, 2011.

[24] A. Kuznetcov, I. Telichev, and C. Q. Wu. Effect of Thin-walled Tube Geometry on Its Crashworthiness Performance. In *14th International LS-DYNA Users Conference*, Canada, June 2016. University of Manitoba.

[25] M. E. Erdin, C. Baykasoglu, and M. T. Cetin. Quasi-static axial crushing behavior of thin-walled circular aluminum tubes with functionally graded thickness. *Procedia Engineering*, 149:559–565, 2016.

[26] G. Sun, F. Xu, G. Li, and Q. Li. Crashing analysis and multiobjective optimization for thin-walled structures with functionally graded thickness. *International Journal of Impact Engineering*, 64:62–74, 2013.

[27] X. Zhang, H. Zhang, and Z. Wang. Bending collapse of square tubes with variable thickness. *International Journal of Mechanical Sciences*, 106:107–116, 2015.

[28] P. Bogusz, M. Stankiewicz, and G. Sławiński. Energy absorption study of aluminium profiles with variety of filling configurations. *Engineering Transactions*, 65(4):543–562, 2017.

[29] W. Abramowicz and N. Jones. Dynamic axial crushing of square tubes. *International Journal of Impact Engineering*, 2(2):179–208, 1984.

[30] W. Abramowicz and N. Jones. Dynamic axial crushing of circular tubes. *International Journal of Impact Engineering*, 2(3):263–281, 1984.

[31] N. Qiu, Y. Gao, J. Fang, Z. Feng, G. Sun, and Q. Li. Crashworthiness analysis and design of multi-cell hexagonal columns under multiple loading cases. *Finite Elements in Analysis and Design*, 104: 89–101, 2015.

[32] N. Qiu, Y. Gao, J. Fang, G. Sun, and N. H. Kim. Topological design of multi-cell hexagonal tubes under axial and lateral loading cases using a modified particle swarm algorithm. *Applied Mathematical Modelling*, 53:567–583, 2017.

[33] N. N. Hussain, S. P. Regalla, and Y. V. Rao. Comparative Study of Trigger Configuration for Enhancement of Crashworthiness of Automobile Crash Box Subjected to Axial Impact Loading. *Procedia Engineering*, 173:1390–1398, 2016.

[34] European Aluminium Association. The Aluminum Automotive Manual. Applications - Car body – Crash Management Systems, 2013.

[35] T. N. Tran, S. Hou, X. Han, and M. Q. Chau. Crushing analysis and numerical optimization of angle element structures under axial impact loading. *Composite Structures*, 119:422–435, 2014.

[36] X. Zhang and H. Zhang. Numerical and theoretical studies on energy absorption of three-panel angle elements. *International Journal of Impact Engineering*, 46:23–40, 2012.

[37] N. Qiu, Y. Gao, J. Fang, Z. Feng, G. Sun, and Q. Li. Theoretical prediction and optimization of multi-cell hexagonal tubes under axial crashing. *Thin-Walled Structures*, 102:111–121, 2016.

[38] Altair. Hyperworks 2017 Radioss User guide. `altairhyperworks.com`, Acessed June 2018.

[39] Y. Chen, A. H. Clausen, O. S. Hopperstad, and M. Langseth. Stress-strain behaviour of aluminium alloys at a wide range of strain rates. *International Journal of Solids and Structures*, 46:3825–3835, 2009.

[40] N. Nazemi. *Identification of the mechanical properties in the heat-affected zone of aluminum welded structures*. PhD thesis, University of Windsor, Canada, 2015.

[41] P. Sensharma, M. Collette, and J. Harrington. Effect of welded properties on aluminum structures. Technical report, Ship Structure Committee, 2010.

[42] The European Union. Eurocode 9: Design of aluminium structures, 2006. Part 1-1: General structural rules.

[43] Altair University. Crash Analysis with RADIOSS - A Study Guide, 2015.

[44] V. Adams and A. Askenazi. *Building Better Products with Finite Element Analysis*. OnWord Press, 1999.

[45] RADIOSS. Radioss Theory Manual: Large Displacement Finite Element Analysis, 2009.

[46] D. Ogmaia and S. E. Tasel. Simulation of vehicle crash into bridge parapet using Abaqus / Explicit. *KTH Royal Institute of Technology, Sweden*, 2015.

[47] MathWorks. Mathworks Documentation. `https://www.mathworks.com/help/gads/how-solvers-compute-in-parallel.html`, Acessed September 2018.

[48] K. Deb. *Multi-Objective Optimization using Evolutionary Algorithms*. John Wiley & Sons, Ltd, 2001.

[49] F. Djamaluddin, S. Abdullah, A. Ariffin, and Z. Nopiah. Multi objective optimization of foam-filled circular tubes for quasi-static and dynamic responses. *Latin American Journal of Solids and Structures*, 16(2):1126–1143, 2014.

[50] X. Chen and J. Yang. Optimization of longitudinal beam for improvement of crashworthiness in frontal and offset impacts. pages 582–585, 2012.

[51] European Aluminium Association. The Aluminum Automotive Manual. Materials – Resources, 2002.

[52] Corrosion of Aluminum and Aluminum alloys. *ASM International*, pages 1 –10, 1999.

[53] RPM Industries LLC. `https://www.rpmindinc.com/aluminum-extrusions-uses-and-applications/`, Acessed September 2018.

[54] European Aluminium Association. The Aluminum Automotive Manual. Applications - Materials – Designation System, 2002.

[55] SAE Intenational: The Engineering Society For Advancing Mobility Land Sea Air and Space. SAE J211: Instrumentation for Impact Test - Part 1 - Electronic Instrumentation, 1995.

[56] S. Kokkula, O. S. Hopperstad, O. G. Lademo, T. Berstad, and M. Langseth. Offset impact behaviour of bumper beam-longitudinal systems: Numerical simulations. *International Journal of Crashworthiness*, 11(4):317–336, 2006.

[57] J. A. L. Campos, A. S. Robleda, J. A. V. Vilán, P. J. G. Nieto, and J. B. Cordero. Study of a steel's energy absorption system for heavy quadricycles and nonlinear explicit dynamic analysis of its behavior under impact by FEM. *Materials*, 8(10):6893–6908, 2015.

[58] Standard Test Methods for Tension Testing Wrought and Cast Aluminum- and Magnesium-Alloy Products. *ASTM International*, 2015.